Stony Brook University

A Surface Science Study of Metal Oxides and Supported Nanoparticles for the Production of Clean Hydrogen

A Dissertation Presented

by

John C. Lofaro Jr.

to

The Graduate School

in Partial Fulfillment of the

Requirements

for the Degree of

Doctor of Philosophy

in

Chemistry

Stony Brook University

August 2013

Stony Brook University
The Graduate School

John C. Lofaro Jr.

We, the dissertation committee for the above candidate for the

Doctor of Philosophy degree, hereby recommend

acceptance of this dissertation.

Michael G. White – Dissertation Advisor
Professor, Chemistry Department
Senior Chemist, Chemistry Department, Brookhaven National Laboratory

David M. Hanson - Chairperson of Defense
Distinguished Service Professor, Chemistry

Trevor Sears – Third Member
Professor, Chemistry Department
Senior Chemist, Chemistry Department, Brookhaven National Laboratory

Dario Stacchiola – Outside Member
Associate Chemist, Chemistry Department, Brookhaven National Laboratory

This dissertation is accepted by the Graduate School

Charles Taber
Interim Dean of the Graduate School

Abstract of the Dissertation

A Surface Science Study of Metal Oxides and Supported Nanoparticles for the Production of Clean Hydrogen

by

John C. Lofaro Jr.

Doctor of Philosophy

in

Chemistry

Stony Brook University

2013

The search for alternative fuels has increased over the past decade due to a growth in energy demand and the need to reduce carbon output. Hydrogen has been seen as a potential replacement for fossil fuels, such as oil and coal. A clean source of hydrogen and can be processed via the water gas (WGS) shift reaction ($H_2O + CO \rightarrow CO_2 + H_2$). However, current industrial catalysts are comprised of a mixture of metal-oxides and supported nanoparticles that are often too complex to accurately elucidate reaction mechanisms. Using well defined "model systems" in a controlled reaction environment provides a route to gain fundamental understanding of how these catalysts function. Work presented here focuses on the study of model metal oxides and supported nanoparticles for the production of hydrogen.

Primarily the WGS reaction has been investigated on Au/TiO_2 (110), Cu/TiO_2 (110) and $Cu/CeO_2/YSZ$ (111) catalysts. These particular systems have been shown to be active for H_2 generation under simulated industrial conditions, but little is known about their thermal reactivity

and stability. It was found that the function of oxide surfaces was to adsorb and dissociate water, while the nanoparticles are the main source of CO adsorption above 300 K. The role of the metal oxide support was studied using Cu/CeO_2. It is apparent a stronger metal-support interaction exists for ceria supported copper compared to titania supported copper and gold, evidenced by partial encapsulation of copper by ceria at elevated temperatures. These characteristics may be crucial to improve functional understanding of the industrial catalysts.

Another method to produce clean hydrogen is to photocatalytically split water ($2H_2O \rightarrow 2H_2 + O_2$). A study of the electronic structure, using x-ray photoelectron spectroscopy (XPS), of several potential water splitting photocatalysts was undertaken. A family of lanthanum titanate ($LaTiO_{3.5}$) crystal surfaces was studied. Understanding the electronic states of each system may lend insight into the nature of their activity. The interaction of water on the surface of these materials was also studied. Results show that water does not dissociatively adsorb on the surface, suggesting that H_2O, not –OH is the active reactant for H_2 generation. Another promising water splitting photocatalyst, $SrTiO_3$:Rh, was also studied using XPS and showed that the incorporation of Rh^{4+} ions into the lattice, and not Rh^0 particle formation on the surface, was the driving force for increased visible light absorbance and photocatalytic activity. This emphasizes the role catalyst preparation plays in both the performance and stability of a catalyst.

Dedication Page

For Conrad Lofaro

Table of Contents

List of Figures

List of Tables

List of Abbreviations

AES – Auger Electron Spectroscopy

DFT – Density Functional Theory

eV – electron Volt

FTIR – Fourier Transform Infrared

FWHM – Full Width Half Maximum

ISS – Ion Scattering Spectroscopy

L – Langmuir (1×10^{-6} Torr/sec)

LN_2 – Liquid Nitrogen

ML – Monolayer

PC – Polymerizable Complex

PEMFC – Proton Exchange Membrane Fuel Cell

ppm – Part Per Million

QMS – Quadrupole Mass Spectrometer

SSR – Solid State Reaction

STM – Scanning Tunneling Microscopy

TEM – Transmission Electron Microscopy

TPD- Temperature Programmed Desorption

TWh – Terawatt hour

UHV – Ultra High Vacuum

WGS – Water Gas Shift

XRD – X-ray Diffraction

Acknowledgments

I would like to acknowledge the help and support I received throughout my long and sometimes trying graduate career at Stony Brook University. First, I would like to thank my research advisor Professor Michael G. White for all his time, guidance, and patience that he has afforded me over the years. Though there were many trying times he never gave up on me and never allowed me to give up on myself. Also, I want to thank my advisement committee members: Professors David M. Hanson and Trevor Sears, and Dr. Dario Stacchiola for their guidance and valuable time they committed to my graduate career.

I would also like to send a big thank you to all my fellow group members, both past and present for all their help. Past members Dr. James Lightstone, Dr. Melissa Patterson, and Dr. David Sporleder were my first teachers in surface science; their help through my first years was invaluable and they were able to teach me to handle any situation that may arise in the laboratory. Extra special thanks to Dr. Daniel Wilson, Joseph Magee, and Matt Kershis for all their help. They were not only valuable muscle in reconfiguring equipment and providing helpful discussions, but they were valuable friends that were able to help me get through anything.

Finally none of this would be possible without my family: John C. Lofaro Sr., Lisa Lofaro, Amanda Testani, Nicholas Testani, and Ann Lofaro. Without their constant supply of free meals, giving me a place to live, and especially their undying belief that I would achieve what I set out to even though there were times I did not believe in myself, I would not have been able to accomplish this degree.

Chapter 1

1. **Introduction**

The search for alternative fuels has increased over the past decade due to the increase in energy demand and the need to reduce carbon output. The world's population has recently eclipsed 7 billion and continues to rise. With this increase in population comes an increase in energy demand, especially from countries like China and India, which are currently going through an industrial revolution. There has been an increase in the use and development of solar, wind, hydroelectric, and nuclear energy over the past decade to help offset this demand. Unfortunately, these energy sources account for only ~18% of the world's power production, while more than 80% still comes from fossil fuels,[1] which are both in finite supply and harmful to the environment. There is theoretical potential[2] for these energy sources to supply the world with more than the ~19000 TWh [3] it needs; however, these forms of energy production suffer from fundamental issues that cannot be controlled. Solar, wind, and hydroelectric are all at the mercy of Mother Nature, thus making them at times unreliable. If there is no sun, solar panels, both thermal and photovoltaic, will not work and without wind there is nothing to propel the turbines. Additionally, there does not yet exist an efficient way to convert incident solar radiation into usable energy.[4] Hydroelectric power output will vary greatly without consistent water flow, thus vast manmade reservoirs must be made to keep the supply consistent. In the aftermath of the Fukushima reactor meltdown that resulted from the tsunami that struck Japan in 2011, public perception of the dangers of nuclear reactors is heightened, causing resistance to the construction of new nuclear power plants. Second is the issue of the spent nuclear waste which must be stored somewhere safe while it remains radioactive.[5] However, the major barrier to

expanding the implementation of these energy sources is that fossil fuels are still economically favorable.

Hydrogen has been eyed as a viable replacement for fossil fuels due to its ability to be used in various ways, including in fuel cells and direct combustion.[5-8] It also has an energy density approximately three times greater than gasoline, based on their available chemical energy. Unfortunately the current supply of hydrogen is derived mainly from steam reforming of hydrocarbons, which is a non-renewable source. These hydrocarbons come from the world's finite reserve of fossil fuels. One source of these hydrocarbons is oil, which is not only used in the production of fuel (gasoline, diesel, etc.), but is the major source of plastics and other industrial materials. These plastics have become a vital part of every day life, from housing water in convenient portable bottles to body panels on automobiles. One model predicts that if we maintain our current oil usage we only have enough reserves to last ~200 years.[9] Recent trends show that we are increasing our energy usage by ~2.4% per year and this increase has been steady for approximately the past decade.[1] However, due to China and India's ongoing industrial revolutions the depletion of oil reserves may accelerate and could be exhausted within the next 50 years.[9]

In addition to rapidly depleting the finite supply, our dependence on fossil fuels has led to an increase in atmospheric CO_2. This increase has led to a change in our planet's climate; most notably, the Earth's average temperature has risen 1.4 °F over the past century and may increase by as much as 11.5 °F over the next century.[10] Though 1.4 °F is a small change in temperature, it has already had a large effect on our climate. Recently the Midwest of the United States has experienced one of its worst droughts in recorded history, causing damage to crops which resulted in lower crop yields and in turn higher prices for the food that was produced. This

increase in temperature not only results in severe droughts, but also can result in massive flooding, caused by an increase in the melting of mountain snow and/or dramatic changes in weather patterns.[10] Higher temperatures are not the only result of changing climate, as the number of extreme weather incidents has also increased dramatically.[10] This is evidenced by Hurricanes Katrina, Irene, and most recently Sandy, which made landfall and devastated large sections of shoreline throughout the Tri-State area in 2012. This increase in temperature has also melted more of the polar ice caps, raising sea levels and altering the delicate balance of our oceans.[10] These weather related issues have caused billions of dollars in damage and have taken the lives of thousands.

Though hydrogen has been viewed as a potential solution to our need for a new energy source, the system of production needs to be clean and efficient. One promising system is the proton exchange membrane fuel cell (PEMFC); especially as a portable energy source to replace the internal combustion engine in cars.[5, 11] The ideal energy source for these fuel cells is pure hydrogen. Unfortunately the current source of hydrogen (steam reforming of hydrocarbons) contains a high percentage of CO as a byproduct. Even low levels (ppm) of CO are known to poison noble metal catalysts commonly used in fuel cells.[11] A new clean and sustainable source of hydrogen has to be found if we are to switch to a hydrogen based economy. The water-gas shift (WGS) reaction ($CO + H_2O \leftrightarrow H_2 + CO_2$) can be used as a standalone source of hydrogen or in conjunction with steam reforming to increase overall H_2 production while removing CO, resulting in a clean, useable source of hydrogen.[12-16] Besides producing usable H_2, the WGS reaction also produces CO_2, which is a known greenhouse gas and contributor to global warming. However, there are current efforts to capture and store or use manmade CO_2.

Many industrial processes rely on the presence of heterogeneous catalysts, which lower the activation barrier for a reaction while remaining unchanged. These systems are usually highly complex, consisting of multiple components interacting in multiple ways and can be extremely difficult to characterize. The lack of mechanistic information hinders our ability to improve the catalysts' efficiency, which would lead to higher purity products, produced at a lower cost. Fundamental studies of model systems allow for insight into how these complex systems work and can lead to strategies to improve the industrial catalyst.

The main focus of this dissertation is understanding how catalysts used to produce clean hydrogen via the Water Gas Shift (WGS) reaction work. Here, model systems consisting of a TiO_2 (110) single crystal with and without Au and Cu nanoparticles and CeO_2 thin films with and without Cu nanoparticles are studied under ultrahigh vacuum (UHV) conditions to elucidate the reactivity and stability of these systems. A second potential source for clean hydrogen is the photocatalytic splitting of water. Novel materials (several lanthanum titanates and $SrTiO_3$:Rh) were investigated due to their unique properties, namely, band gap transitions that are accessible via visible light.

The current industrial WGS catalyst is comprised of Cu particles supported on a mixed Zn and Al oxide support, which operates in a temperature range of 450 – 575 K. Though this system is effective, it must undergo a long activation process and is pyrophoric.[13-15] If the WGS reaction is to be used as the source of hydrogen for fuel cells, a more efficient and safe catalyst needs to be found. Titania (TiO_2) and ceria (CeO_2) based catalysts have shown to be promising candidates for efficient low temperature WGS systems.[14, 17-28] Both supports are stable in the temperature range at which the reaction is known to take place and both oxides contain cations that have the ability to switch between 4+ and 3+ oxidation states.[29-31] This change in oxidation

state allows for the surface to have a role in the reduction and oxidation of water. Though these systems have been studied under high pressure,[13-17, 20-23, 25-27, 31-35] in order to simulate industrial conditions, minimal focus has been given to fundamental surface science experiments. These fundamental studies are necessary to elucidate the roles of these oxides and their supported particles, i.e. where and how the reactants bind.

Titania and titania supported nanoparticles have been used for numerous thermal[17, 27, 28, 30, 36-38] and photochemical[39] reactions as well as applications like sunscreens[40] and self-cleaning clothes.[41] However, bare TiO_2 is not active for the oxidation of CO to CO_2, an important part of the WGS reaction.[29, 42] The addition of Au nanoparticles has been shown to increase the rate of CO oxidation.[43] The authors found that the activity was not directly correlated to the change in CO binding, but rather gold's increased ability to bind oxygen compared to that of the support. Furthermore, the total evolved CO_2 can be accounted for based on oxygen bound only to the Au nanoparticles. TiO_2 supported Au nanoparticles were also found to be active for the WGS reaction. Haruta and co-workers showed that Au nanoparticles supported on P-25 titania (a mixture of rutile and anatase phases) had a turn over frequency for CO oxidation, as a result of the WGS reaction, that was more than four times greater than that of commercial $Cu/ZnO/Al_2O_3$.[28] It was also shown that reactivity increases with increased loading of Au up to investigated maximum loading of 10 %. In Chapter 3 of this dissertation the reactivity of TiO_2 supported Au and Cu nanoparticles is investigated as it pertains to the WGS reaction

Chen et. al. have found that Cu deposited on P-25 TiO_2 was active for CO oxidation.[44] It was found that the activity was nearly consistent for the different Cu loadings investigate (3.7 – 10.3 wt%) and was attributed to the similar particle size for each loading. However, the calcination temperature played a considerable role in the rate of CO_2 production with ~2 times

greater generation as calcination temperature increased from 413 to 473 K. The authors also conducted FTIR studies and found that Cu^{2+} was reduced at 437 K and is likely the driving force for the increased activity. Titania supported copper, like Au/TiO_2, has shown high activity for the WGS reaction. Rodriguez and co-workers showed that Cu/TiO_2 produced more hydrogen than pure Cu and Cu supported on various other metal oxides.[14] They also used DFT calculations to show that the WGS reaction has a lower activation energy on a Cu_{29} nanoparticle when compared to a Cu (100) surface, providing further evidence for the increased reactivity of Cu nanoparticles.

The support that a nanoparticle is dispersed on can have a dramatic effect on its stability and reactivity.[14, 27, 38, 45-47] The experiments in Chapter 4 will focus on how changing from TiO_2 to CeO_2 affects the reactivity and stability of Cu nanoparticles as a model catalyst for the WGS reaction. Ceria's (CeO_2) ability to easily undergo changes in oxidation state between Ce^{4+} and Ce^{3+}, which allows it to readily accept and donate oxygen atoms,[31] makes it a promising oxide support replacement for the industrial WGS catalyst ($Cu/ZnO/Al_2O_3$).[13, 15] Chen and co-workers have shown that Cu deposited on SiO_2 has high activity for the WGS reaction with the entire reaction taking place on the Cu nanoparticles or at the metal-oxide interface, with no activity occurring on the bare SiO_2 support.[13] Previous work has shown Cu/CeO_2 to have superior WGS performance when compared to Cu/ZnO, Au/ZnO, single crystal Au, and single crystal Cu systems.[21] Its hydrogen production was also on par with that of Au/CeO_2, and Cu/MnO_2 systems.[14, 21] It was found that the dissociation of water took place predominately on the CeO_2 surface while CO oxidation occurred on the nanoparticle or particle/substrate interface. This demonstrates that an oxide can be more than a support to disperse the nanoparticles and may play a vital role in the reaction.

Along with the WGS reaction, the photochemical splitting of water can produce a clean source of hydrogen from an abundant and renewable source. Ever since Fujishima and Honda found that TiO_2 was an effective photocatalyst,[48] the past 40 years has been filled with many efforts to design an optimal photocatalytic material.[39, 49, 50] There have been a wide range of materials studied for the photochemical production of hydrogen; with various oxides[51, 52] (doped and undoped), oxynitrides,[53, 54] and oxysulfides[55] found to be most promising. In chapter 5, the role of preparation in $SrTiO_3$:Rh particle synthesis is investigated as it pertains to photochemical hydrogen evolution. $SrTiO_3$ by itself is an active photocatalyst but only under UV irradiation, due to it wide band gap of ~3.2 eV.[56] Konata and co-workers found that doping $SrTiO_3$ with Rh produced a visible light active photocatalyst that had a measurable H_2 production rate, under their reaction conditions, that was at least twice as high as the next best dopant.[57] The authors attributed this increase to the presence of Rh^{3+} and Rh^{4+} or Rh^{5+} species. However, experiments to determine the presence of these species were not performed. The introduction of Rh into the lattice produces states within the $SrTiO_3$ band gap that allow for multiphoton excitation across the band gap, allowing visible light energy to be used to generate electron-hole pairs. XPS has the ability to identify the oxidation states of the Rh and to confirm their incorporation into the lattice or on the surface as particles**,** which will be discussed in the final chapter of this dissertation.

Finally, in Chapter 6, a series of La containing titanates will be investigated for their composition and interaction with water. He and co-workers have found that a lanthanum and iodine co-doped TiO_2 show high catalytic activity under visible light for the degradation of oxalic acid (model pollutant).[51] The authors determined that the incorporation of iodine into the lattice shifted the catalyst's adsorption edge from the ultraviolet into the visible region of the

solar spectrum, while the La_2O_3 that formed on the surface slowed the recombination of electron-hole pairs. $La_2Ti_2O_7$ loaded with Ni has been found to have a dramatically higher H_2 evolution rate when compared to Pt/TiO_2 and other perovskite samples.[58, 59] This increase in activity was attributed to the longer electron hole pair lifetime and the charge transfer that existed between the oxide and metal co-catalyst.

Chapter 2

2. Experimental Section

This chapter will discuss the vacuum instrumentation used for the experiments carried out in this dissertation. Section 2.1 will describe the overall design and layout of the UHV chamber and substrates used. Section 2.2 will discuss the individual techniques that were used for the preparation and analysis of the various systems studied.

2.1 Layout and Substrates

2.1.1 UHV Chamber

Experiments were conducted in an UHV chamber (Fig. 2.1) with a base pressure less than 8×10^{-10} Torr. The chamber is pumped by a 600 L/s turbomolecular pump (Oerlikon Leybold). A residual gas analyzer (SRS 200) is used to monitor the composition of the background gases. The lower level of the chamber was outfitted with a quadrupole mass spectrometer (Extrel), a direct doser, a quartz microbalance (Inficon XTM/2), and a homemade thermal evaporator. The upper level of the chamber is equipped with various spectroscopic instruments including an Auger electron spectroscopy system (PHI Electronics, 10-155A), an Al/Mg dual anode x-ray source (PSP Vacuum Technology, TX400/2), an ion gun used for ion scattering spectroscopy (Thermo Scientific), and a 100 mm hemispherical energy analyzer (Oxford Applied Research, VSW 100). The chamber also contains a sputter gun (LK Technologies), which produces Ar^+ ion beams to clean the surface by sputtering away any contaminants. An XYZ manipulator (MDC Vacuum) and differentially pumped rotation stage (McAllister Technical) allows for access to all levels of the chamber.

2.1.2 Substrates

Experiments were conducted on TiO_2 (110), CeO_2/YSZ (111), $La_2Ti_2O_7$, $La_5Ti_5O_{17}$, nitrided $La_2Ti_2O_7$ surfaces, and $SrTiO_3$:Rh powders pressed on Al plates. All substrates were mounted on a Ta backing plate (0.060" thick) with a piece of 0.010" thick gold foil between and held in place with Mo clips (0.010" thick) screwed into the plate. The plate was mounted to a thermocouple/power feedthrough (Ceram Tec North America) via two Ta wires (1 mm). This arrangement allowed for the sample to be resistively heated and LN_2 cooled. Crystal temperature, which ranged from 110 K – 900 K, was measured using a type K thermocouple held in place on the face of the crystal by one of the molybdenum clips, except for the TiO_2 crystal, for which the thermocouple was inserted into a 0.020" diameter hole drilled in one edge and held in place with high temperature cement (Omegabond 600, Omega). A schematic of this set-up is shown in Figure 2.2.

The TiO_2 crystal (Crystek) was initially subjected to several cycles of high energy, (3 keV) high temperature (800 K) Ar^+ sputtering followed by annealing at 850 K in vacuum. This process removes the bulk impurities, typically potassium and calcium, which can be tracked by AES. The crystal was not deemed clean until impurities were below detectable limits and a clean (1x1) LEED pattern was obtained, which signified long range order. This procedure also induced a change in the crystal color from colorless to light blue. This color change was due to the creation of bulk defects (oxygen vacancies). These defects make the sample conductive enough for electron/ion spectroscopy with minimal charging. The surface underwent a daily regimen of low energy sputtering (0.5 KeV for 10 mins) and high temperature annealing (850 K for 30 mins) to ensure surface cleanliness. Annealing in a background of O_2 (2.0×10^{-6} Torr) resulted in an oxidized surface while annealing in vacuum resulting in a reduced surface (TiO_{2-x}).

In cases where metal nanoparticles were deposited, several cycles of sputtering and annealing were needed to provide a clean surface. Daily AES spectra were taken to insure surface cleanliness.

Ceria films (200 nm) were commercially (Spectrum Thin Films) grown on YSZ (111) single crystals (MTI Corporation) in a manner similar to previously established methods.[60-62] Briefly, Ce was vapor deposited in an atmosphere of O_2 (~3.0 x 10^{-7} Torr), while the crystal was maintained at a temperature of 750 – 800 K. There was no sign of yttrium or zirconium from the underlying support during initial testing by AES or XPS, indicating the substrate was completely covered by the CeO_2 film. To minimize film loss the surface was cleaned via high temperature (850 K) O_2 (2.0 x 10^{-6} Torr) annealing treatments unless nanoparticles were deposited, the removal of which necessitated the use of several cycles of Ar^+ sputtering. Once Zr became visible, via AES after numerous sputtering cycles, the crystal was removed and recoated. The film thickness (200 nm) allowed for several experiments where nanoparticles were deposited before the crystal had to be removed.

The various La titanates were created in collaboration with Dr. Limin Wang, Dr. Polina Burmistrova, and Prof. Peter Khalifah (Stony Brook University). Their preparation will be discussed in detail in Chapter 5. Briefly the $La_2Ti_2O_7$ and $La_5Ti_5O_{17}$ samples were prepared via the floating zone technique. The resultant crystals were then cleaved for use. The nitrided sample was prepared by flowing NH_3 over a cleaved $La_2Ti_2O_7$ crystal at high temperature. The crystals were mounted in the same manner as the CeO_2/YSZ (111) samples.

Rhodium doped $SrTiO_3$ powders were produced by three different methods as part of collaboration with Peichuan Shen and Dr. Alexander Orlov (Stony Brook University). Novel applications of the polymerized complex (PC) method and the hydrothermal method and the

more standard solid state reaction (SSR) method were used to produce samples. These procedures will be discussed in further detail in Chapter 6. Approximately 40 mg of the powder samples were placed between two Al plates (10 x 10 x 1mm) and compressed under ~2000 psi, one half of the loaded Al plate is shown in Figure 2.3. The plates were then separated and one plate is mounted in the sample holder shown in Figure 2.2.

2.2 Techniques

2.2.1 Nanoparticle Deposition

Nanoparticles of Au and Cu were deposited on a TiO_2 (110) single crystal and CeO_2 thin films grown on YSZ (111) using a homemade thermal evaporator. The evaporator consisted of a two pin medium voltage electrical feedthrough (Insulator Seal) and a DC power supply (Lambda Physics). The filament was composed of 0.015" thick tungsten wire (ESPI) wrapped with 0.005" thick gold or copper wire (ESPI). Evaporation was achieved by passing current through the metal wrapped tungsten filament, which produces enough heat to melt the Au or Cu wire and ultimately evaporate it. The evaporator was housed within a metal shroud with a 10 mm aperture, which could be blocked with a flag to accurately control exposure. The evaporating metal was contained within the shroud, which limited exposure of the chamber and instruments to unnecessary contamination, and aided in maintaining melting temperature by confining radiant heat. The deposition rate was monitored daily using a quartz microbalance which was accurate to a tenth of an Ångstrom. The average deposition rate was ~0.5 Å/min, resulting in total deposition times ranging from 1 to 20 minutes. The Au coverage in monolayers (ML) was estimated based on the thickness of one atomic layer of Au equaling ~2.4 Å.[63] Similarly, Cu coverage in ML was estimated by assuming that if Cu were to wet the surface a monolayer would occur at a film thickness of ~2 Å.[64] Copper coverages were later verified by XPS. Runs

of identical coverage were verified using metal/substrate ratios from either the AES or XPS spectra.

2.2.2 Temperature Programmed Desorption

Temperature programmed desorption (TPD) is an important surface science technique used to ascertain information about the adsorption/desorption processes of molecules bound to a surface. A species' molecular coverage, desorption energy (which is essentially equal to binding energy), and reaction order can all be determined from the resulting spectrum. In these experiments, TPD was conducted under UHV conditions with molecules being adsorbed at cryogenic temperatures (~110 K). By linearly heating a surface and monitoring the resulting desorbed molecules, a plot of signal intensity versus temperature can be produced. A molecule's desorption energy is related to its peak temperature and can be calculated using the Redhead analysis:

$$\Delta E_{des} = RT_{\max}\left[\ln\left(\frac{\upsilon_1 T_{\max}}{\beta}\right) - \ln\left(\frac{\Delta E_{des}}{RT_{\max}}\right)\right] \quad (2.1)$$

Where R is the ideal gas constant (1.9858775 x 10^{-3} kcal / mol·K), T_{max} is the temperature at the maximum of the peak in the TPD spectrum, β is the heating rate (1.5 K/s in these experiments), and ν_1 is the pre-exponential factor (assumed to be 10^{13} s^{-1}). The second natural log term in equation 2.1 can be estimated as 3.64. Though this equation is only for first order reactions, the logarithmic nature of the pre-exponential factor (ν_1), allows this equation be used for non-first order desorption processes and still provide useful desorption energies.[65]

TPD spectra were obtained by manipulating the crystal to the lower level where molecules of interest were introduced via a direct doser with a 5 micron aperture separating the gas reservoir from the dosing tube. Pressures indicated are those of the backing pressure

recorded before the aperture and measured using a capacitance manometer (MKS Instruments). In some cases, gases were backfilled into the chamber through a leak valve (Varian) and pressures were monitored on the chamber's ion gauge (Granville-Phillips). Prior to dosing, the crystal was cooled with LN_2 to ~110K to facilitate adsorption of the molecules of interest. Once the desired coverage was achieved, the crystal was rotated to face the quadrupole mass spectrometer (QMS) and a bias voltage of -75 V was applied to the crystal to prevent any electron mediated reactions that may occur due to the 70 V that can escape from the ionizer of the mass spectrometer. The QMS was set to monitor the species of interest as the temperature was linearly ramped via a computer controlled interface, schematically represented in Figure 2.4.

To simulate "high pressure," a pulsed valve setup was used to deliver a mixture of ^{13}CO and D_2O by bubbling carbon monoxide through a sample of D_2O. A backing pressure of 40 Torr (~1:1 mixture) was used with a pulse rate of 10 Hz, and pulse width of 700 µs. This set up allowed for the surface to experience a pressure of ~1 x 10^{-4} Torr while maintaining a chamber pressure below 1 x 10^{-7} Torr.

2.2.3 Auger Electron Spectroscopy

Auger electron spectroscopy (AES) is a surface sensitive core level spectroscopic technique used to identify and monitor elemental species. An incident high energy electron (1.5 – 3 keV) is used to eject a core level electron. The resulting core hole is filled by an electron in a higher lying state and the energy created by this relaxation is either emitted as x-ray florescence or the ejection of an additional high lying electron, the Auger electron (Figure 2.5). The kinetic energy of the Auger electron is element specific, and in this experiment is collected by a cylindrical mirror analyzer that is housed as part of the electron gun.

Though it is not possible to accurately determine the exact species concentration on the surface, it is possible to calculate relative concentrations (C_a) of all present species. This is accomplished by comparing the AES signal intensity (I_x) and instrument sensitivity factor (S_x) for each element present by following the equation 2.2. Sensitivity factors for each element investigated were taken from the Phi Handbook of Auger Electron Spectroscopy.[66] A comprehensive list of sensitivity factors pertaining to this dissertation can be found in Table 2.1.

$$C_a = \frac{I_a / S_a}{\sum (I_x / S_x)} \quad (2.2)$$

2.2.4 X-ray Photoelectron Spectroscopy

X-ray photoelectron spectroscopy (XPS) is a core level technique that is based on Einstein's photoelectric effect, which states that a solid will emit electrons when hit with light (photon). If an incident photon's energy (hν) is greater than or equal to the binding energy (BE) of an electron, that electron can be ejected from the surface and detected by a hemispherical analyzer (Figure 2.6). The measurable Kinetic Energy (KE) is equal to the difference of hν and BE. The relative concentration of a species is related to the photoemission peak area and its atomic sensitivity factor. Equation 2.2 can be used to calculate the relative concentration (C_a) of a species by substituting peak area for signal intensity and using the appropriate XPS atomic sensitivity factor.

XPS also has the capability of determining the oxidation state of a material as the BE of core electrons is affected by changes in charge due to chemical or structural changes.[65] Unfortunately, due to the resolution of the analyzer (11.4 mV, VSW 100) combined with the natural line width of the x-ray source (~1 eV, TX 400/2), peaks with small differences in binding

energy may not be fully resolved. In order to elucidate the different species that may be contained within the peak or exist as shoulders of the main peak, the spectrum can be fit using a non-linear least squares method. Fitting of the data presented herein was performed using Presents software (Oxford Applied Research). A Shirley background was applied to remove the signal caused by inelastically scattered electrons emerging from the bulk of the sample.[65] The resulting data was then fit with Gaussian-Lorentzian shapes to represent the peak shape, area, and intensity of the individual components within the overall spectrum. There are several factors that can be manipulated (i.e. peak position, height, FWHM, and splitting) during fitting and if care is not taken can produce features that are not real. Therefore, is important to have a general understanding of the surface composition prior to fitting.

Experiments described in this dissertation use un-monochromatized x-ray source (PSP Vacuum Technology, TX400/2) producing Al K_α (1486.6 eV) radiation. The source is mounted on a linear drive to avoid interference with other instruments in the chamber. The sample is positioned normal to the analyzer at a distance of ~4 cm with the analyzer at an angle of 43° to the surface. The emitted electrons were detected using a 100 mm hemispherical analyzer (Oxford Applied Research, VSW 100). All data acquisition was computer controlled by the Spectra software (Oxford Applied Research). Specific parameters will be discussed in the appropriate sections later in this dissertation.

2.2.5 Ion Scattering Spectroscopy

Ion scattering spectroscopy (ISS) is a surface sensitive technique used to characterize the species present in the top one or two atomic layers. This is the main advantage that ISS has over the previously discussed spectroscopic techniques which both probe several layers deep. ISS is a relatively simple technique that relies on the principles of a two body elastic collision and the

conservation of energy and momentum. An incident ion strikes the surface with a known energy and then scatters back with a loss of energy depending on the mass of the surface atom at which the collision took place. The resulting scattered ion is then collected with a hemispherical analyzer and a spectrum of intensity versus kinetic energy is obtained. The energy of a surface atom (E_1) can be calculated by the following equation:

$$\frac{E_1}{E_0} = \left[\frac{1}{(1+A)^2}\right]\left(\cos\theta \pm \sqrt{A^2 - \sin^2\theta}\right)^2 \quad (2.3)$$

where E_0 is the energy of the incident ion, A is the mass of the surface atom divided by the mass of the incident ion, and θ is the scattered angle measured from the direction of the ion beam. Due to the high energy ions that are used, some of the incident ions will not only be scattered to the detector but will cause some atoms on the surface to be sputtered away and removed from the surface. Experiment specific details will be discussed in Chapter 4.

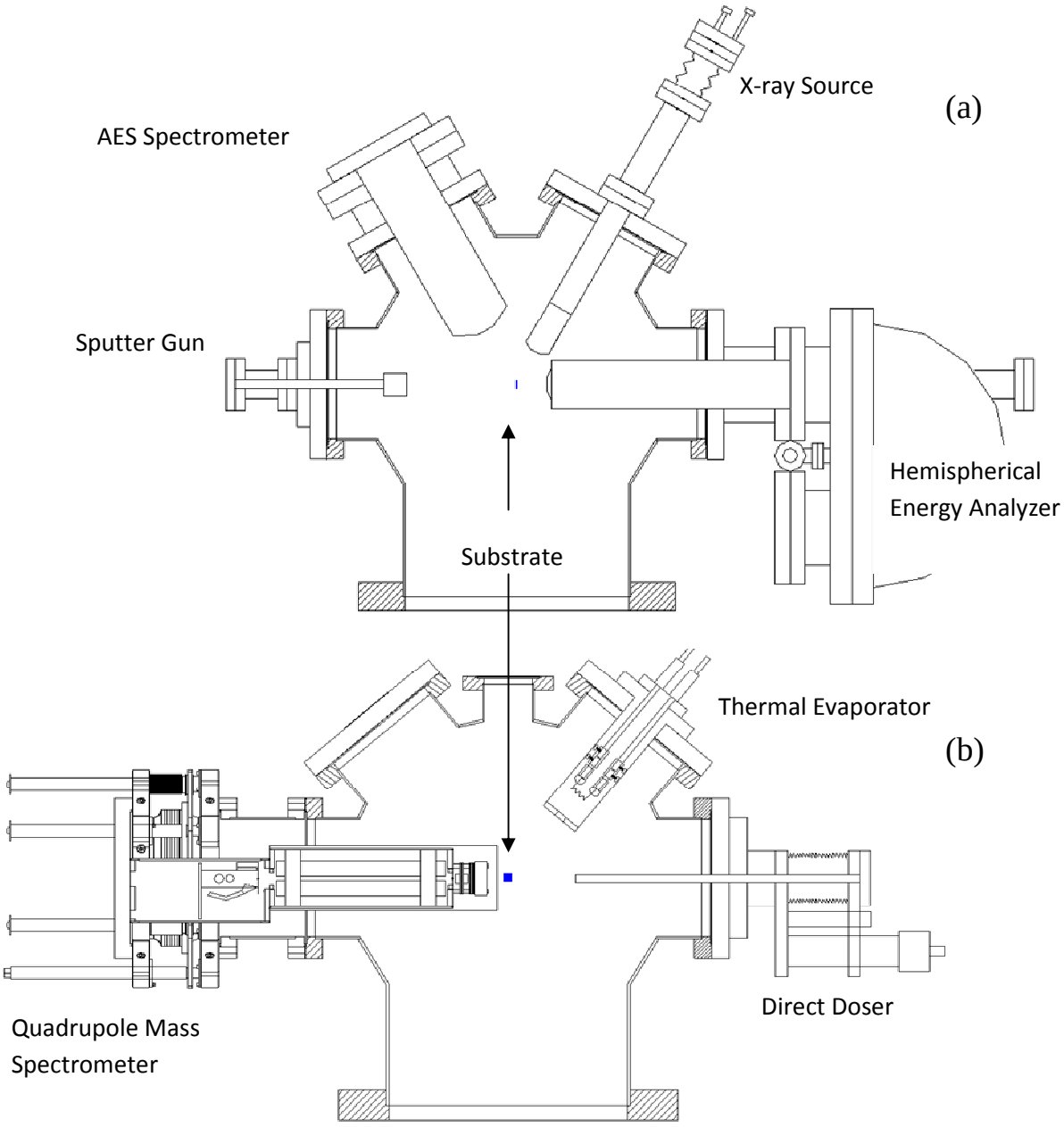

Figure 2.1: Schematic of (a) upper level and (b) lower level of the UHV chamber.

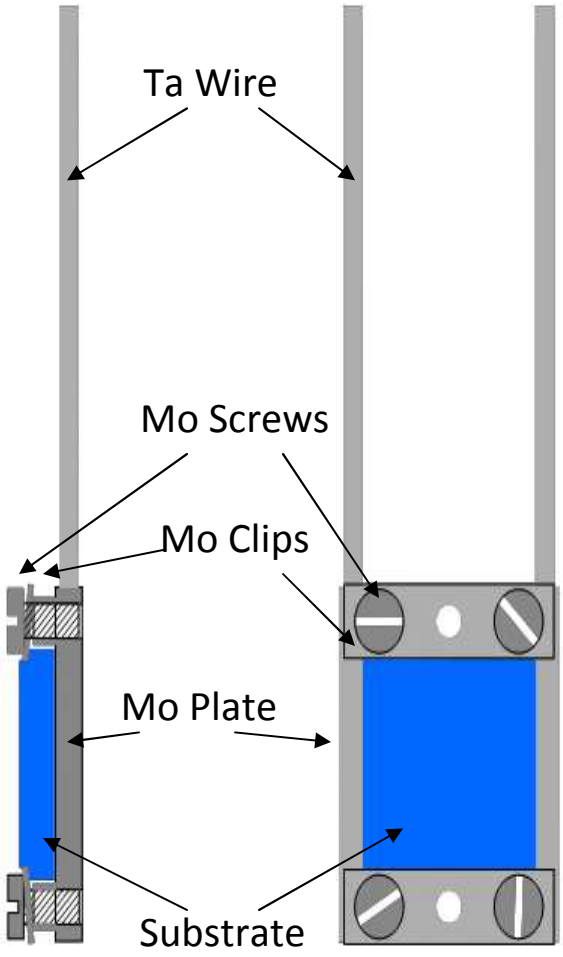

Figure 2.2: Schematic of the substrate holder. The Ta wires were attached to copper blocks that are coupled to the vacuum feedthrough. The setup allowed for the substrates to be LN_2 cooled and resistively heated. Not shown is the 0.010" thick Au foil that is placed between the substrate and Mo plate to improve thermal contact.

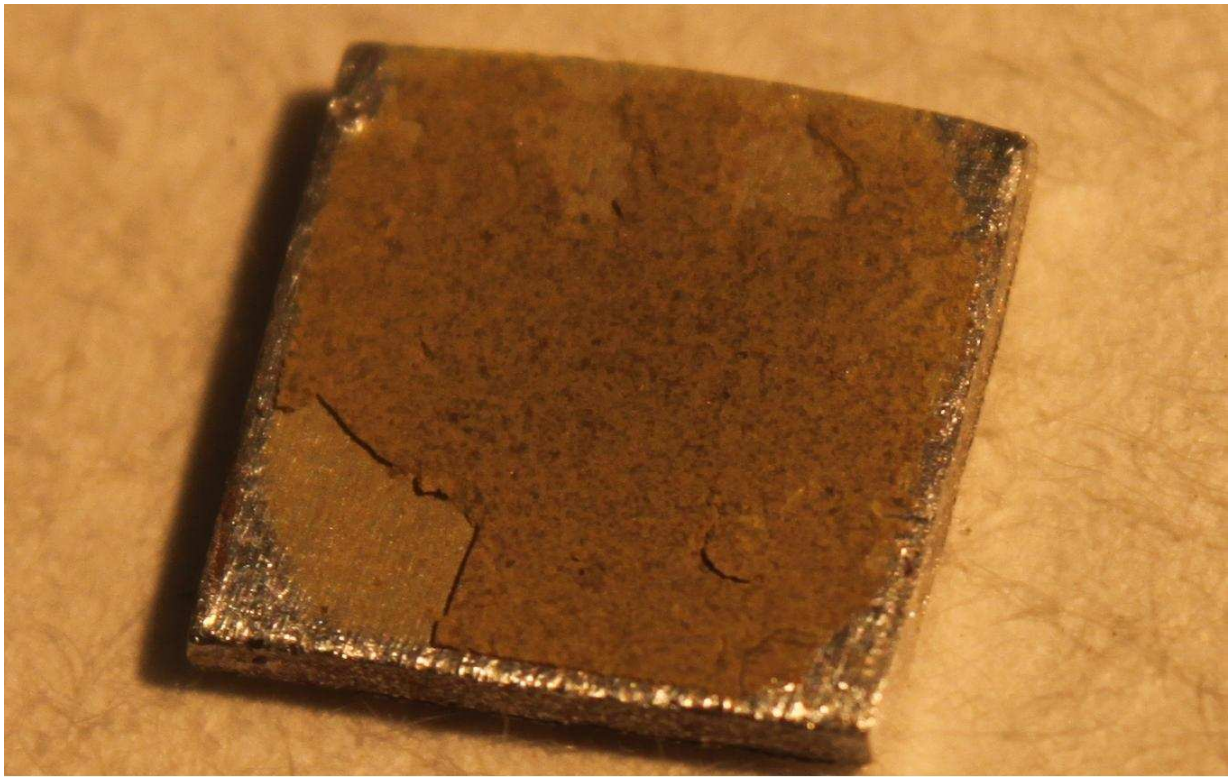

Figure 2.3: Photograph of $SrTiO_3$: Rh (1 mol%) powder pressed onto Al plate

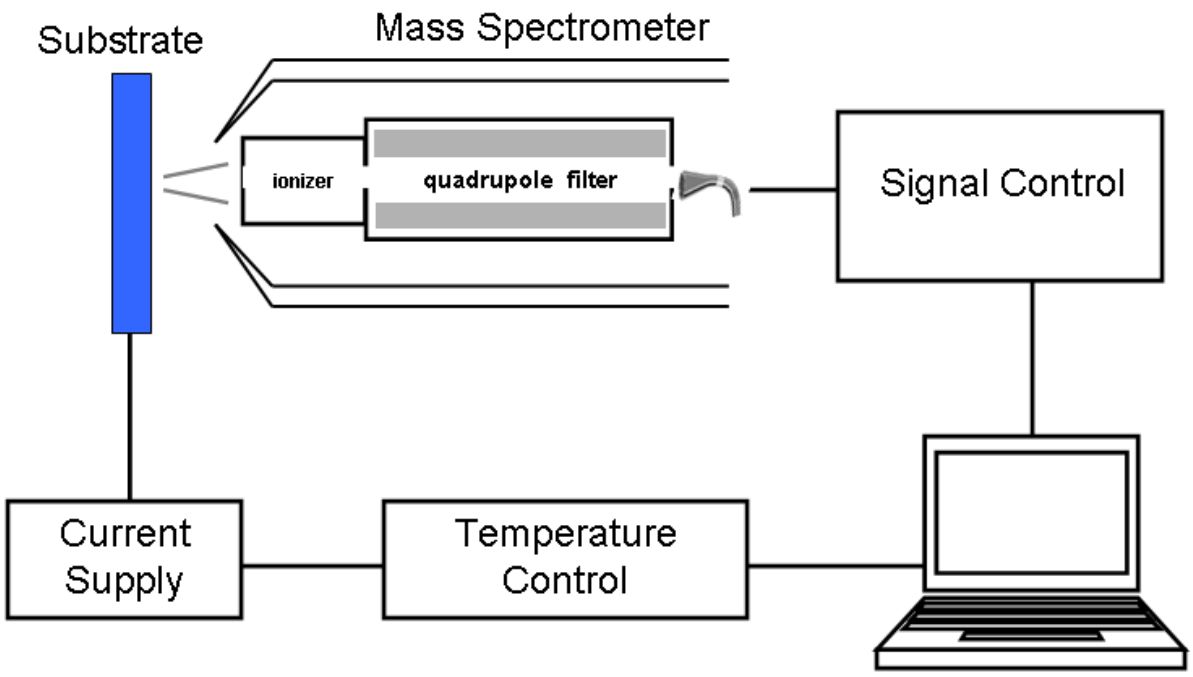

Figure 2.4: Schematic of the TPD set up. Typical ionizer emission is 0.2 mA with an electron beam energy of 70 eV. Typical multiplier value is 2500 V.

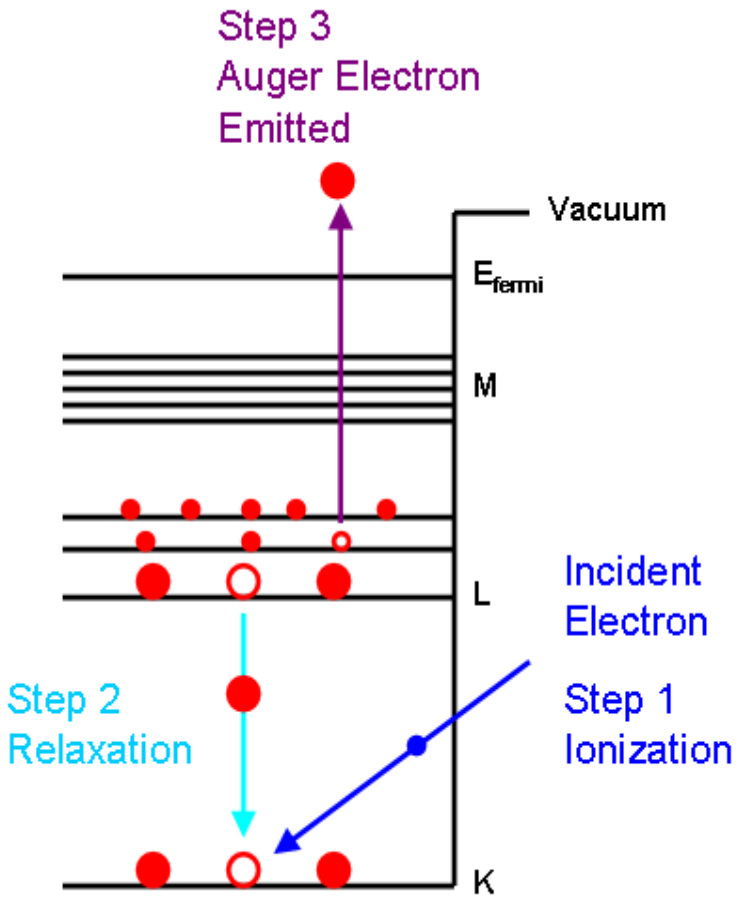

Figure 2.5: Schematic of the Auger process.

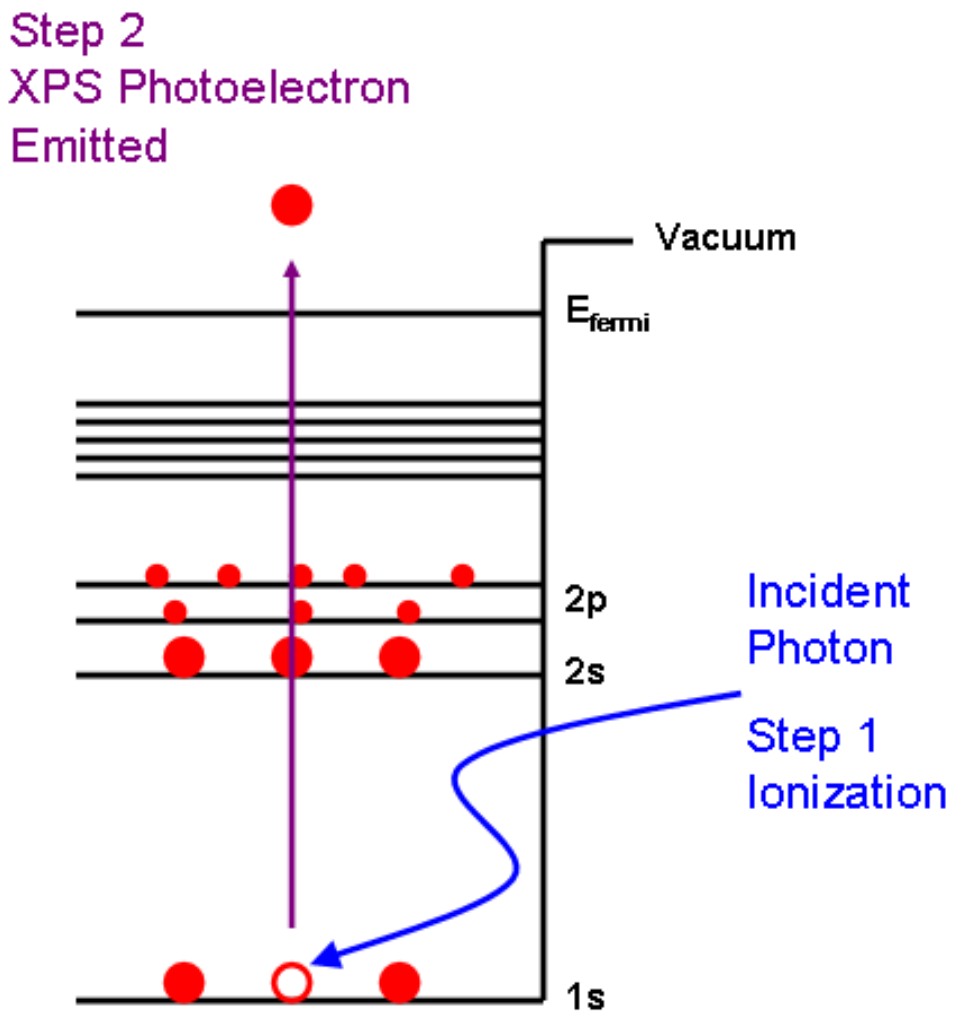

Figure 2.6: Schematic of the photoelectron process as it pertains to XPS.

Element	AES Transition (KE)	AES Sensitivity Factor[66]	XPS Sensitivity Factor[67]
Cu	LMM (920 eV)	0.9688	4.3 ($2p_{3/2}$)
Au	NVV (71 eV)	2.3433	N/A
Ce	NOO (87 eV)	1.6425	12.5 (3d)
Ti	LMM (390 eV)	1.2155	1.1 ($2p_{3/2}$)
O	KLL (510 eV)	1.2571	0.63 (1s)
La	NOO (83 eV)	1.4501	6.7 ($3d_{5/2}$)
N	N/A	N/A	0.38 (1s)
Rh	N/A	N/A	1.75 ($3d_{5/2}$)
Sr	N/A	N/A	1.05 (3d)

N/A = Not Applicable for this dissertation

Table 2.1: Summary of AES transitions, AES sensitivity factors, and XPS sensitivity factors for all elements investigated throughout this dissertation.

Chapter 3

3. A Surface Science Study of TiO_2 Supported Au and Cu Nanoparticles

3.1 Introduction

Since Honda and Fujishima discovered the ability of titania to photocatalytically split water[48], it has been used in everything from heterogeneous catalysis[36] and solar cells[30] to self-cleaning fabrics[41] and sunscreen.[40] TiO_2 has been extensively studied both under controlled environments (UHV) and under high pressure to understand its physical and chemical properties. Despite all of these efforts, questions still exist as to what allows this material to perform under various conditions. A recent review highlights the numerous studies that have been carried out on TiO_2 systems and their efforts to understand even the basic interactions of oxygen on the surface.[39]

TiO_2 has been found to be catalytically active without the addition of a dopant or metal particles. Kim and Barteau have shown that ethanol, n-propanol, and isopropanol adsorb associatively and dissociatively on the Ar^+ sputtered TiO_2 (001) surface. The dissociated species desorbed from the surface either recombined to form the parent alcohol or partially decomposed to olefins and aldehydes.[68] The TiO_2 (110) surface has also been shown to partially photo-oxidize CH_3Cl to H_2CO, CO, HCl, and H_2O in the presence of a limited amount of O_2. On the other hand, P-25 powder can fully oxidize CH_3Cl to CO_2, HCl, and H_2O in an excess of oxygen. Neither sample was able to photo-oxidize methyl chloride without the initial creation of oxygen vacancies, created by annealing at high temperatures (800 – 900 K).[69] Diebold and co-workers have shown that the different phases of titania (rutile and anatase) react with simple probe

molecules, such as water, differently.[70] The authors found that an anatase surface cannot form the oxygen vacancies that are known to dissociate water, which gives rise to a high temperature recombination peak, observed via TPD, on the rutile surface.[70-72] This is just a small sample of the thousands of papers involving the use of TiO_2 as a catalyst. However, they represent differences in adsorbate interactions, which highlight the complex nature of TiO_2 and the need for further studies of its interaction even with the simplest molecules.

The addition of metal particles has been shown to enhance titania's catalytic activity and selectivity.[17, 26, 73] Of particular interest in this work is the addition of Au and Cu nanoparticles, which have shown enhanced performance for the WGS reaction. Shekhar and co-workers showed that gold particles supported on rutile TiO_2 powder had a 20 fold increase in the production of H_2 under a flow of a standard WGS mixture (CO, H_2O, CO_2, H_2, and Ar) compared to Au/Al_2O_3.[35] It was found that there was a direct correlation between Au particle size and rate of H_2 production for both oxide surfaces. The highest rate was associated with the smallest particles and a decrease in H_2 production rate of more than an order of magnitude was seen as particle sizes increased from ~1 to 7 nm. This trend was attributed to a decrease in the number of coordinatively unsaturated edge and perimeter sites, which FTIR showed were predominately metallic Au.[35] These metallic gold corner sites were also seen by Williams and co-workers, using TEM and a similar reaction rate study as described above.[74]

Rodriguez and co-workers have also shown that the Au nanoparticles supported on a rutile TiO_2 (110) single crystal are highly active for the WGS reaction.[27] This system has a lower activation energy for the WGS reaction than Au/ZnO, Cu/ZnO, Cu (100), and Cu (111). This lower activation energy was directly correlated to better H_2 production. The only system studied that had a lower activation energy was that of Cu nanoparticles supported on a TiO_2

(110) single crystal. The authors found a decrease of ~2 kcal/mol for this Cu/TiO_2 system compared to the Au/TiO_2 system and ascribed this change to a stronger Cu – titania interaction that results in smaller average particle size.[14, 27] As with Au nanoparticles, this smaller Cu particle size has been found both experimentally and theoretically to have an increased number of under coordinated, mainly metallic, sites.[36, 75]

In this chapter, TiO_2 (110), Au/TiO_2 (110) and Cu/TiO_2 (110) systems were investigated for their interaction with water and carbon monoxide and stability as a model catalyst for the WGS reaction. Studying these systems under UHV conditions helps to determine how the nanoparticles and oxides interact with each other and how the probe molecules (D_2O and ^{13}CO) react with the systems as a whole, in a clean and controllable environment. D_2O was found to bind predominately to the oxide and only dissociate on a surface that contained oxygen vacancies. On the other hand, ^{13}CO binds mainly to the metal nanoparticles deposited on the surface to temperatures up to ~300 K. Heating the nanoparticle containing systems resulted in a reduction of ^{13}CO adsorption.

3.2 Experimental

The experiments in this section were conducted in the UHV chamber on a TiO_2 single crystal detailed in section 2.1 using TPD and AES as detailed in section 2.2 of this dissertation. Briefly, Au and Cu nanoparticles were deposited on a rutile TiO_2 (110) single crystal, which was cleaned daily via sputtering and annealing in an oxygen atmosphere, using a homemade thermal evaporator. These systems were then dosed with D_2O and/or ^{13}CO, at ~110 K, and studied using temperature programmed desorption to investigate their thermal stability and interaction with D_2O and ^{13}CO. Isotopically labeled ^{13}CO (m/e = 29; Cambridge Isotopes) and D_2O (m/e = 20; Sigma Aldrich) were used to avoid interference from background CO (m/e = 28) and H_2O (m/e =

18) in the vacuum chamber. The ^{13}CO was used as purchased, while the D_2O was subjected to three freeze-thaw cycles to remove any dissolved gases. Both the oxidized and reduced surfaces of TiO_2 were investigated. The reduced surface was created by annealing the crystal at 850 K in vacuum for 10 minutes.[76]

Auger electron spectroscopy was also employed to monitor crystal cleanliness and determine metal to oxide ratios after deposition. The experiments were carried out with an incident energy of 3.0 keV which excited the Au (NVV, 71 eV), Ti (LMM, 390 eV), O (KLL, 510 eV), and Cu (LMM, 920 eV) Auger transitions.[77, 78] The surface concentrations of Au, Ti, O, and Cu atoms were determined using the Auger signal intensities corrected for their relative sensitivity factors(Table 2.1) as per equation 2.2.[66]

3.3 Results and Discussion

3.3.1 D_2O TPD from TiO_2, TiO_{2-x} Au/TiO_{2-x}, and Cu/TiO_{2-x}

Figure 3.1 shows the desorption of D_2O, mass 20, from a fully oxidized TiO_2 (110) single crystal as a function of exposure time. This surface produces three distinct features centered at 155 K, 175 K, and 270 K. The initial low coverage dose (0.1 Torr, 2 mins) produced a peak centered at 285 K. This peak grew in intensity and shifted to 270 K as the dose was increased and saturated at a dose of ~0.4 Torr for 2 mins. Though this peak seems to gain in intensity with a further increase in exposure, this is due to spillover from the two lower temperature peaks. This peak is thus assigned to molecularly chemisorbed water. A new feature appears at a dose of 0.2 Torr at 175 K and follows the same behavior as the peak centered at 270 K and is assigned to the presence of a second layer of water. Finally, a new feature appears at a dose of 0.3 Torr, is centered at 155 K, which increases with exposure and never saturates. This peak has been

assigned to desorption of multilayer water. These features and assignments are in agreement with those previously published.[71, 72, 79, 80]

The reduced TiO_2 (110) surface, produced by annealing in vacuum, displayed a spectrum that was similar to that described above for the fully oxidized surface. The two main differences were the overall reduction in adsorbed water and, more notably, was the presence of a new feature at 480 K (Figure 3.2). This peak has been assigned to the recombination of dissociatively adsorbed water at oxygen vacancies.[71, 79] Using the area of this peak and comparing it to that of the saturated chemisorbed peak (270 K) one can determine the percentage of oxygen vacancies present on the surface. The surface used in these experiments showed a concentration of ~3% oxygen vacancies. The highest reported concentration is ~7-10%, which was achieved by further bulk reduction of the crystal using high temperature sputtering and annealing cycles.[79] No attempt was made to increase the number of oxygen vacancies because the crystal was sufficiently conductive to allow for electron spectroscopy experiments.

Figure 3.3 shows a comparison of the D_2O TPD spectra between bare reduced TiO_{2-x}, ~0.5 ML Au/TiO_{2-x}, and ~0.5 ML Cu/TiO_{2-x}. The addition of Au and Cu nanoparticles greatly reduces the overall adsorption of water, especially molecular chemisorbed water (peak at ~270 K). This change in total water adsorption is due to the metals' inability to adsorb water[81-83] as well as the overall blocking of water adsorption sites on the oxide surface. The recombination peak seen on the reduced surface (Figure 3.2) is completely absent with the addition of the metal nanoparticles (not shown). This is attributed to gold and copper's preference to bind at oxygen vacancies, thus blocking its ability to dissociate water.[84-87]

3.3.2 CO TPD from TiO_2, TiO_{2-x}, Au/TiO_{2-x}, and Cu/TiO_{2-x}

The adsorption of CO was also investigated on these systems. Figure 3.4 shows the TPD spectra of ^{13}CO, mass 29, on fully oxidized and reduced TiO_2. Unlike water, oxidized TiO_2 only binds CO at a single site at a very low temperature (140 K). Annealing the surface to induce oxygen vacancies produces a shoulder that extends to ~300 K. These features have been seen previously.[42] In that work, the presence of the new feature on the reduced surface was attributed to the increased interaction of the oxygen atom of CO with the oxygen vacancy on the surface. The interaction however, is not strong enough to induce dissociation of the CO molecule or O atom exchange with the surface.[42]

Unlike water, the addition of Au and Cu nanoparticles greatly enhances the system's ability to adsorb CO. Figure 3.5 shows ^{13}CO desorption spectra for (a) ~0.5 ML Au/TiO_{2-x} and (b) ~0.5 ML Cu/TiO_{2-x}. The addition of Au produces a feature centered at 195 K and extends to just below 300 K. This peak grows and shifts to 180 K with increasing exposure. This shift is due to an increase in the repulsive forces that occur as more molecules of CO are adsorbed on the surface. This new feature is attributed to the presence of gold on the surface, which is consistent with previous work that found CO desorbs from the $Au/TiO_x/Pt$ (111) system at ~ 200 K.[88] This is in stark contrast to the weak interaction CO has on bulk gold surfaces.[89-91] This increased binding energy of nano-gold has made it a highly studied CO oxidation catalyst,[92-94] which is one of the key features that make Au/TiO_2 a promising WGS catalyst.

Carbon monoxide desorption from ~0.5 ML Cu/TiO_{2-x} (Figure 3.5b) displayed similar characteristics to ^{13}CO desorption from Au/TiO_{2-x}. At a dose of 0.025 Torr for 30 seconds there are two distinct peaks in the TPD spectrum. There is a peak at 185 K that grows with increasing exposure and saturates at a dose of 0.2 Torr for 30 seconds. There is a second smaller feature

centered at 260 K and saturates at a dose of 0.05 Torr for 30 seconds. Though this peak seems to gain intensity with a further increase in dose, this is due to intensity spillover from the peak centered at 185 K and this increase is not significant. These peaks have been assigned to CO desorbing from Cu nanoparticles and/or the particle-substrate interface. This is consistent with CO desorption (~200 K) for Cu (111) and (110) surfaces.[95, 96] A new low temperature peak begins to grow in (first as a shoulder to the 185 K peak) at a dose of 0.1 Torr for 30 seconds. This peak is similar to that seen in the Au/TiO_2 system and the bare TiO_2 surface and is assigned to the weak interaction of CO on TiO_2.

The thermal stability of the deposited metal nanoparticles was studied by monitoring changes in their CO desorption profiles. Figure 3.6 shows the effect that annealing temperature has on (a) Au/TiO_2 and (b) Cu/TiO_2 systems. Spectra were obtained sequentially by increasing the final temperature of each preceding TPD scan. Both systems show a decrease in signal from the high temperature feature (assigned to CO on the metal nanoparticles) and a corresponding appearance and growth of a feature centered at 140 K (assigned to TiO_2) as the annealing temperature increases. Though it appears that the Au and Cu nanoparticles are undergoing the same change, AES (figures 3.7 and 3.8 respectively) studies show that each system behaves differently with increasing temperature. Figure 3.7 shows minor changes in the overall differentiated AES spectra of the as deposited and 700 K flash annealed Au/TiO_{2-x} sample. In fact the Au/Ti ratios that were calculated were nearly identical. This result is consistent with Au particles undergoing agglomeration to form larger 2D particles. This leaves the relative amount of exposed Ti the same before and after annealing but increases the particle size, thus reducing the number of exposed under coordinated Au atoms. If the particles were undergoing 3D particle formation then the number of exposed Ti atoms would increase thus reducing the Au/Ti ratio,

which is not seen. This process has been seen previously via XPS, STM, and ISS, which have all shown that Au particles on TiO_2 undergo Oswald ripening (small particles get smaller and large particles get bigger).[84, 97-101] On the other hand, Cu nanoparticles exhibit a change in AES ratios as they are flash annealed to higher temperatures. As seen in Figure 3.8 the Cu/Ti ratio increases from 400 – 550 K, at which point the ratio begins to decrease, ultimately reaching a value below that of the as deposited sample. This means between 400 and 500 K the 3D Cu nanoparticles may begin to break apart and cover more of the surface before new larger particles are formed. This formation of more, smaller particles would account for the change in Cu/Ti ratio as they would cover previously exposed surface Ti atoms thus increasing the Cu/Ti ratio. Similar behavior has been seen for Cu and Fe particles supported on TiO_2 with the addition of O_2.[102] It is possible that there is enough reactive oxygen on the surface of our reduced titania, that once thermally activated, may begin to induce particle dissociation. However, as the temperature increases beyond 550K, the Cu follows standard 3D island formation as previously seen,[103] with the formation of the new, larger 3D particles exposing more of the surface Ti, decreasing the Cu/Ti ratio.

3.3.3 Water Gas Shift Reaction

Attempts to study the WGS reaction on the bare and metal nanoparticle covered TiO_2 surfaces resulted in no detectable products. The experiments were carried out using a pulsed valve set up that delivered a mixture of ^{13}CO and D_2O by bubbling carbon monoxide through a sample of D_2O, detailed in Section 2.2.2. The crystal was maintained at 600 K which is within the operating temperature of the low temperature WGS reaction (~525 – 625 K). There were no signs of D_2, HD, $^{13}CO_2$, or CO_2. During the experiments, direct scattering of D_2O and ^{13}CO were detected, indicating that the pulsed gases were hitting the surface and being directed into the

QMS for detection. These results do not indicate that this system is not active for the WGS reaction just that these experimental conditions are not sufficient for a reaction to occur. Previous work has shown this system to be reactive under relatively low pressures of ~30 Torr , but still several orders of magnitude away from our experimental reaction pressure.[27]

3.4 Summary

In this chapter the reactivity and thermal stability of oxidized and reduced TiO_2, Au/TiO_{2-x}, and Cu/TiO_{2-x} systems have been investigated as they pertain to the WGS reaction. It has been found that water reacts mainly with the oxidized and reduced TiO_2 surface. The reduced surface, containing ~3% oxygen vacancies, had the ability to dissociate water as evidenced by a recombination peak centered at 480 K. This peak was suppressed with the addition of Au and Cu nanoparticles, which preferentially aggregate at defect sites on TiO_2.[84, 86, 87, 99] The addition of metal nanoparticles also reduced the system's ability to adsorb water, especially molecularly chemisorbed water (270 K). Bare TiO_2 surfaces, either oxidized or reduced, only show a weak affinity for CO, resulting in almost all of the molecules desorbing below 200 K. However, the addition of Au and Cu nanoparticles greatly increased the system's ability to adsorb CO, resulting in the molecule remaining on the surface to ~ 300 K.

The thermal stability of the metal nanoparticles was also investigated by tracking the changes to ^{13}CO TPD and AES as a result of increased flash annealing temperature. The Au and Cu particle systems exhibited similar changes in TPD spectra with increasing flash annealing temperature, that is, a decrease in the peak attributed to the nanoparticle (~200 K) and an increase in the low temperature peak (140 K) assigned to ^{13}CO desorbing from the TiO_2 surface. Though the nanoparticles display similar thermal stability for the adsorption of CO, they undergo very distinct sintering models when studied using AES. By monitoring the changes in the AES

spectra it is clear that Au particles are agglomerating into larger 2D islands, evidenced by the nearly identical spectra for the as deposited and flash annealed samples. However, Cu particles sinter into larger 3D islands, which is seen by the decrease in the Cu/Ti ratio. These trends have also been observed previously via XPS and STM.[2, 97, 98, 101, 103]

These systems were also tested for their ability to catalyze the WGS reaction. The use of a pulsed valve set up was employed to deliver the maximum exposure possible to the surface. All attempts resulted in no detectable hydrogen or carbon dioxide. This however does not mean that these systems are catalytically inactive, but further highlight the role that elevated pressures play in a reaction. Though a lot can be learned from studying these model systems under UHV conditions, they must be subjected to similar conditions to those that are used in an industrial setting so that we can have as much information as possible to improve the industrial catalysts.

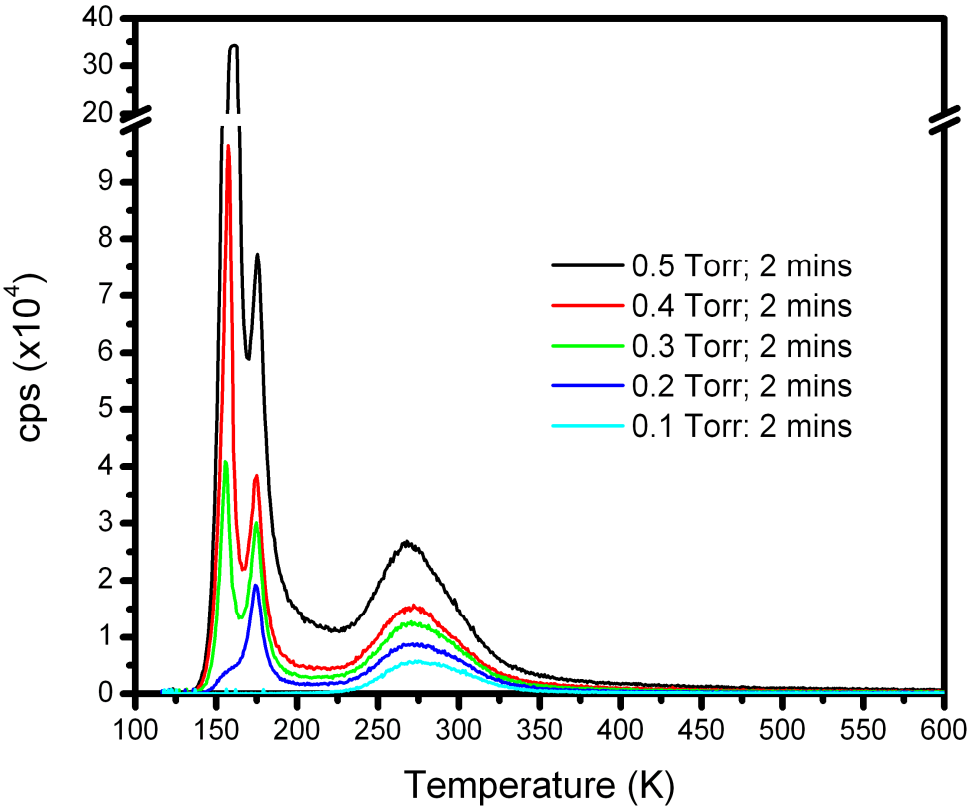

Figure 3.1: TPD spectra of D_2O coverage dependence adsorbed on fully oxidized TiO_2.

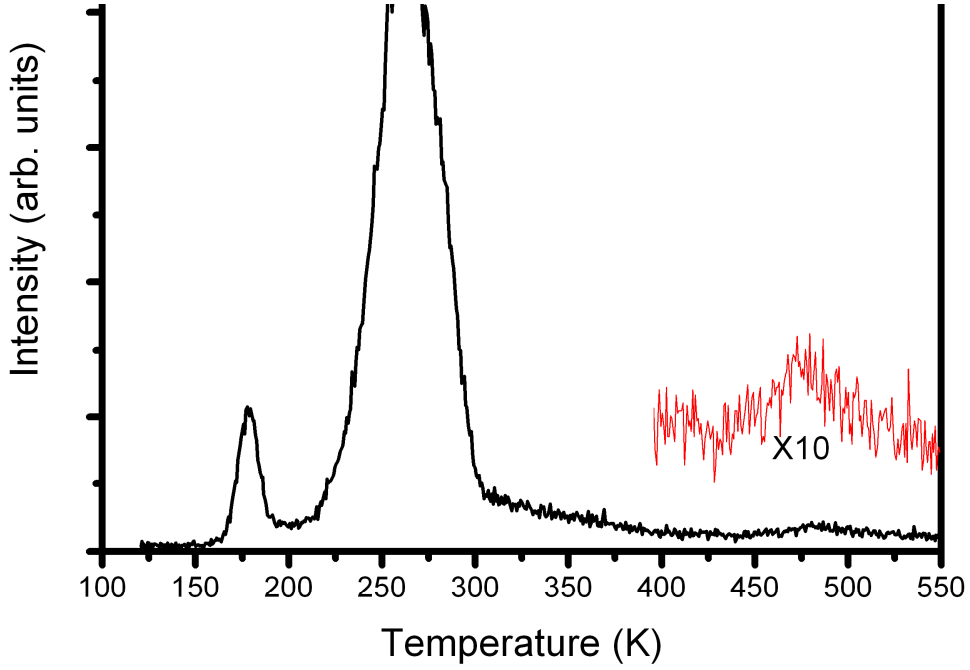

Figure 3.2: TPD spectra of D_2O adsorbed on reduced TiO_{2-x}; showing the presence of oxygen vacancies.

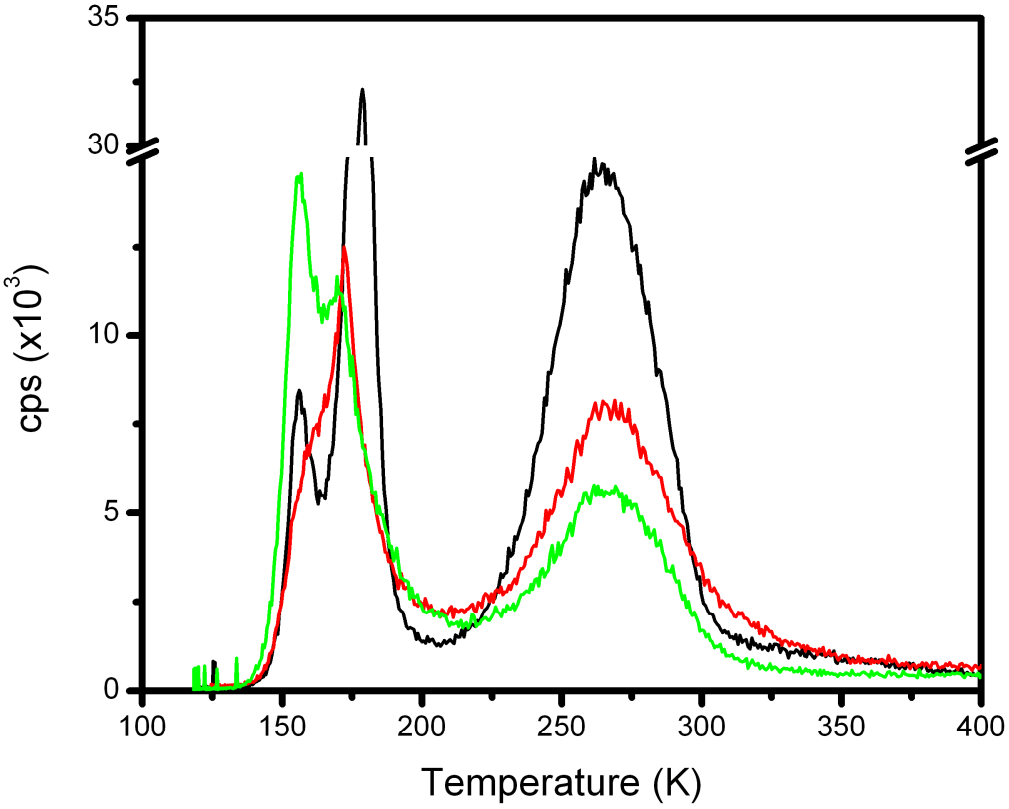

Figure 3.3: TPD spectra of D_2O adsorbed on reduced TiO_{2-x} (black), ~0.5 ML Au/TiO_{2-x} (red), and ~0.5 ML Cu/TiO_{2-x} (green). All spectra were dosed with a backing pressure of 0.1 Torr for 2 mins.

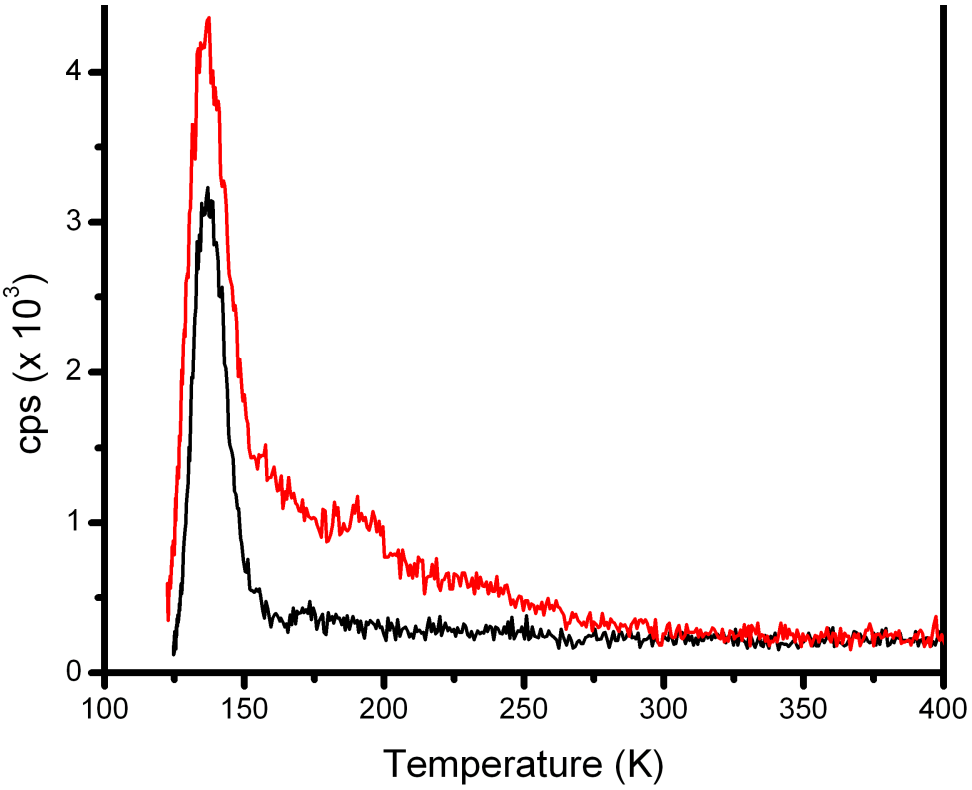

Figure 3.4: TPD spectra of ^{13}CO adsorbed on oxidized (black) and reduced (red) TiO_2. Both spectra were dosed with a backing pressure of 0.4 Torr for 2 mins.

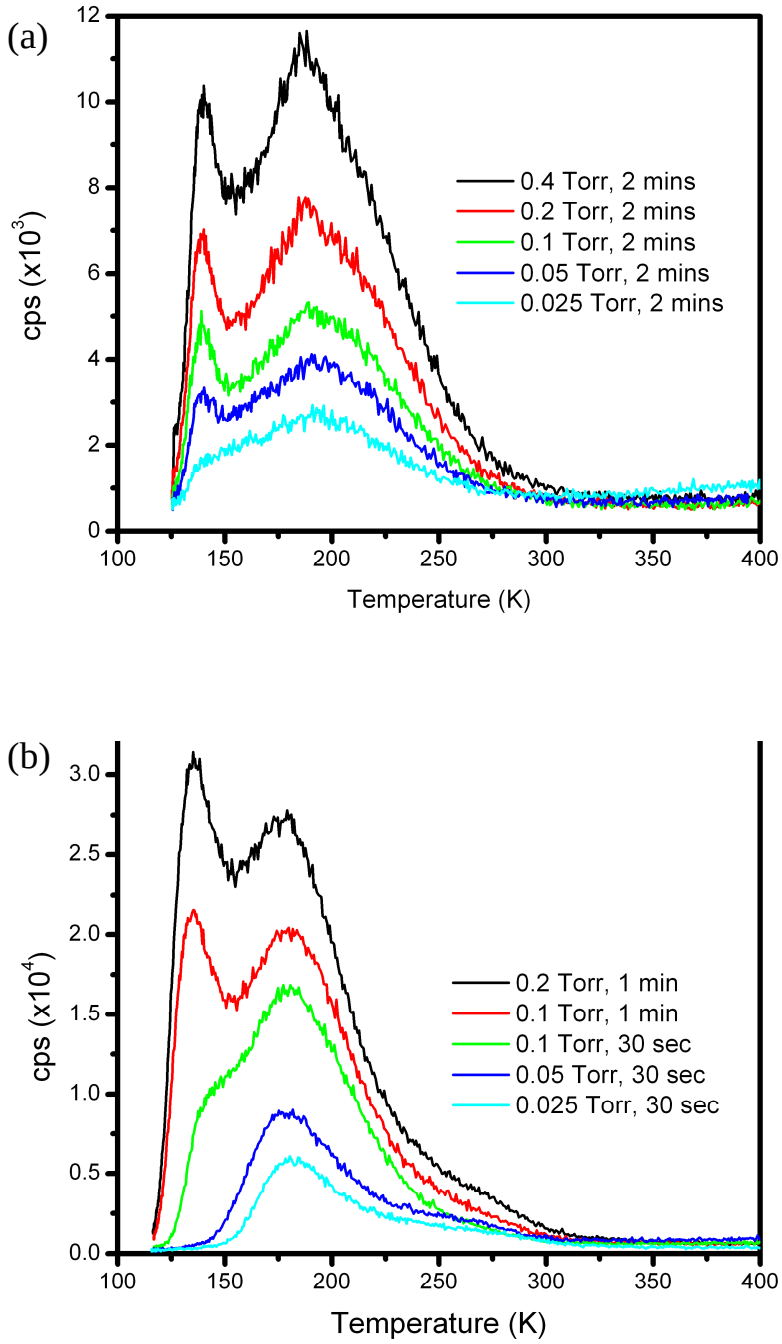

Figure 3.5: Coverage dependent TPD spectra of ^{13}CO adsorbed on (a) ~0.5 ML Au/TiO_{2-x} and (b) ~0.5 ML Cu/TiO_{2-x}. The differences in counts can be attributed to differences in multiplier settings and not necessarily an effect of Au versus Cu nanoparticles.

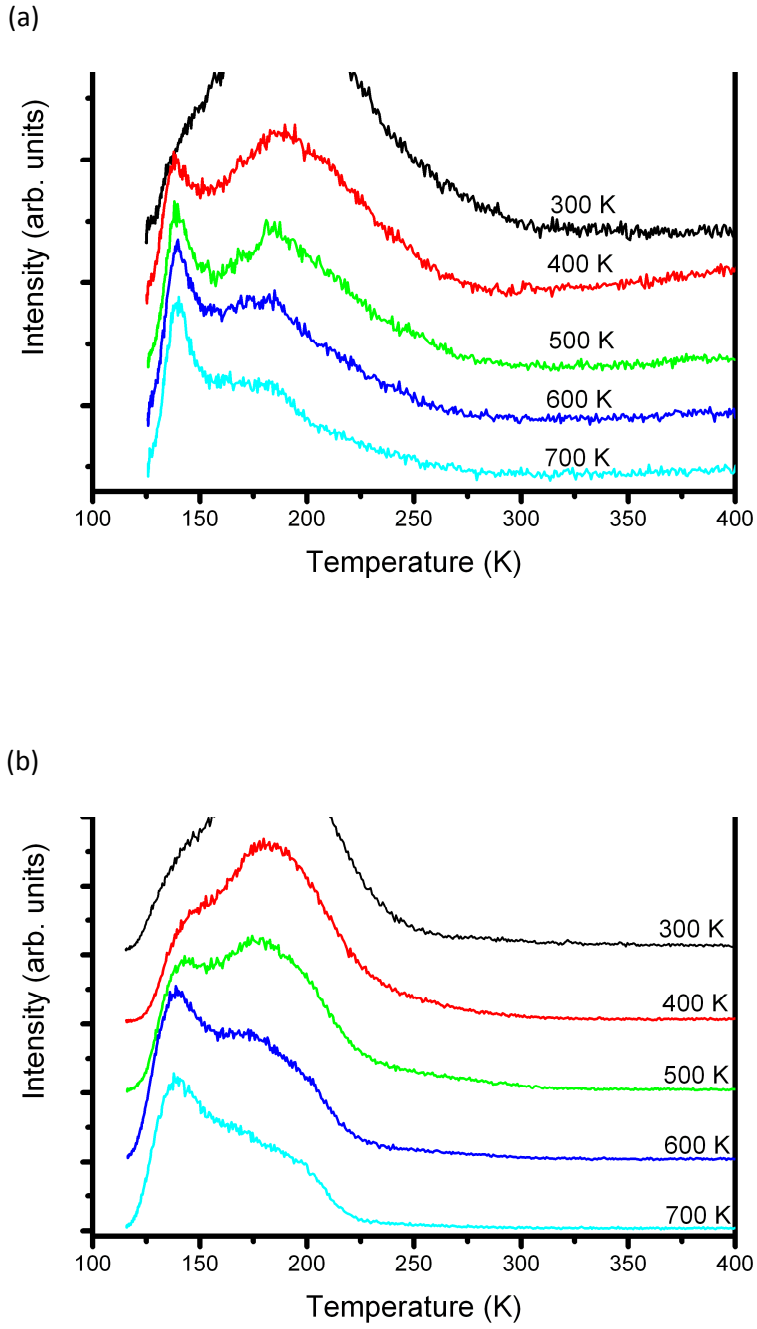

Figure 3.6: Temperature dependent TPD spectra of ^{13}CO adsorbed on (a) ~0.5 ML Au/TiO_{2-x} and (b) ~0.5 ML Cu/TiO_{2-x}.

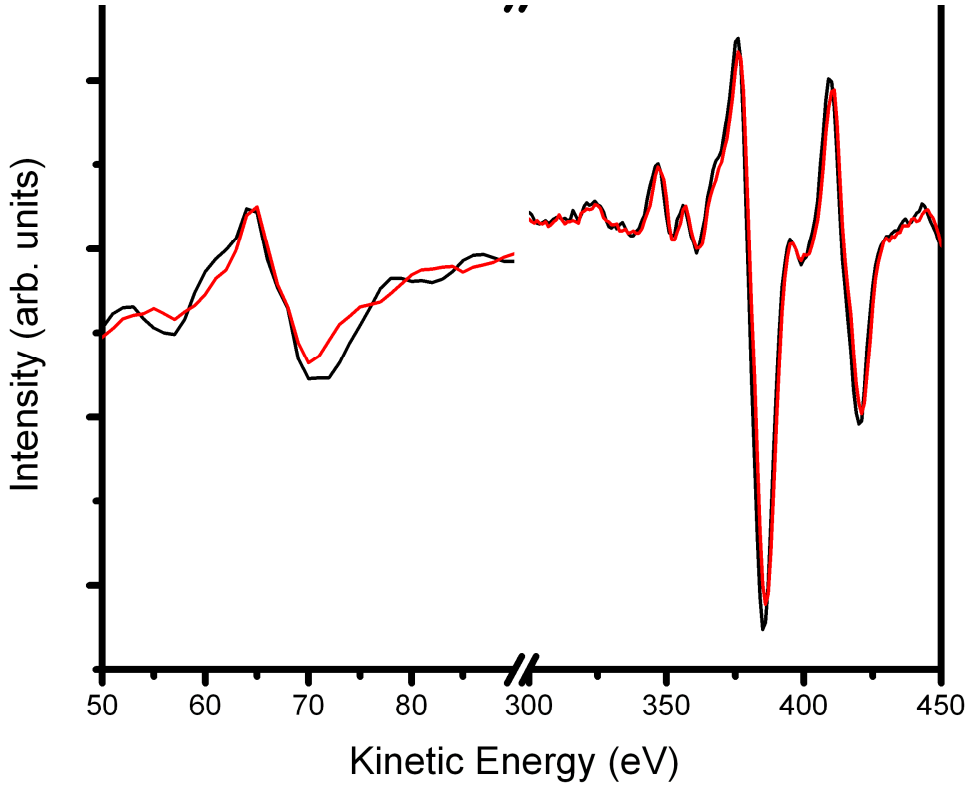

Figure 3.7: Smooth and differentiated Auger spectra of ~0.5 ML Au/TiO_{2-x} (Au NVV, 71 eV and Ti LMM, 390 eV) as deposited (black) and flash annealed to 700 K (red).

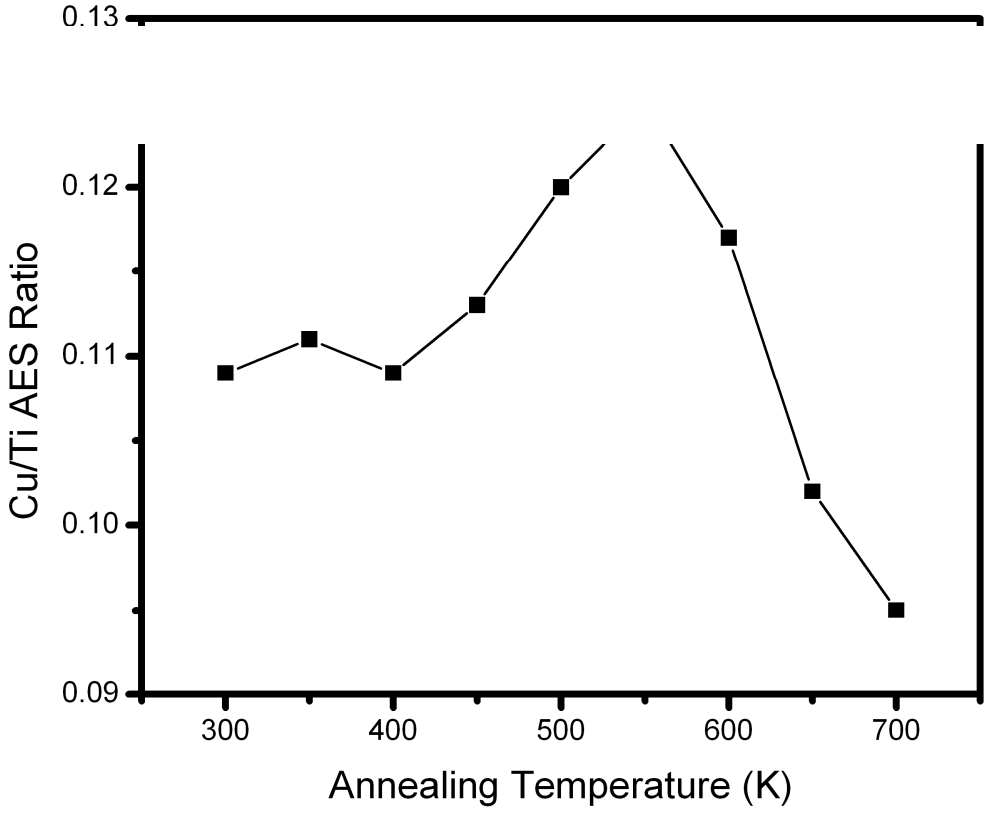

Figure 3.8: AES ratios as a function of annealing temperature for ~0.5 ML Cu/TiO_{2-x}

Chapter 4

4. A Surface Science Study of Cu on CeO_2 Thin Films: Evidence for Encapsulation

This work has been submitted for publication

4.1 Introduction

The current industrial WGS catalyst consists of Cu particles supported on a mixed Zn and Al oxide support, which operates in a temperature range of 450 – 525 K. Though this system is catalytically active it must undergo a long activation process and is pyrophoric.[13, 15, 27] Replacement of the current catalyst with materials that are more stable and similarly active is very desirable. Recent studies have identified ceria supported metal nanoparticles (Cu, Au, and Pt) as air stable and highly active WGS catalysts at a relatively low temperature (625 K).[20] The reducibility of the ceria support is thought to play an important role in the WGS reaction by allowing it to readily accept and donate oxygen atoms.[31] The presence of vacancies on the reduced surface allows the catalyst to dissociate water[104] and the oxidized surface can donate O atoms for the oxidation of CO.[105] Ceria supported nanoparticles have been studied rather extensively in high pressure systems and have been shown to produce more hydrogen than both the individual components and the industrial catalyst[13-16, 20, 31, 34, 105]

Of particular interest in this work are ceria supported Cu catalysts, which have shown superior WGS performance when compared to Cu/ZnO, Au/ZnO, single crystal Au, and single crystal Cu systems.[21] Its hydrogen production was also on par with that of Au/CeO_2, Cu/TiO_2, and Cu/MnO_2 systems.[14, 21] Previous work by Wang and co-workers was the first to show that metallic copper and the oxygen vacancies in the reduced ceria played key roles in catalytic activity of Cu/CeO_2.[33] Using a combination of *in situ* DRIFTS, time-resolved XRD, and

EXAFS, they found that metallic Cu bound to oxygen vacancies was the main source of bound CO, which than reacts with the oxide to form CO_2. Also, water was found to dissociate at the oxygen vacancies or at the Cu-oxygen vacancy interface.

Rodriguez and co-workers also showed that an inverse catalyst (metal-oxide particles deposited on a metal single crystal) of CeO_2 grown on oxygen covered Cu(111) is highly active for the WGS reaction, even more so than the more conventional $Cu/CeO_2(111)$ system.[31] In this inverse catalyst, ceria is now the supported nanoparticle rather than the support, resulting in more reduced ceria and a greater number of stabilized oxygen vacancy sites. These vacancies allow for greater dissociation of water, which is considered the rate limiting step of the WGS reaction, thus enhancing the catalyst activity.[32, 106] This outcome further proves that ceria plays an important role in the WGS reaction.[31] The role Cu plays in the reaction is not fully understood and depends on the oxide support. For highly reducible supports (i.e. CeO_2), Cu has a higher adsorption energy for CO than the support and is found to aid in the overall reduction of the surface, thus increasing the available sites for water dissociation.[32, 33] However, if Cu is supported on non-reducible oxides (i.e. $MgAl_2O_4$) then the Cu particles are responsible for the dissociation of water.

The bare ceria surface has been studied extensively under UHV conditions. Mullins and co-workers have exposed thin CeO_2 (111) films grown on Ru (0001) to various alcohols,[107, 108] ethylene glycol,[109] formic acid,[110] and acetaldehyde.[111] Each of these molecule/surface interactions showed that fully oxidized and partially reduced ceria behave differently. Product yields could be manipulated based on the amount of Ce^{3+} in the system, which can be controlled by the extent of reduction of the surface. In contrast to the bare surface, there have only been a limited number of UHV studies conducted on ceria supported nanoparticles. These studies have

focused mainly on the noble metals Rh and Pt using XPS and TPD to study the interaction of CO, C_2H_4, and/or NO.[112-116] To date there has only been one TPD study of ceria supported copper. Kolb and co-workers combined ex-situ catalyst preparation and UHV TPD techniques to explore the desorption characteristics of their $Cu/CeO_2/\gamma\text{-}Al_2O_3$ powder samples.[117] They found that higher copper loadings lead to an increase in H_2O desorption coupled with a decrease in H_2 production at temperatures above 500 K. This decrease in H_2 production combined with an increase in H_2O desorption signifies the deactivation of this system at industrially relevant temperatures. This deactivation may be due to the possible phase changes of the Al_2O_3 support that may be occurring during the experiments.[118]

In this chapter, we present a surface science study of *in-situ* deposited copper nanoparticles supported on ceria films grown on yttria stabilized zirconia, YSZ (111), as a model catalyst system for the WGS reaction. Studying this system under UHV conditions helps elucidate the interaction of copper with ceria, as well as their interactions with probe molecules, D_2O and ^{13}CO, which are involved in the WGS reaction. The present study indicates that D_2O interacts mainly with the ceria substrate and adsorbs both associatively and dissociatively with -OH remaining on the surface at temperatures above 300 K. ^{13}CO binds mainly to the copper nanoparticles, but only remains on the surface until slightly above room temperature. Furthermore, the combined TPD, AES, XPS, and ISS experiments show that ceria partially encapsulates the copper nanoparticles after annealing to high temperatures (700K).

4.2 Experimental

The experiments conducted in this chapter were carried out in the chamber and on the ceria films discussed in detail in Section 2.1 using TPD, AES, XPS, and ISS techniques discussed in detail in Section 2.2. For ISS experiments, the ceria film thickness was decreased to

100 nm and was deposited on a polycrystalline gold substrate (Princeton Scientific) to mitigate charging induced by the ion beam. To minimize film loss, the ceria films were cleaned by annealing the surface to 850 K in a background of O_2 at 2.0 x 10^{-6} Torr, unless nanoparticles were deposited, the removal of which necessitated the use of Ar^+ sputtering. Crystal cleanliness was verified daily until carbon signals were below the detectable limits of AES and negligible amounts were seen with XPS.

Copper was deposited using a homemade thermal evaporator, detailed in Section 2.2.1. Cu coverages in monolayers (ML) are estimated by assuming that a Cu monolayer would occur at a film thickness of ~2 Å which was later confirmed by XPS.[64] Runs of identical coverage were verified using the Cu/Ce ratio from either the AES or XPS spectra.

Temperature programmed desorption of ^{13}CO and D_2O were used to probe the reactivity and thermal stability of the deposited nanoparticles. Isotopically labeled ^{13}CO (m/e = 29; Cambridge Isotopes) and D_2O (m/e = 20; Sigma Aldrich) were used to avoid interference from background CO (m/e = 28) and H_2O (m/e = 18) in the vacuum chamber. The ^{13}CO was used as purchased, while the D_2O was subjected to 3 freeze-thaw cycles to remove any dissolved gases. TPD studies were conducted on fully oxidized (CeO_2) and reduced (CeO_{2-x}) ceria films. Reduced ceria was prepared by dosing 100 L of methanol at 700 K in accordance with a previously established method.[107] This resulted in a reproducible surface that contained ~40 % Ce^{3+}, which was determined by comparing the area of the peak centered at 917.5 eV to the total area of the 3d spectrum.[119]

Auger electron spectroscopy was carried out with an incident energy of 1.5 KeV which was sufficient to excite the Ce (NOO, 87 eV), O (KLL, 510 eV), and Cu (LMM, 920 eV) Auger transitions.[78] The AES spectra for the as-deposited CeO_2 films showed no sign of yttrium or

zirconium from the supporting YSZ (111) crystal. After numerous sputtering cycles, a Zr peak was observed, at which point the crystal was removed and recoated. The surface concentrations of Cu, Ce, and O atoms were determined by comparing the Auger signal intensities corrected for their relative sensitivity factors: 1.6425 (Ce), 1.2571 (O), and 0.9688 (Cu).[66]

XPS spectra were obtained using un-monochromatized Al K_α (1486.6 eV) radiation. Elemental region specific spectra were taken at an analyzer pass energy of 35 eV, step size of 0.2 eV, and dwell time of 0.5 sec. Each spectral region was signal averaged for 5 scans. Analysis of the XPS spectra was performed using Presents software (Oxford Applied Research). Each spectrum was fit with a Shirley background and an appropriate number of peaks depending on species present. The O 1s peak of 530.1 eV (CeO_2) was used to calibrate the energy scale to which all the measured binding energies were adjusted.[120] The fits were allowed to optimize without constraints as long as a reasonable FWHM (below ~3 eV) and quality of fit were obtained. In cases where a FWHM greater than 3 eV occurred, widths and/or known peak separations were fixed to one another, until an acceptable fit was achieved.

As noted above, ISS measurements were conducted on a CeO_2 film (100 nm) grown on a polycrystalline gold substrate, in order to eliminate the charging effect that occurred on the YSZ samples. Spectra were obtained using a 1 keV He^+ ion beam at an incident angle of 45º to the surface normal and the analyzer was fixed at a pass energy of 50 eV. This was the minimum incident ion energy required in order to separate the Cu peak from the peak that appears as a result of inelastic scattering. Due to the destructive nature of ISS, all XPS scans were taken prior to exposure to the ion beam. The Avantage (Thermo-Fisher Scientific) software was used to analyze ISS spectra.

4.3 Results and Discussion

4.3.1 Water TPD from CeO_2/YSZ (111)

Figure 4.1 shows the desorption of D_2O, mass 20, as a function of exposure time on fully oxidized (a) and reduced (b) ceria films. The fully oxidized surface produced three major features that appear above 200 K (255 K, 360 K, and 500 K) assigned to associative chemisorbed water, and two different recombination sites, respectively, and one minor component that appears at ~170 K and is assigned to multilayer water. These assignments are based on those that were previously reported for CeO_2 (100) thin films by Overbury and co-workers.[104] The two recombination sites both saturate over the exposures studied here; however, it is clear from the peak behavior that they originate from two distinct sites. The desorption temperature of the peak at 360 K shifts to higher temperature, indicating an attractive interaction and has an asymmetric peak shape, which is indicative of a first order reaction. In contrast, the desorption temperature of the peak centered at 500 K shifts to lower temperature. This shift, coupled with the peak symmetry is indicative of a second order reaction.

Water adsorption on a reduced ceria surface (Fig. 4.1b) was also investigated. Similar D_2O TPD features are observed, however, the desorption temperatures of these features shift slightly lower with the chemisorbed peak centered at 225 K, the low temperature recombination peak shifted to 325 K, and high temperature recombination peak shifted to 410 K. There are however, two major differences between a fully oxidized and a reduced surface. First is the decrease in overall signal intensity, which is easily seen in Figure 4.2 and has been previously observed.[104] This reduction in signal may be due to the loss of surface oxygen atoms that allow for strong H-bonding of water to the surface. Second and most notable is the presence of a new peak centered at ~700 K. At the lowest exposures, desorption in this region appears as two

peaks at 615 K and 740 K, which then appear to coalesce into a broader feature at 700 K at high exposures. This new high temperature peak is associated with water dissociation at an oxygen vacancy which has been seen both theoretically[121] and experimentally[104, 122] and is therefore only observed on reduced surfaces.

Although the water TPD peak positions in the spectra presented in Figure 4.1 are shifted to higher temperatures (~50-100 K) compared to those observed by Mullins et al. on CeO_2 (100), they nonetheless have similar shapes and relative intensities.[104] The shifts in temperature may be caused by the differences in oxide thickness and the support. Mullins and co-workers grew their films on Nb-doped $SrTiO_3$ (100) to a thickness of ~20 nm, while the films here were grown on YSZ (111) to a thickness of ~200 nm. Although thin films of ceria (<50 nm) deposited on YSZ (111)[60, 122] and doped $SrTiO_3$ (100)[104] have been shown to grow epitaxially, thicker films are likely to be amorphous with a number of different termination structures (facets) and an increased density of defects, e.g. grain boundaries, step edges, and under coordinated edges. Water binding at these structural defects may be responsible for the somewhat higher water desorption temperatures observed for the thicker films used in this work.[122] However, it is clear that our surface is not comprised of a (111) termination, which produced a lone water desorption peak at ~175 K.[122, 123]

It is also interesting to compare our water TPD results with a recent calculation by Molinari, et al. who performed DFT calculations on water adsorption and dissociation on (111), (110) and (100) surfaces of CeO_2, including the effects of coverage and surface reduction.[121] In particular, they used DFT calculated adsorption energies in an equilibrium model to predict the temperature ranges for desorption of chemisorbed water and recombination. Using their calculated results at a pressure of 10^{-10} bar for comparison, our observed TPD spectra are in

reasonable agreement with the calculated desorption temperature ranges for the (100) and (110) surfaces. Specifically, they predict that desorption of chemisorbed water occurs over the range 250 K - 300 K. These findings show our surface is composed of multiple facets consisting mainly of (100) and (110) terminations.[104, 121, 122, 124]

4.3.2 Water TPD from $Cu/CeO_2/YSZ$ (111)

Figure 4.2 shows a comparison of the D_2O TPD spectra between bare oxidized (CeO_2), bare reduced (CeO_{2-x}), and ~0.5 ML Cu/CeO_{2-x} samples. The addition of Cu nanoparticles to the reduced surface results in increased adsorption of water over all three adsorption sites compared to the reduced surface without Cu, but D_2O adsorption is still less than that of the fully oxidized bare ceria surface. Furthermore, the TPD peak positions for Cu/CeO_{2-x} have shifted to even lower temperatures than the bare reduced surface, with the strong chemisorption peak near 200 K and the first recombination peak appearing more as a shoulder with an estimated peak position of ~290 K. The increase in water desorption at low temperature for the Cu/CeO_{2-x} surface is consistent with adsorption of water on the (111) and (110) Cu surfaces (~150 – 175 K)[81, 82] and may result from a combination of water desorption directly from the Cu particles and at the Cu-CeO_{2-x} interface sites. Also, there is a broad feature centered at ~575 K which is probably related to the recombination peak observed for the bare reduced ceria surface between 600-800 K. Based on DFT calculations, the overall reduction in peak temperatures is attributed to charge transfer from the Cu particles to the ceria support which increases the electron density of the surface oxygen atoms and lowers the binding energy of water.[12] It should be noted that no D_2 was observed in any of the TPD spectra which had been seen previously.[104]

4.3.3 CO TPD from CeO_2/YSZ (111) and Cu/CeO_2/YSZ (111)

The adsorption of CO was also investigated as it is the second reactant in the WGS reaction. Figure 3 shows TPD spectra of ^{13}CO, mass 29, on bare reduced (Fig. 4.3a), ~0.5 ML of Cu on both oxidized (Fig. 3b) and reduced (Fig. 3c) ceria, and ~1 ML of Cu on reduced ceria. Unlike water, CO binds very weakly on these surfaces, with only a single desorption peak centered at 130 K on both the fully oxidized (not shown) and the reduced ceria surfaces. The only difference is the lower peak intensity on the reduced surface. Theoretical studies have shown that CO has only one weakly bound state on a bare ceria surface, with a binding energy (~0.2 eV) that is consistent with a physisorbed peak.[125-127] The calculations indicate that the lower signal intensity on the reduced surface is caused by the depletion of CO bonding sites, which contain two surface oxygen atoms, which there are fewer of on a reduced surface. Previous work has also shown that there is no CO adsorption on both oxidized and reduced ceria surfaces (single crystal and thin film) above 300 K[128, 129] and infrared spectra show evidence that CO will only adsorb below ~200 K on ceria grown on Pt (111)[130]

The addition of ~0.5 ML Cu on the oxidized (Figure 4.3b) and reduced surfaces (Figure 4.3c) results in a new broad TPD feature centered at ~200 K that extends out to 300 K, suggesting that the state of the surface plays little role in the characteristics of the deposited particles. At a higher coverage of ~1 ML (Figure 4.3d), the CO TPD peak for the ceria support is suppressed and the higher temperature TPD peak becomes much more prominent with a peak temperature centered at 175 K. The observed trend with increasing Cu coverage suggests that the broad TPD peak between 150-300 K results from CO desorption from the deposited Cu particles and/or the Cu-ceria interface. This assignment is consistent with CO desorption from planar Cu surfaces, (111) and (110), which occurs at ~200 K.[95, 96] Previous STM studies of Cu

deposition on TiO_2 and CeO_x/TiO_2 have also shown that at a coverage of ~ 1 ML, Cu is present in the form of 3D nanoparticles with a diameter of ~5 nm and does not completely cover the surface.[20, 102] Though 1 ML of Cu does not fully cover the surface it may sufficiently block CO surface adsorption sites.

Figure 4.4 shows the effects of increasing flash annealing temperature on the CO TPD spectra for the ~0.5 ML Cu/CeO_2 surface. The spectra in Figure 4.4 were obtained sequentially by increasing the final temperature of each preceding TPD scan. The TPD spectrum marked as 300 K corresponds to the as-prepared surface and is the same as that shown in Figure 4.3b. The TPD spectra remain relatively unchanged from 300 – 500 K. This indicates that Cu nanoparticles are thermally stable up to 500 K. However, once the particles are flash annealed to 600 K the broad feature begins to develop slight asymmetry toward higher temperatures. Upon flash annealing to 700 K the broad feature now develops into a distinguishable peak centered at ~250 K and extends beyond 300 K. Figure 4.5 shows the same effects for a ~1 ML Cu/CeO_{2-x} surface. This coverage was investigated to further clarify the changes we noticed in the ~0.5 ML sample. The spectrum in Figure 4.5 marked as 300 K once again corresponds to the as-prepared sample and is the same shown in Figure 4.3d. Unlike the ~0.5 ML sample, changes in the TPD spectrum can be seen at temperatures as low as 400 K, this slight asymmetry to high temperature may have been too small to notice on 0.5 ML coverage (Figure 4.4). This asymmetry increases, until 700 K, when the peak splits into two distinguishable features with maxima at ~160 K and ~280 K. However, the integrated CO desorption intensities from the as-prepared sample at 300 K and the sample flash annealed to 700 K are essentially identical. Hence, the total number of CO adsorption sites remains unchanged with flash annealing. Although STM studies of Cu/CeO_2 surfaces have yet to be published, STM investigations of vapor deposited Cu on the

similarly reducible oxide, TiO_2 (110), have reported the effects of surface heating on Cu nanoparticle size and morphology.[102, 131] Assuming similar behavior for the Cu/CeO_{2-x} surface studied here, we expect flash annealing to 700 K to result in somewhat larger 3D islands than on the as-prepared surface at 300 K. As noted above, the TPD data in Figure 4.5 suggest almost no change in total CO adsorption with flash annealing, which is consistent with a small change in Cu particle size. Nonetheless, this does not explain the changes in the CO TPD profile as the heating temperature is increased, especially for the ~1ML Cu/CeO_{2-x} surface. It is possible that the two CO desorption peaks at 160 K and 280 K in the TPD spectrum after flash annealing to 700 K are due to different facets on the "annealed" Cu nanoparticles, e.g., (111) and (100), however, previous STM studies of Cu on TiO_2 (110) surfaces do not provide any clear indication of such faceted crystallites.[102, 131, 132] Alternatively the Cu nanoparticles could be partially encapsulated by ceria, which has occurred for other metal nanoparticles supported on ceria.[133-140] The partially encapsulated surfaces might be expected to have a CO desorption temperature between bare CeO_2 (130 K; Figure 4.3a) and bare Cu nanoparticles (≥150 K) (Figure 4.3 b and c), which is consistent with the low temperature portions of the CO TPD profiles after heating to ≥600 K. The higher temperature portions of the CO TPD profiles after ≥600 K with peaks near 250 K (Figure 4.4) and 280 K (Figure 4.5) would correspond to bare portions of the Cu nanoparticles. If we assume that the portions of the ^{13}CO TPD for the 700 K flash annealed surface with ~1.0 ML are characteristic of encapsulated (100 – 200 K) and bare Cu surfaces (220 – 350K), we find that roughly 44% of the intensity can be ascribed to the encapsulated Cu surfaces. TPD measurements up to 700 K also showed no Cu loss from the surface (not shown). One possible explanation consistent with these observations is that heating to 700 K results in partial encapsulation of the Cu nanoparticles by a thin ceria layer and subsurface Cu still

influences adsorption of molecules like CO (see Figure 4.4 and 4.5). Since it is impossible to determine the effect of flash annealing by TPD alone, additional measurements were carried out using AES, XPS, and ISS studies which are sensitive to the surface atomic composition. The results are discussed below.

4.3.4 Surface Composition using AES, XPS, and ISS

A combination of AES, XPS, and ISS were used to investigate the surface atomic composition of Cu/CeO_2 surfaces that were subjected to increasing flash annealing temperatures. Figure 4.6 displays the smoothed and differentiated AES spectra of (a) the Ce (NOO, 87 eV) and (b) Cu (LMM, 920 eV) regions from ~0.5 ML of Cu deposited on oxidized ceria as prepared and flash annealed to 700 K. After flash annealing to 700 K, the Ce region shows a noticeable increase in intensity (factor of ~1.3x) indicating that the amount of Ce exposed on the surface has increased. This increase is consistent with the growth of larger 3D Cu islands, i.e., and increase in island height would expose more of the ceria surface, however, our expectations based on the CO TPD data and previous STM studies are that the size of Cu islands does not change appreciably with high temperature heating. More surprising, is the AES Cu data (Fig. 4.6b), which shows that the Cu AES signal decreases significantly after heating to 700 K. The latter observation is not consistent with the formation of 3D nanoparticles; since the concentration of surface Cu atoms would remain unchanged (some reduction in the Cu AES signal could result from the attenuated electron emission from Cu atoms in the interior of the particles if the escape depth is comparable to their height, ~1-2 nm[20]). As stated above no Cu desorption was seen over the investigated temperature range.

XPS was also used to investigate surface atomic composition as well as to monitor oxidation states of all species present. Figure 7 shows the Ce 3d region for the clean CeO_2/YSZ

(111) surface (black), after Cu deposition ~0.5 ML at 300 K (red), and after the Cu/CeO_2/YSZ (111) surface was heated to 700 K (green). The 3d spectrum for the bare surface is consistent with fully oxidized CeO_2 with the cerium atoms in the Ce^{4+} state.[120, 139-141] Deposition of Cu nanoparticles at 300 K results in a decrease in the Ce 3d intensity, consistent with some part of the ceria film being covered by the nanoparticles. The average decrease in peak intensity is ~55%, which agrees with our estimated Cu coverage of ~0.5 ML using the quartz microbalance. Consistent with the AES data in Figure 5a, the Ce 3d signal increases after heating the Cu/CeO_2/YSZ (111) surface to 700 K. The Ce 3d peaks are seen to change uniformly in intensity, indicating that Cu deposition and/or subsequent heating does not lead to reduction of the ceria film, i.e. formation of Ce^{3+}.

The XPS spectra for the Cu 2p region are shown in Figure 4.8. For both the as prepared and subsequently heated Cu/CeO_2 surfaces, the Cu $2p_{3/2}$ can be assigned to metallic copper (Cu^0). The spectra also do not show any signs of the satellite peaks associated with the presence of copper oxides.[142] After heating the Cu/CeO_2 surface to 700 K, the intensity of the Cu 2p signal decreases, similar to what was observed for the Cu AES data in Figure 5b. The better signal to noise in the Cu 2p XPS spectra, compared to the AES spectra, permits the loss of intensity to be estimated at ~ 39%. Hence, if encapsulation of the Cu nanoparticles by ceria is occurring at higher temperatures, it is only partial, with ~40% of the Cu area covered at 700 K. Moreover, the observation that neither the Cu nor Ce core levels shift after heating indicates that partial encapsulation does not induce substantial electronic modifications to either the ceria film or Cu nanoparticles.

As a final probe of the Cu/CeO_2 surface we used ISS, which has a penetration depth of only one to two atomic layers and is even more sensitive to surface composition than AES or

XPS. The ISS experiments were conducted on CeO_2 films (100 nm) grown on a polycrystalline gold substrate to reduce charging induced by the ion beam which prevented ISS measurements for CeO_2/YSZ (111) surfaces. ISS of the bare CeO_2 surface produces only one broad peak centered at ~850 eV. The addition of ~0.5 ML of Cu nanoparticles caused a new peak to appear at ~783 eV. These positions are consistent with those expected from calculations for Ce and Cu respectively. Just as with AES and XPS, there is an increase in Ce peak (850 eV) intensity and a decrease in Cu (783 eV) intensity (Fig. 4.9) upon flash annealing. It is apparent that the Ce peak is much broader than that of Cu, which we attribute to a combination of fully exposed Ce atoms and those that fall in the shadow of the surface O atoms causing ions to be scattered off Ce atoms with a larger range of kinetic energies.[47] The narrow Cu peak suggests that all of the nanoparticles are located on the surface. The decrease in the Cu ISS peak intensity after heating the surface to 700 K is ~40%, which is similar to the decrease in the Cu 2p XPS signal of ~39% noted above. This calculated decrease is greater than the 15-20 % loss that was seen due to the sputtering effect of the ISS alone. Again, these data are consistent with the Cu nanoparticles being only partially encapsulated by the ceria.

4.3.4 Water Gas Shift Reaction

As with the Au/TiO_2 and Cu/TiO_2 surfaces, attempts to conduct the WGS reaction on the bare and copper covered CeO_2 surfaces resulted in no detectable products. The experiments were carried out using the pulsed valve set up detailed in section 2.2.2 above. In addition, TPD experiments were conducted where D_2O and ^{13}CO were co-dosed on the surface. Once again there were no detectable products and the order of dosing made no difference. Dosing of D_2O and running the TPD in a background of ^{13}CO (~1 x 10^{-7} Torr) also resulted in no detectable reaction. These results do not indicate that this system is not active for the WGS reaction, just

that these conditions may not contain enough molecules with appropriate energy for reaction to take place. Previous work has shown this system to be reactive under relatively low pressures of ~30 Torr which is only 4% of an atmosphere, but still several orders of magnitude away from our experimental reaction pressure.[21]

4.5 Summary

Here we report a surface science investigation of Cu particles deposited on CeO_2 grown on YSZ (111) as a model catalyst system for the WGS reaction. TPD of D_2O and ^{13}CO provided insight in to the role that each component plays in the WGS reaction. D_2O binds strongly to both the fully oxidized and reduced surfaces of CeO_2 with recombination peaks at ~500 K and ~700 K respectively. These peaks signify that there is dissociated water (-OH) on the surface that is available for reaction. The addition of Cu suppressed some of the water adsorption but still allowed for water dissociation to occur and remain on the surface at temperatures high enough for potential reaction. On the other hand, ^{13}CO only binds on bare CeO_2 surfaces in a physisorbed state, but the addition of Cu nanoparticles allows for a new peak to appear in the range of 150-325 K depending on the Cu surface coverage and the annealing temperature.

Flash annealing the Cu/CeO_2 and Cu/CeO_{2-x} surfaces to 700 K produced significant changes in the ^{13}CO TPD, AES, XPS, and ISS spectra. Specifically, the Cu 2p XPS and Cu ISS signals showed ~40 % decrease in their respective Cu signals upon flashing annealing to 700 K, whereas the Ce XPS and ISS signals exhibit a corresponding increase in intensity. Additionally, XPS showed that cerium's oxidation state did not change before or after Cu deposition or flash annealing. Cu was deposited in the zero valent (metallic) state and remained that way even after flash annealing. The CO TPD profiles show more complex behavior with sequential flash annealing. The overall yield of desorbed CO is essentially constant, but the CO desorption

signal assigned to encapsulated Cu surfaces makes up ~44 % of the overall CO desorption intensity, which is in qualitative agreement with the ~40 % loss in bare Cu signals in XPS and ISS

This is consistent with strong metal support interaction (SMSI), which is usually explained by encapsulation of the metal particles by the oxide surface.[113] Encapsulation by ceria has been reported for Pt, Pd, Rh, Ni, and Au previously[113, 133-140] but at temperatures in excess of 700 K and usually in the presence of H_2. The temperature dependent CO TPD (Figures 4.4 and 4.5) and the temperature dependent Cu 2p XPS (not all temperatures shown) data both show that there is a continuous evolution in their spectra, which could indicate that encapsulation begins at temperatures even lower than 700 K. This means that encapsulation of Cu is kinetically controlled but is the more thermodynamically favorable state under our conditions. Whether this encapsulation actually plays an important role, either activation or deactivation, in the WGS reaction needs to be explored further.

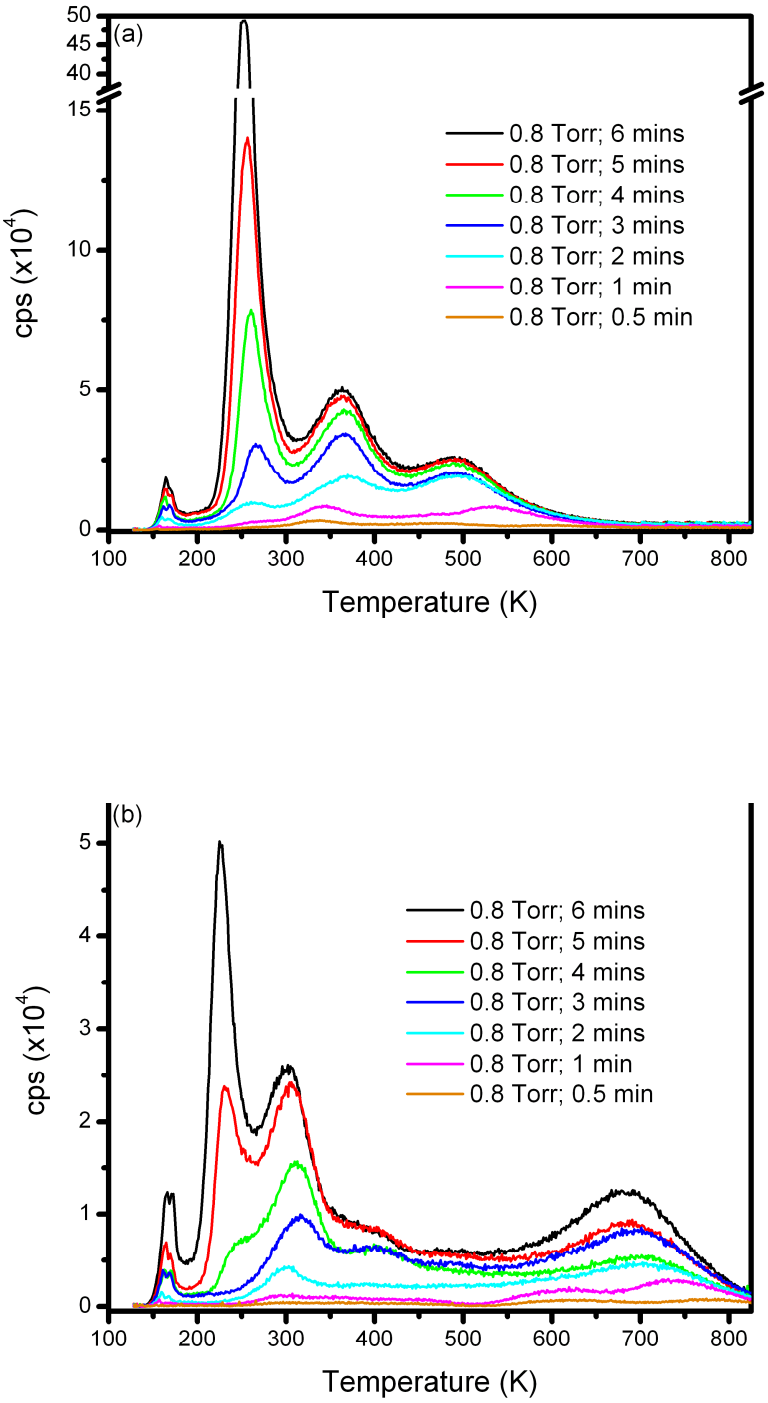

Figure 4.1: Coverage dependent TPD spectra of D_2O adsorbed on (a) oxidized CeO_2 and (b) reduced CeO_{2-x}.

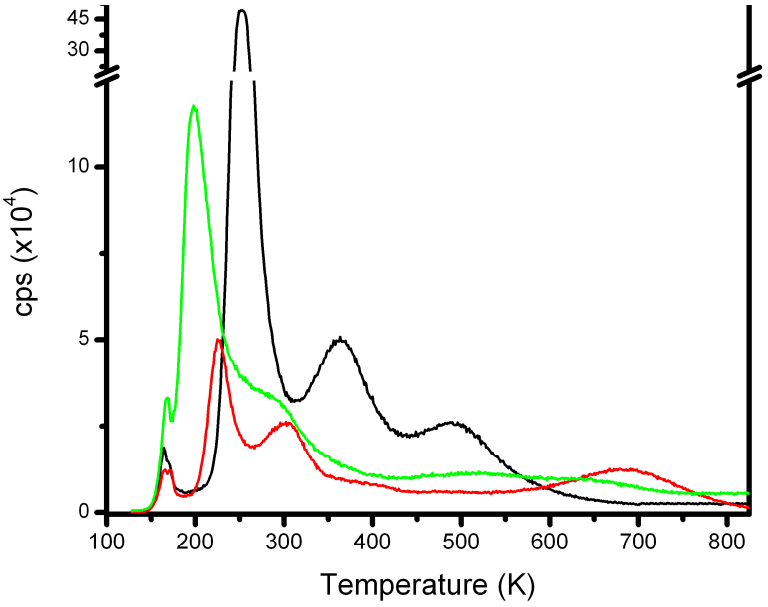

Figure 4.2: TPD spectra of D_2O adsorbed on fully oxidized CeO_2 (black), reduced CeO_{2-x} (red), and ~0.5ML Cu/CeO_{2-x} (green). All spectra were dosed with a backing pressure of 0.6 Torr for 1 min.

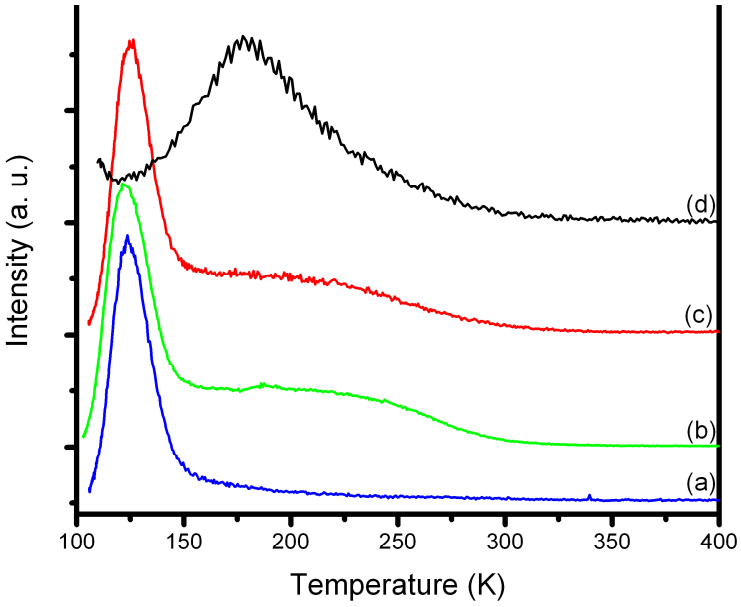

Figure 4.3: TPD spectra of ^{13}CO adsorbed on (a) CeO_{2-x} (blue), (b) ~0.5 ML Cu/CeO_2 (green), (c) ~0.5 ML Cu/CeO_{2-x} (red), and (d) ~1.0 ML Cu/CeO_{2-x} (black). All spectra were dosed with a backing pressure of 0.6 Torr for 4 mins.

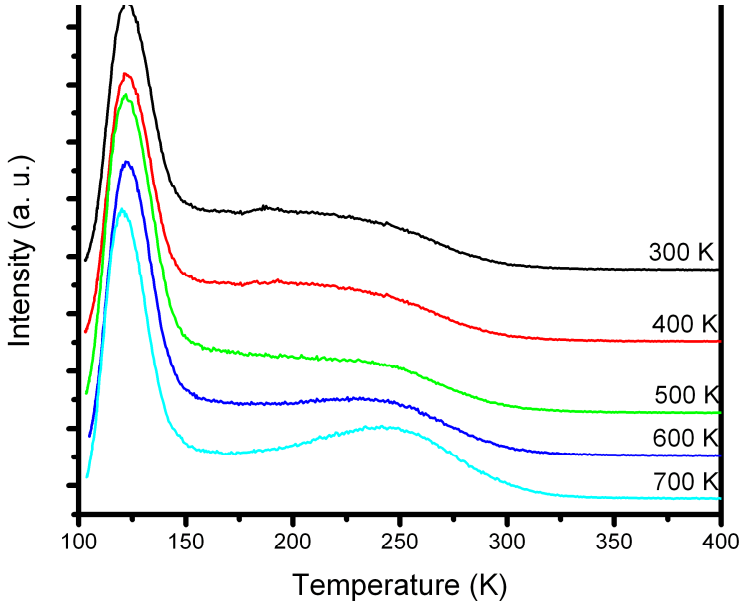

Figure 4.4: Temperature dependent TPD spectra of ^{13}CO adsorbed on ~0.5 ML of Cu/CeO_2. As prepared (black), flash annealed to 400 K (red), 500 K (green), 600 K (blue), and to 700 K (cyan). All spectra were dosed with a backing pressure of 0.6 Torr for 4 mins.

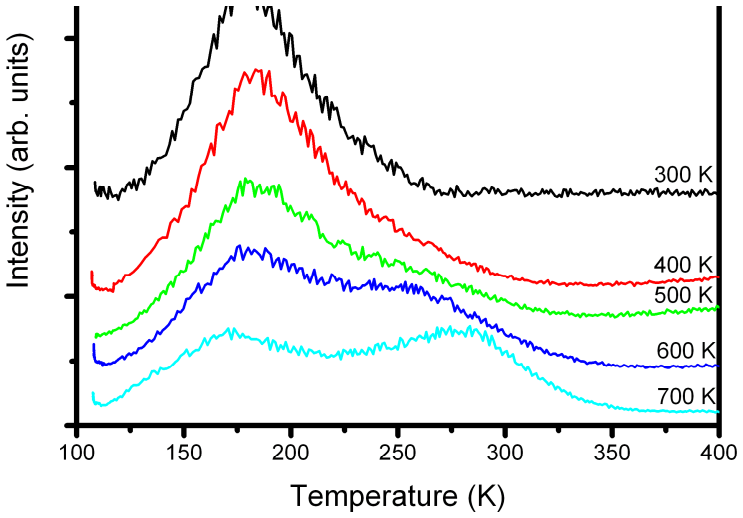

Figure 4.5: Temperature dependent TPD spectra of ^{13}CO adsorbed on ~1.0 ML of Cu/CeO_{2-x}. As prepared (black), flash annealed to 400 K (red), 500 K (green), 600 K (blue), and to 700 K (cyan). All spectra were dosed with a backing pressure of 0.6 Torr for 4 mins

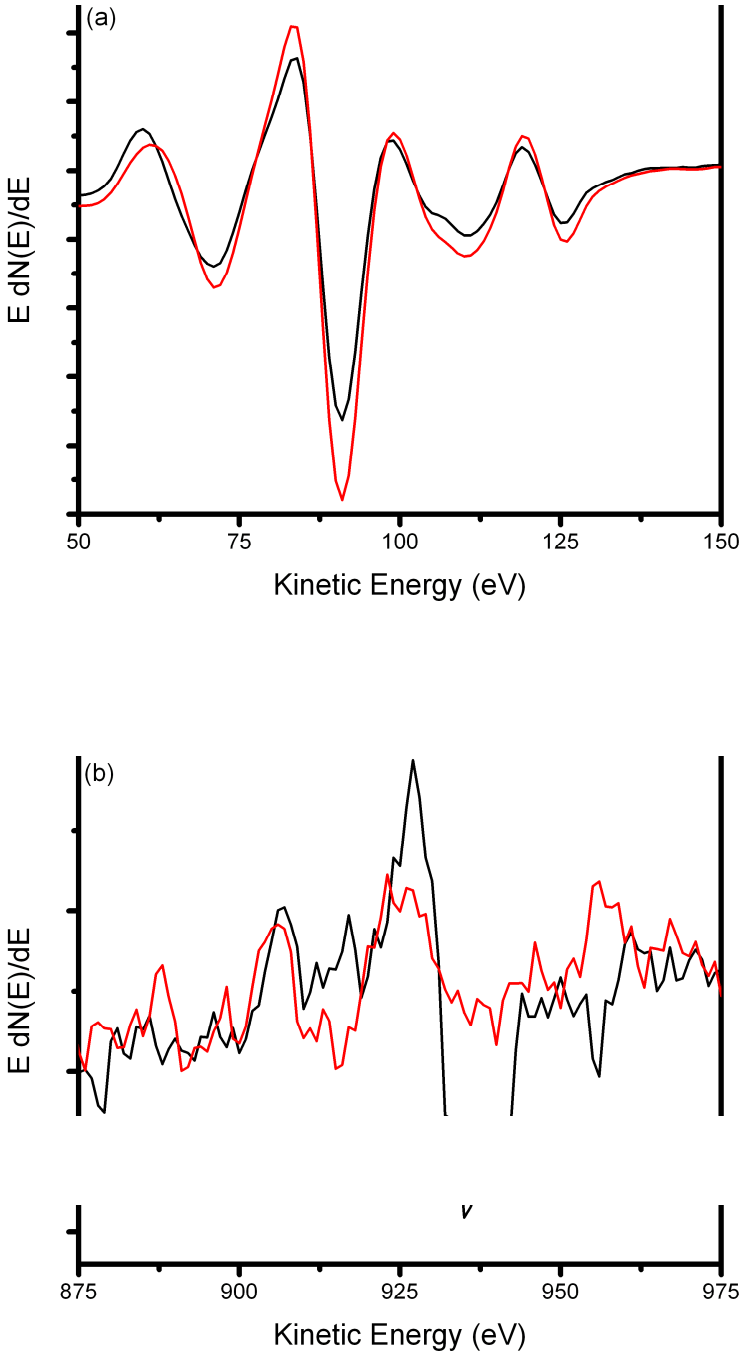

Figure 4.6: Smoothed and differentiated temperature dependent AES spectra of (a) Ce region and (b) Cu region; as prepared (black) and flash annealed to 700 K (red) for ~0.5 ML Cu/CeO_2 sample

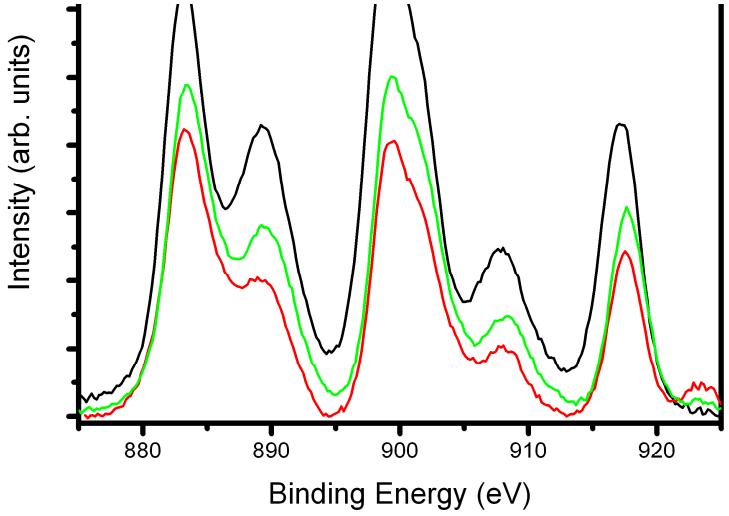

Figure 4.7: Temperature dependent Ce 3d XPS spectra. Bare surface (black), ~0.5ML Cu/CeO_2 (red), and flash annealed to 700 K (green)

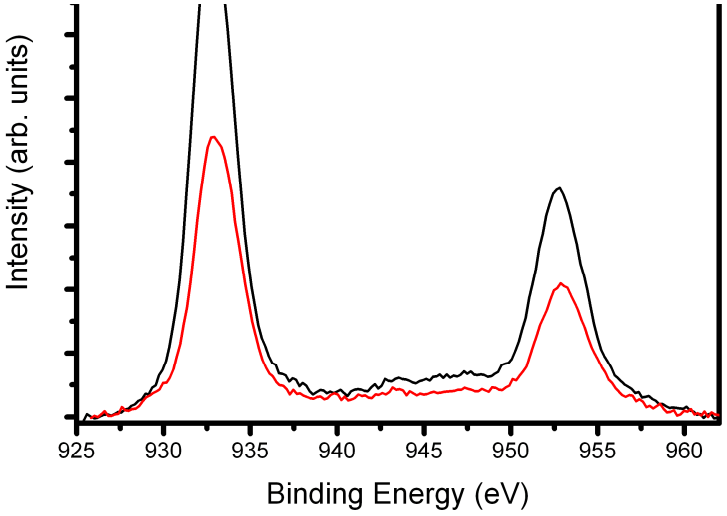

Figure 4.8: Temperature dependent Cu 2p XPS spectra. As prepared (black) and flash annealed to 700 K (red) for ~0.5 ML Cu/CeO_2

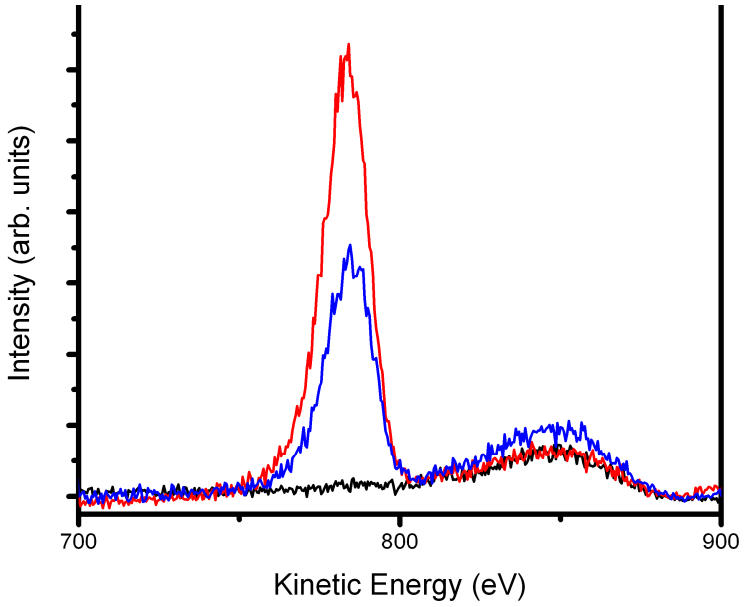

Figure 4.9: Temperature dependent ISS spectra of clean CeO_2 (black), ~0.5ML of Cu/CeO_2 (red), and flash annealed to 700 K (blue).

Chapter 5

5. An XPS Investigation of $SrTiO_3$:Rh : Role of Catalyst Preparation

This section was published in Chem. Eng. J., 223, 200-208, 2013

5.1 Introduction

The majority of current oxide semiconductor based photocatalysts are only active under UV light due to their large band gaps. Though materials like TiO_2 and $SrTiO_3$ are active for the photocatalytic decompositions of various molecules, their performance is hindered by the portion of the solar spectrum that can excite their ~3.2 eV band gaps.[56] In fact only ~4 % of the solar spectrum that hits the Earth's surface has enough energy to induce the electron hole pair formation in oxides like TiO_2 and $SrTiO_3$.[143] In order to take advantage of the majority of the solar spectrum, discovery of new materials or modifications to existing photocatalysts must be undertaken. Modifying strontium titanate ($SrTiO_3$) has garnered interest in recent years for its ability to be easily doped with various cations (Ru, Rh, Cr, Pd, Ir, Pt, etc.), which induce states into the band gap that allow for excitation via the lower energy visible light.[56, 57, 144-147]

Among the various transition metal dopants explored, Rh has stood out as one of the most promising for the production of hydrogen. A recent theoretical study found that Rh-doping of $SrTiO_3$ resulted in the best visible light driven H_2 evolution efficiency compared to five other transition metal dopants.[145] This increase in efficiency can be traced to Rh having an optimal density of states located close to the valence band maximum (VBM). This position allows for a narrowing of the band gap, while maintaining the proper conduction band minimum position for the reduction of water (Figure 5.1). These additional energy levels also reduce the number of potential electron hole recombination centers. The optimal density of states located near the

VBM and the reduced number of recombination centers were not found in the other investigated metals. Another theoretical study, which explored similar dopants, found that Rh was the only metal dopant that allowed $SrTiO_3$ to have its conduction band minimum above the potential for H_2 evolution.[147]

Bae and co-workers conducted an experimental investigation into the effect of Pd, Pt, Rh, Ir, and Ru as cation dopants in the $SrTiO_3$ lattice as visible light photocatalysts.[147] They found that the addition of Pt and Pd showed little or no visible light absorbance and no H_2 evolution. This is attributed to the fact that the dopants most likely did not diffuse into the lattice and only deposited on the surface due to the mismatch in ionic radii with Ti^{4+} cations they are expected to replace. They also found that Rh produced approximately 15 times more hydrogen than any of the other dopants. In fact, it was also determined that 1 mol % of Rh was the optimal dopant concentration due to the high crystallinity of the resulting material, enhanced visible light absorbance, and its minimized number of recombination centers. These conclusions are in good agreement with the previously published theoretical paper.[145]

As noted above, theoretical calculations suggest that incorporation of Rh into the lattice of $SrTiO_3$ produces new states in the band gap that allow for the absorption of visible light. Konta et al. were the first to propose that the absorption was due to the presence of Rh^{3+} and a higher oxidation state, either Rh^{4+} or Rh^{5+}.[57] The authors suggest that these ions would neighbor each other and would undergo reversible oxidation and reduction as the surface is exposed to light. At steady state, most of the Rh present will be trivalent (Figure 5.2). Additionally, no O_2 evolution was observed due to the inability of the dopant to create an appropriate reaction center. Despite the use of a sacrificial agent, the sample was still inactive because the Rh^{3+}/Rh^{4+} acts as an electron hole recombination site, thus not enough long lived holes are available for water

oxidation. A similar mechanism was proposed by Sasaki and co-workers for their $SrTiO_3$:Rh catalysts, produced via the solid state reaction method, that were used in conjunction with $BiVO_4$, to overcome the O_2 evolution problem.[146] Here the authors present a mechanism that requires both systems to be in intimate contact with each other and the presence of Rh^{3+} or Rh^{4+} to facilitate inter-particle electron transfer, allowing for holes to oxidize water to O_2 on the $BiVO_4$ particle and the electrons to reduce water on the $SrTiO_3$:Rh particle. Unfortunately, neither system was studied using XPS to elucidate the validity of their proposed presence of Rh^{3+}, Rh^{4+}, or Rh^{5+}. Though both proposed mechanisms are reasonable, the presence of an oxidation state other than Rh^{4+} seems unlikely due to the charge difference that would be induced in the system since Rh ions are replacing Ti^{4+} ions. Furthermore, the difference in ionic radii of Rh^{3+} and Rh^{5+} compared to Ti^{4+} would cause lattice strain that could alter the crystallinity of the particles.

A recent study of $SrTiO_3$:Rh, produced via a modified areogel method, was found to have similar H_2 evolution reactivity to the above systems.[144] The authors found a direct correlation between varying the catalyst calcination temperature and changes in surface area and crystallinity; both are known to affect the overall performance of the catalyst. Once again a proposed mechanism of an inter play between Rh^{3+} and Rh^{4+} was proposed, which they were able to confirm via XPS. However, the authors did not provide details regarding the oxidation states of Sr, Ti, or O species in the sample or a calculated stoichiometry to confirm or deny the expected substitution of Rh for Ti. Furthermore, the spectra lacked any evidence of the appropriate doublets to confirm their assignments of the Rh oxidation states.

Here an XPS investigation into the doping of $SrTiO_3$ with Rh prepared by the polymerizable complex (PC) method, solid state reaction (SSR) method, and the hydrothermal

method was conducted in conjunction with photocatalytic reactivity measurements, which will not be discussed. Each preparation produced catalysts that had Rh^{4+} ions substituting for Ti^{4+}. However, the PC method samples exhibited greater stability upon annealing. This information provided insight into the enhanced activity the PC method showed over the SSR and hydrothermal methods.

5.2 Experimental

The experiments detailed in this chapter were carried out in the UHV chamber described in section 2.1 using XPS explained in section 2.2.4. This work was part of a collaboration between Peichuan Shen and Prof. Alexander Orlov (Stony Brook Univeristy) who prepared the $SrTiO_3$:Rh samples.[148] The samples were produced via three different methods: polymerizable complex method, solid state reaction method, and the hydrothermal method. Each procedure will be briefly described to highlight their differences as amended from the procedures detailed by Shen et. al.[148]

A novel application of the PC method began by dissolving $Ti(OiPr)_4$ in a solution of methanol and ethylene glycol. While the solution was continuously stirred, citric acid was added followed by $SrCO_3$. The resultant solution was stirred at 50°C until it became transparent, at which point the $Rh(NO_3)_3$ was added. This solution was then stirred at 130°C to promote polymerization. The mixture was then heated to accelerate the evaporation of water and methanol. The polymer was then heated at 400°C for two hours to remove any excess liquid. The resultant powder was then calcined at 500°C. Samples containing 0.7, 1.0, and 5.0 mol % of Rh were produced.

The more straight forward SSR reaction is achieved by combining $SrCO_3$, TiO_2, and Rh_2O_3 powders in the desired stoichiometric ratio. The mixture was then heated at a linear rate to 500°C where it was held for 10 hours.

The hydrothermal method starts with an appropriate molar ratio mixture of amorphous TiO_2 particles, $Sr(OH)_2 \cdot xH_2O$, and $Rh(NO_3)_3 \cdot xH_2O$ dissolved in distilled water. The solution was then dried at 180°C for 12 hours. The resulting product was washed with acetic acid and deionized water. The ensuing powders were then dried overnight at 60 °C.

X-ray photoelectron spectroscopy was employed to investigate the oxidation states and chemical composition of the species present. In order to prepare the powders for use in the UHV chamber, ~40 mg of sample was pressed between two Al plates at a pressure of ~2000 psi. One of the plates (Figure 2.3) was then mounted on the holder shown in Figure 2.2. XPS spectra were obtained using unmonochromatized Al Kα (1486.6 eV) radiation. Element specific spectra were taken at an analyzer pass energy of 35 eV, with a step size of 0.2 eV, and dwell time of 0.5 sec. Each region was signal averaged for 5 scans except for Rh which was averaged over 20 scans to improve the signal to noise ratio that was a result of the low rhodium concentration in the samples. Analysis of the XPS spectra was performed using Presents software. The O 1s peak at 529.5 eV of $SrTiO_3$ was used to calibrate the energy scale to which all the measured binding energies were adjusted.[149, 150] A Shirley background was applied to the spectra which were then fit with an appropriate number of peaks. The fits were allowed to optimize without constraints as long as a reasonable FWHM (below ~3 eV) and goodness of fit were obtained. In cases where a FWHM greater than 3 eV occurred, widths and/or known peak separations were fixed to one another, until an acceptable fit was achieved. The atomic sensitivity factors of 0.63

(O 1s), 1.1 (Ti $2p_{3/2}$), 1.05 (Sr 3d), and 1.75 (Rh $3d_{5/2}$) were used to correct for differences in photoemission cross sections to obtain relative surface atomic compositions.[67]

5.3 Results and Discussion

Figure 5.3 shows the XPS spectra for (a) Sr 3d, (b) Ti 2p, and (c) O 1s spectra for as prepared $SrTiO_3$:Rh (1 mol%) synthesized by the PC method. The spectra for Sr and Ti both contain one doublet, which indicates that there is only one oxidation state of each element present. Sr is present in its 2+ oxidation state as evidenced by the peak position of the $3d_{5/2}$ peak centered at 132.3 eV. Ti is present as 4+, which is confirmed by the $2p_{3/2}$ peak positioned at 458.1 eV. The O 1s spectra showed 2 peaks, which correspond to lattice oxygen (529.5 eV) and OH species on the surface (531.8 eV). These spectra are representative of all the doped samples investigated for the PC method, as well as the 1 mol% SSR and hydrothermal methods (not shown). All peak values are in good agreement with literature values.[67, 120, 149-151]

The Rh 3d XPS spectrum of the as prepared $SrTiO_3$:Rh (1 mol%) sample produced by the PC method is shown in Figure 5.4. The spectrum was fitted with a doublet indicating only a single oxidation state. Here rhodium is present in the 4+ oxidation state as evidenced by a $3d_{5/2}$ binding energy of 309.3 eV.[151] The as prepared $SrTiO_3$:Rh (1 mol%) sample synthesized by the SSR method (Figure 5.5a), exhibited a similar Rh 3d spectrum to that of the PC method. However, the hydrothermal sample (Figure 5.5b) shows the presences of two Rh species. Rh^{4+} is the dominant species; however; there is a noticeable contribution to the overall spectrum from the presence of Rh^0.

When the samples were annealed at 850 K in vacuum for 30 min, the XPS spectra of the SSR, and hydrothermal samples became distinctly different. As shown in Figure 5.6a, the Rh 3d spectrum for the hydrothermal sample showed an increase in the amount of Rh^0 present. A

similar behavior was also seen in the sample prepared via the SSR method (Figure 5.6b). The appearance (increase) of Rh^0 suggests that some of the Rh^{4+} in the as synthesized SSR and hydrothermal samples exists as a surface oxide, which is then converted to metallic nanoparticles during high temperature annealing. In contrast, the Rh 3d spectrum for the PC sample (Figure 5.6c) was essentially unchanged after annealing, which can be seen by the retention of a single 3d doublet assigned to Rh^{4+}. These results indicate that the Rh^{4+} species in the PC samples are located mostly in the lattice, whereas the SSR and hydrothermal samples have Rh located in the lattice as Rh^{4+} and on the surface as nanoparticles, either as an oxide (before annealing) or metal particle (after annealing). Moreover, annealing the samples did not cause any significant changes in the binding energies of the Sr, Ti, or O from the literature reported values for $SrTiO_3$. The robustness of the PC sample was also confirmed by the consistency observed in the XRD patterns (not shown) for samples of varying Rh concentrations and for the 1 mol% samples calcined at different temperatures.[148]

In addition to the 1 mol% PC sample, a complete series of XPS spectra were taken for the 0.7 and 5.0 mol% samples as well. Their peak positions and assignments are detailed in Table 6.1. All binding energies for each sample were consistent with each other and are also in good agreement with the literature values for $SrTiO_3$ and Rh oxide (RhO_2).[149-151] It should be noted that in general the Rh 3d peak widths (FWHM) for the PC samples were wider (~1 eV) than those for the SSR and hydrothermal samples, however, spectra of the PC samples could only be fit by a single 3d doublet. This result is consistent with the earlier assignment that the Rh^{4+} species in the PC samples is located in the lattice.

The observation of Rh^{4+} in all the samples is consistent with the expectation that Rh^{4+} would most readily substitute for Ti^{4+} based on both charge balance and the similarity in cation

size. The relative elemental concentrations obtained from the XPS data for the PC samples, however, actually show that the Sr^{2+} abundance changes with the Rh substitution, whereas the Ti^{4+} abundance is roughly constant (Table 6.2). The calculated stoichiometries were determined using the corrected peak areas and by fixing the value of oxygen to 3. Due to the limited escape depth of the electrons sampled by XPS (~1.5 nm), it is believed that these calculated ratios are more representative of the surface and less so of the bulk material. It is well known that $SrTiO_3$ surfaces can be SrO or TiO_2 terminated or a mixture of both, depending on preparation method and post synthesis treatments.[152] This is more clearly seen in the overall stoichiometry of the Rh doped PC samples, which suggest that the 0.7 and 1.0 mol% samples are Sr rich while the 5.0 mol % is Sr deficient. These compositions are believed to be indicative of the surface and not the bulk, since such large changes in the stoichiometry should have resulted in more significant changes in the XRD patterns (not shown) which are more bulk sensitive.[148]

Shen et. al conducted photocatalytic tests of the PC, SSR, and hydrothermal 1 mol% (most active concentration), using an aqueous solution of 20 vol% methanol and a 300 W Xe lamp equipped with UV and IR filters. Their testing showed that the sample prepared by the PC method had the highest overall amount of hydrogen evolved both with and without the addition of a Pt co-catalyst. This is in good agreement with the presence and stability of the Rh^{4+} that is found predominately in the lattice of the PC samples rather than the SSR and hydrothermal samples that had Rh in the lattice and on the surface. The latter species is likely to play no role in altering the band gap of $SrTiO_3$. The presence of Rh^{4+} in the lattice is in good agreement with what has been seen and theorized previously for $SrTiO_3$:Rh photocatalysts.[57, 144-147]

5.4 Summary

This is the first XPS investigation of Rh doped $SrTiO_3$ samples produced by three different methods. The XPS results showed that Rh doping of $SrTiO_3$ using the PC method results in the substitution incorporation of Rh^{4+} cations in the lattice. Stoichiometry calculations based on the XPS areas, show that on the surface (XPS escape depth of ~1.5 nm), Rh seems to be substituting for the Sr atoms; however, this is most likely only a surface feature as there are no noticeable changes in the XRD patterns for the varying concentrations of Rh. By comparison Rh is present both in the lattice and on the surface of the samples produced via the SSR and hydrothermal methods. The presence of Rh on the surface as nanoparticles will have no effect on altering the $SrTiO_3$ band gap to enhance its ability to adsorb visible light. The uniformity of the Rh^{4+} in the lattice for the sample synthesized by the PC method is one of the key characteristics for the enhanced visible light induced photocatalytic activity. This study shows that the combination of surface science techniques (i.e. XPS) with *ex situ* reactivity measurements can be a powerful approach for understanding and improving catalyst preparation and performance.

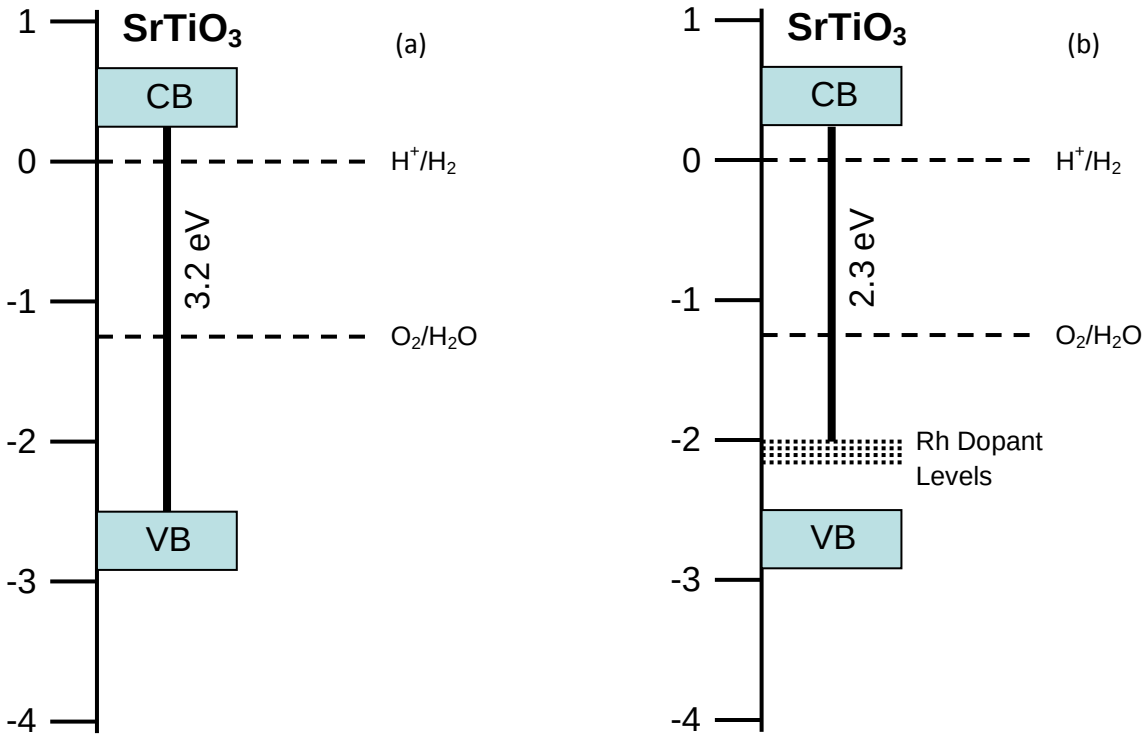

Figure 5.1: Relationship between the band structure of (a) $SrTiO_3$ and (b) $SrTiO_3$:Rh and the redox potentials for water splitting.

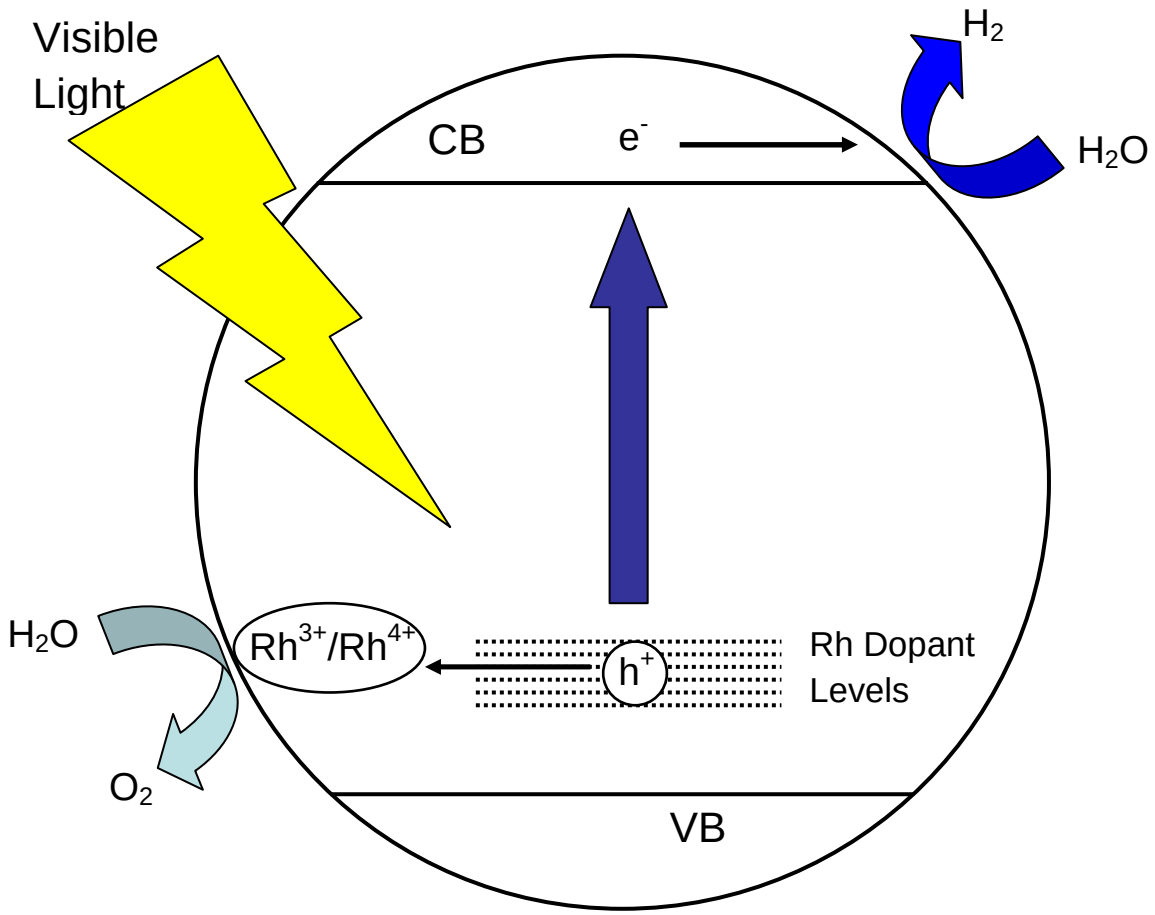

Figure 5.2: Proposed visible light response for $SrTiO_3$:Rh

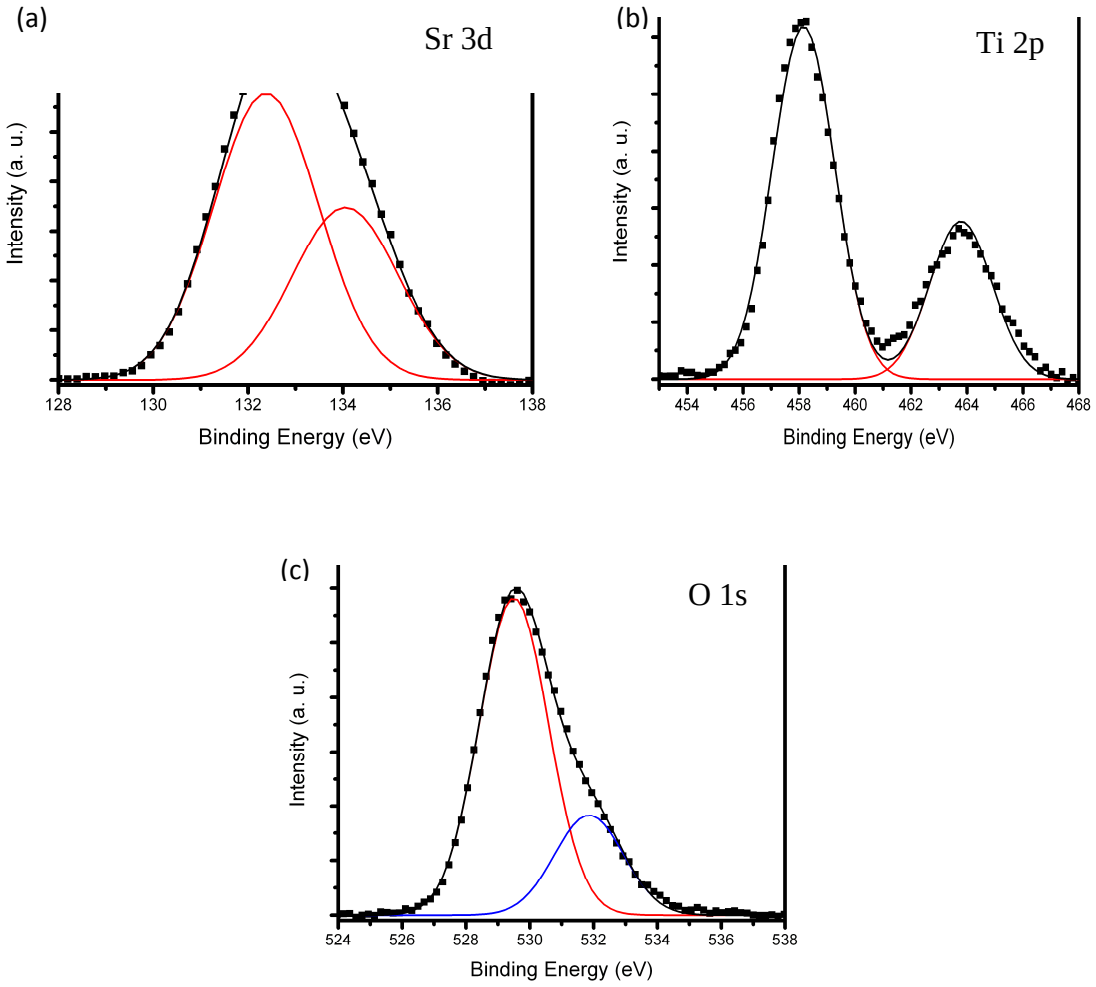

Figure 5.3: Fitted (a) Sr 3d, (b) Ti 2p, (c) O 1s XPS spectra of the as prepared $SrTiO_3$:Rh (1 mol%) produced by the PC method. Black squares are the original data, black line is the overall fit, red line is the Sr^{2+}, Ti^{4+}, and lattice oxygen fits (respectively), and blue line is -OH fit. Spectra are representative of the sample synthesized by the SSR and hydrothermal methods.

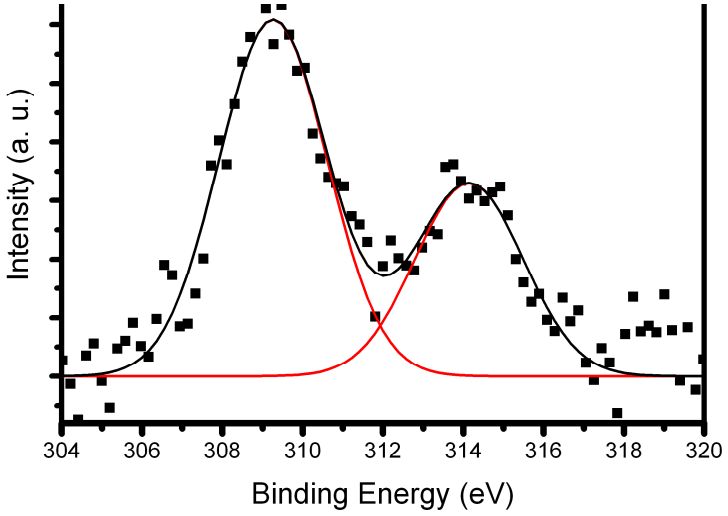

Figure 5.4: Fitted Rh 3d XPS spectrum of the as prepared $SrTiO_3$:Rh (1 mol%) produced by the PC method. Black squares are the original data, black line is the overall fit and red line is the Rh^{4+} fits.

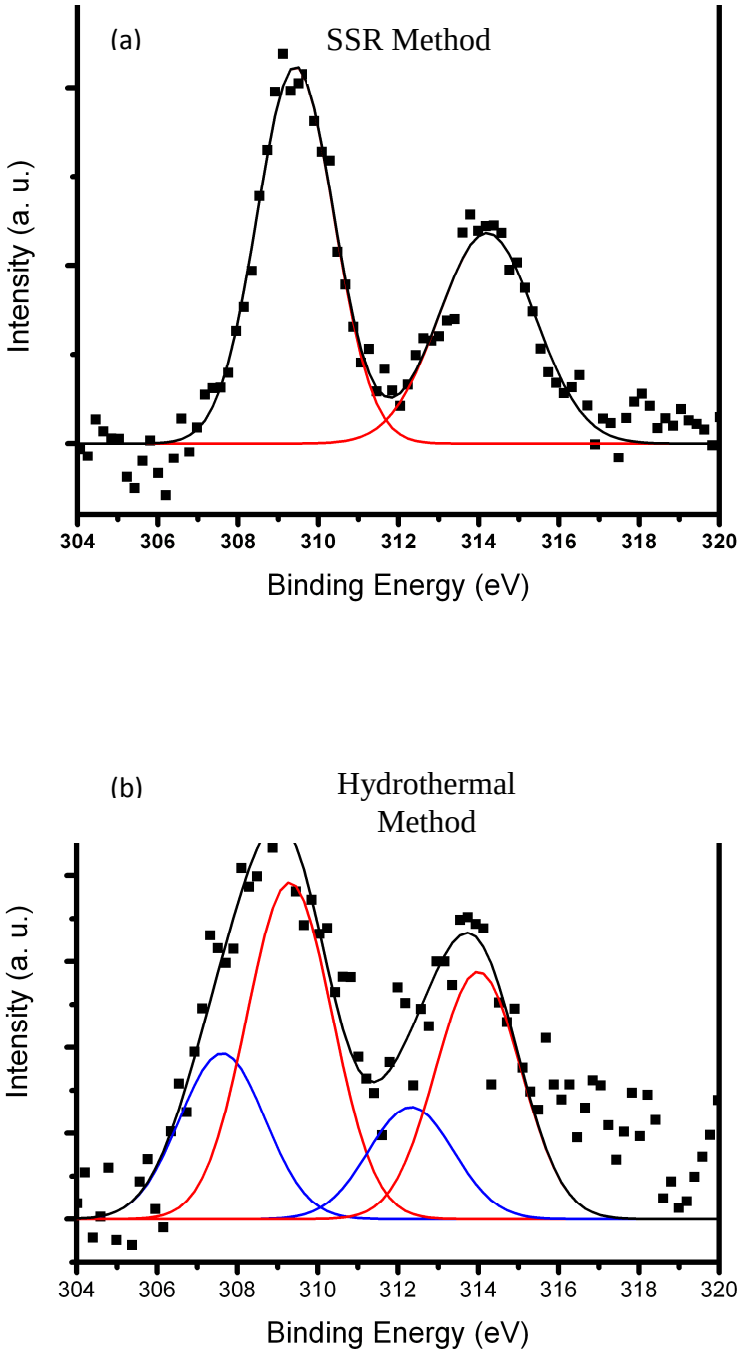

Figure 5.5: Fitted Rh 3d XPS spectra of the as prepared $SrTiO_3$:Rh (1 mol%) produced by (a) SSR method and (b) hydrothermal method. Black squares are the original data, black line is the overall fit, red line is the Rh^{4+} fits, and blue line is the Rh^0 fit

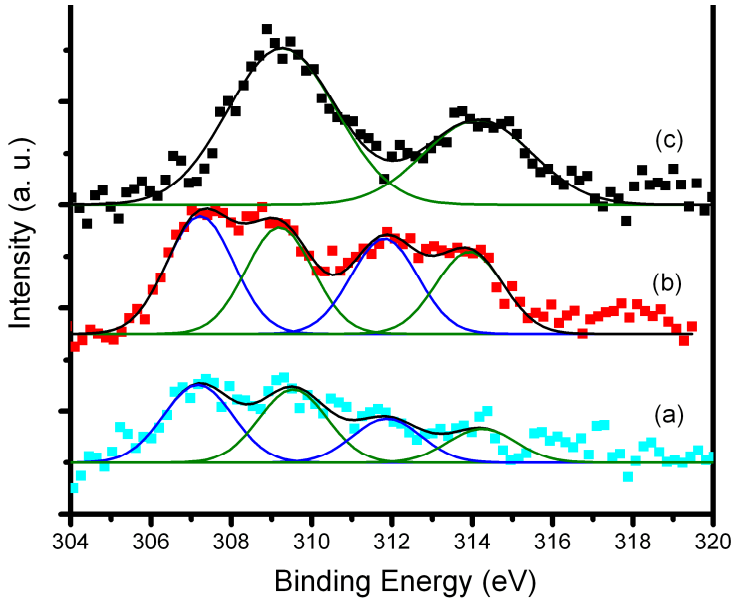

Figure 5.6: Fitted Rh 3d XPS spectra of $SrTiO_3$:Rh (1 mol%) samples prepared by (a) hydrothermal method (cyan squares), (b) SSR method (red squares), and (c) PC method (black squares) after a 30 min anneal at 850 K. The black lines are the overall fits, the green lines are the Rh^{4+} fits, and the blue lines are the Rh^0 fits.

Sample	Exp. BE (eV)	Assignment	Adjusted Area
$SrTiO_3$:Rh (0.7 mol %)			
Rh	309.0	$Rh(^{4+})O_2$	197.41 ($3d_{5/2}$)
Sr	132.5	$Sr(^{2+})TiO_3$	10493.70 (3d)
Ti	458.2	$SrTi(^{4+})O_3$	6664.72 ($2p_{3/2}$)
O1	529.5	$SrTiO_3(^{2+})$	22297.20 (1s)
O2	531.9	OH	5619.40(1s)
$SrTiO_3$:Rh (1 mol %)			
Rh	309.3	$Rh(^{4+})$O2	248.33 ($3d_{5/2}$)
Sr	132.3	$Sr(^{2+})$TiO3	12185.20 (3d)
Ti	458.1	$SrTi(^{4+})$O3	7769.77 ($2p_{3/2}$)
O1	529.5	SrTiO3 ($^{2+}$)	25074.10 (1s)
O2	531.8	OH	7875.03 (1s)
$SrTiO_3$:Rh (5 mol %)			
Rh	309.3	$Rh(^{4+})O_2$	546.99 ($3d_{5/2}$)
Sr	132.4	$Sr(^{2+})TiO_3$	5733.57 (3d)
Ti	458.0	$SrTi(^{4+})O_3$	7092.11 ($2p_{3/2}$)
O1	529.5	SrTiO3 ($^{2+}$)	22042.70 (1s)
O2	531.2	OH	2977.10 (1s)

Table 5.1: Summary of binding energies, assignments, and calculated areas of each atomic species for $SrTiO_3$: Rh (0.7, 1, 5 mol %) prepared by the PC method

%Rh[a]	Rh/O	Ti/O	Sr/O	Sr/Ti	Rh/Ti	Rh/Sr	Calculated Stoichiometry Rh : Sr : Ti : O
0.07	0.01	0.30	0.47	1.6	0.03	0.02	0.03 : 1.4 : 0.9 : 3.0
1.0	0.01	0.31	0.49	1.6	0.03	0.02	0.03 : 1.5 : 0.9 : 3.0
5.0	0.03	0.32	0.26	0.8	0.08	0.09	0.07 : 0.8 : 1.0 : 3.0

[a] Mole percent of Rh precursor

Table 5.2: Summary of compositional ratios determined using the fitted XPS peak areas corrected for elemental sensitivity factors. Calculated stoichiometries was determined using the corrected peak areas and by fixing the value of oxygen to 3.

Chapter 6

6. The Surface Composition and Water Interactions of Various Lanthanum Titanate Perovskite Photocatalysts

This work is to be published

6.1 Introduction

The WGS reaction is not the only way to produce clean hydrogen. Water can also be photocatalytically split into its base components of hydrogen and oxygen. This process has two major advantages over other hydrogen production schemes; it consumes no fossil fuels and also does not emit any form of greenhouse gas. Photocatalytic water splitting also has the advantage of using the most abundant resource on the planet; H_2O, which covers ~70% of the Earth's surface. Also, if the end products are utilized properly, this H_2 generation process can be completely renewable. Using light to create energy has been something Mother Nature has been doing since the first organism used chlorophyll to adsorb sunlight and convert carbohydrates into chemical energy. However, photochemical water splitting only requires water and light to produce useable energy. To date, oxides[39, 49, 52, 56], oxysulfides[49], and oxynitrides[53, 153-155] have shown promise for use in photocatalytic water splitting.

Over fifty years ago, Honda and Fujishima, found that a TiO_2 electrode coupled to a platinum black electrode can facilitate the photoinduced splitting of water.[48] The authors found that when the TiO_2 electrode was irradiated, current flowed to the platinum electrode from the TiO_2 electrode. This electron flow (current) indicates that water is oxidized to form oxygen and hydrogen ions at the TiO_2 surface, while the hydrogen ions are reduced to form H_2 at the platinum surface. A recent review of the surface science studies conducted on TiO_2 as a photocatalyst[39] contains over 1500 references since the initial discovery by Honda and

Fujishima.[48] This review highlights the various forms of TiO_2 (i.e. anatase and rutile) and their interactions with numerous adsorbates. More importantly, the insight gained from the molecular understating of bulk phenomenon (such as photon adsorption) and how they relate to surface events. The additions of metal co-catalysts (Pt, Au, Ag, Pd, Rh, and Cu) have also been extensively studied. Though each has it own unique features for specific reactions, they all promote charge carrier separation, with electrons accumulating on the metal and holes on the oxide.[39]

As stated above, TiO_2 based systems have been studied for over fifty years; unfortunately, due to its large band gap, ~3.1 eV, it is only an active photocatalyst under ultraviolet light. In order to utilize more of the solar spectrum, the band gap needs to be decreased so that visible light, which constitutes the bulk of the available solar spectrum, can be used to initiate electron-hole pair formation (Figure 5.1). This process is vital for photocatalysis. Cation or anion doping can create compounds that contain new states near the valence or conduction band of a semiconductor. Materials possessing a layered perovskite structure have also been shown to be promising as water splitting photocatalysts. Domen and co-workers were some of the first to show that niobates with potassium or rubidium ($Ln_xNb_6O_7$, Ln = K, Rb) to be effective water splitting catalysts.[156-158] Though these systems showed activity, the addition of nickel into the layers allowed for the stoichiometric evolution of H_2 and O_2.

Lanthanum titanates are another class of layered perovskites, which have a surface structure of (110).[159, 160] There are of particular interest in the work presented here and have been shown to photo-decompose organics[51, 161] and show high water splitting activity.[49, 58, 59, 162-164] Domen and co-workers have shown that TiO_2 powders co-doped with La and N can be effective photocatalysts under visible light for the complete decomposition of acetaldehyde to

CO_2.[161] It was found that the addition of the La limited the creation of Ti^{3+} and other lattice defects, while the N doping added additional electronic states into the band gap to allow for the adsorption of visible light. The photo-decomposition of oxalic acid, a very common industrial pollutant, has been achieved using a lanthanum and iodine doped TiO_2 powder.[51] The I^- doping exhibited similar behavior to N^{3-} doping and allowed the band gap to be shifted into the visible region. In this experiment the La did not incorporate into the lattice but formed La_2O_3 particles on the surface. These particles are believed to play a role in suppressing recombination of electron hole pairs. This is a vital characteristic to any "good" photocatalysts because charge carrier separation is what allows for efficient production of H_2 (electrons) and O_2 (holes).

Lanthanum titanate powder, $La_2Ti_2O_7$, has been studied as a photocatalyst for water splitting.[58, 59] Like most (110) layered perovskites, $La_2Ti_2O_7$ exhibits an extremely low rate of H_2 evolution. However, the addition of a NiO_x particle co-catalyst greatly enhanced the sample's ability to split water under UV irradiation. The authors found that 1 wt% NiO_x supported on $La_2Ti_2O_7$ produced H_2 at a rate nearly two orders of magnitude greater than TiO_2 and $SrTiO_3$. They attribute this enhancement to longer lived electron hole pairs that exist as a result of the natural layering of the perovskite sample and the efficient electron hole separation between the perovskite and NiO_x. The authors also found that the reduction of water takes place on the NiO_x particles and oxidation takes place on the surface of the perovskite, further emphasizing the roles the particles and the perovskite play in this process.

Oxynitrides, created from layered (110) perovskites, are another class of photocatalysts that have gained interest in recent years due to their ability to split water under visible light.[53, 154, 155, 165] In addition to catalytic activity, oxynitrides have been found to be stable in various chemical environments, including acids, and also at high temperatures in air. These unique

characteristics make them even more promising as possible photocatalysts.[155] Domen and co-workers have conducted several experiments regarding the preparation and resulting photocatalytic performance of $LaTiO_2N$. Using DFT, they found that the valence band was made of mainly N 2p orbitals, rather than O 2p orbitals of traditional oxides (i.e. TiO_2 or $SrTiO_3$).[165] This change in the composition of the valence band structure lowers the band gap from ~3.8 eV ($La_2Ti_2O_7$)[164] to ~2.2 eV allowing the use of visible light to excite electrons to the conduction band. Furthermore, the band positions are such that both half reactions are possible.[53] The addition of a co-catalyst (TiO_2 or IrO_2) was found to greatly enhance the photocatalytic activity of the oxynitrides.

To date, this is the first surface science experiment to investigate the surface atomic composition and water interactions of single crystals of $La_2Ti_2O_7$ (2-2-7), $La_5Ti_5O_{17}$ (5-5-17) and a nitrided 2-2-7 crystal, which produced a film with an overall stoichiometry of $LaTiO_2N$. AES and XPS were used to determine surface composition. The 2-2-7 and 5-5-17 crystals were found to have compositions similar to the proposed stoichometry. On the other hand, the nitrided 2-2-7 exhibited stoichometry and oxidation states that were not consistent with the expected $LaTiO_2N$. TPD was employed to investigate these systems' interaction with water. These experiments have revealed that despite the high activity of the powder catalyst equivalents, water only binds molecularly and only to slightly above room temperature. A UV diode (365 nm) was used to try and induce electron-hole pairs to facilitate the dissociation of water.

6.2 Experimental

Experiments in this chapter were conducted in the UHV chamber detailed in section 2.1 using TPD, AES, and XPS techniques detailed in section 2.2 of this dissertation. Only experimental specific details will be given here. This work was part of a collaboration with Dr.

Limin Wang, Dr. Polina Burminstrova, and Prof. Peter Khalifah (Stony Brook University) from whom the samples were received. The 2-2-7 and 5-5-17 crystals were grown using a floating zone furnace. First, La_2O_3 and TiO_2 powders were mixed in a stoichiometric ratio and calcined at 1300°C to produce 2-2-7 powder. The powder was then pressed into a rod with a diameter of ~5 mm and sintered at 1300°C for 24 hours in air. Finally, the rod was placed in the floating zone furnace where four high intensity lamps were focused into a spot size of ~4 mm, forming a melting zone with a temperature in excess of 1800°C. The 2-2-7 and 5-5-17 crystals were grown in pure oxygen and a reducing (Ar/H_2 = 98:2) atmosphere, respectively. The molten rod then crystallizes as it cools to form the native crystal. The resulting cylindrical crystals were then cleaved along the growth axis using a razor blade guillotine, which applies even force across the width of the entire blade. The cleaved crystals were then cut to fit within the sample holder (Figure 2.2). The side in contact with the Mo plate was polished using a water cooled counter rotating polishing machine equipped with 1500 grit sandpaper. This was done to ensure optimal contact between the crystal and gold foil to promote thermal conduction. It also ensured that when the Mo mounting clips were tightened, pressure was applied across the whole surface and not to a point, which could cause the crystal to break. A 2-2-7 crystal was nitrided by ammonolysis to produce a $LaTiO_2N$ film (~1 micron), here after referred to as nitrided 2-2-7. Ammonolysis was achieved by heating the 2-2-7 crystal in a tube furnace to 900°C for 120 minutes under an 80 ml/min NH_3 flow.

The samples were studied using temperature programmed desorption to investigate their interaction with water. D_2O (m/e = 20; Sigma Aldrich) was used to avoid interference from background H_2O (m/e = 18) in the vacuum chamber and was subjected to 3 freeze-thaw cycles to remove any dissolved gases. The samples were also irradiated using a UV diode (365nm,

Prizmatix), before and after dosing, attached to the chamber via a UV/Vis SMA feedthrough (Accu-Glass). The vacuum side of the feedthrough was equipped with a collimator (Accu-Glass) to focus the light to a spot size of ~12 mm diameter, which was large enough to completely cover the sample.

Auger electron spectroscopy was employed to monitor crystal cleanliness and determine surface composition. The experiments were carried out with an incident energy of 1.5 keV, which excited the La (NOO, 83 eV), Ti (LMM, 390 eV), and O (KLL, 510 eV) Auger transitions.[78] The surface concentrations of La, Ti, and O atoms were determined by comparing the Auger signal intensities corrected for their relative sensitivity factors: 1.4501 (La), 1.2155 (Ti), and 1.2571 (O) as per equation 2.2.[66] AES experiments were not conducted on the nitrided sample due to the overlap of the N (KLL, 389) and Ti (LMM, 390) transitions and the absence of other characteristic transitions over the energy range that we could investigate.

X-ray photoelectron spectroscopy was employed to investigate the oxidation states of the species present. Elemental specific spectra (La 3d, Ti 2p, O 1s, and N 1s) were taken at an analyzer pass energy of 35 eV, a step size of 0.2 eV, and a dwell time of 0.5 seconds. Each spectral region was signal averaged for 5 scans. The O 1s peak of 529.8 eV, which gave similar results when compared to adjusting the energy scale to adventitious C (285.0 eV), was used to calibrate the energy scale to which all measured binding energies were adjusted due to its better signal to noise ratio.[10] The fits were allowed to optimize without constraints as long as a reasonable FWHM (below ~3 eV) and goodness of fit were obtained. In cases where a FWHM greater than 3 eV occurred, widths and/or known peak separations were fixed to one another, until an acceptable fit was achieved. The surface concentrations of La, Ti, O, and N atoms were

determined by comparing the area of the fitted peaks corrected for their relative sensitivity factors: 6.7 (La $3d_{5/2}$), 1.1 (Ti $2p_{3/2}$), 0.63 (O 1s), and 0.38 (N 1s) as per equation 2.2.[67]

6.3 Results and Discussion

6.3.1 Surface Composition using AES and XPS

The smoothed and differentiated AES spectrum of $La_5Ti_5O_{17}$ (Figure 6.2), which was identical to that of the $La_2Ti_2O_7$ crystal, shows a surface that is lanthanum rich and oxygen deficient. After adjusting for the elemental sensitivity and normalizing to La, it was found that there is ~2.25x more La than Ti and approximately equal amounts of La and oxygen, resulting in an experimental stoichiometry of 1:0.45:1.38 (Table 6.1). This is contrary to the expected 1:1:3.5 stoichiometry. Though AES is a global representation of the surface it does not necessarily represent the bulk of the surface due to the electron escape depth of ~5 Å, which is equivalent to about 3 atomic layers for this system.[164] It is also known that the after ~2 Å, the electron signal is attenuated by 30-50%, depending on its elemental origin.[166] These factors suggest that the surface may be La rich but not necessarily the bulk. Again, AES was not carried out on the nitrided 2-2-7 sample due to the overlap of the N and Ti observable Auger electrons.

Figure 6.3 shows the XPS spectra for (a) La 3d, (b) Ti 2p, and (c) O1s of 2-2-7, which are identical to those the 5-5-17 crystal. The La 3d spectrum is made up of 2 distinct doublets, the $3d_{5/2}$, $3d_{3/2}$ and their corresponding satellites. These lower binding energy satellites have been seen previously;[167] and have the same 16.7 eV spin-orbit splitting, further proving their assignment. The peak position of the $3d_{5/2}$ at 834.1 eV is consistent with the La^{3+} oxidation state, which is expected and has been seen previously.[51] The La 3d spectrum also contains 2 additional satellites. One appears as a shoulder at 847.2 eV and the other as a defined peak at 864.9 eV and are due to the La (MNN) Auger transitions.[168]

The Ti 2p region (Fig. 6.3b) shows a single doublet with the $2p_{3/2}$ peak located at 458.6 eV, which is consistent with Ti^{4+} and which is the expected oxidation state for these compounds.[153, 169] Figure 6.3c shows the O 1s XPS spectrum and contains two features. The major component located at 529.8 eV is assigned to lattice O-atoms.[51, 153] The second, the minor component located at 531.9 eV, is consistent with adsorbed water (from the background) on the surface.[120] Unlike AES, which is more surface sensitive, the calculated stoichometry via XPS is 1:1:3.8 (Table 6.1), which is in good agreement with the expected 1:1:3.4. This difference in calculated stoichiometry is due to the ability of the electrons created during XPS to escape from ~2.5 nm rather than the ~0.5 nm for AES, thus providing a representation of the bulk compared to the surface.[166] This proves that that what is seen in the AES calculations is the result of a La rich surface termination.

The nitrided 2-2-7 sample showed similar La 3d and O 1s spectra as those seen in Figure 6.3 and thus will not be discussed further. Figure 6.4a shows the N 1s XPS spectrum, which consists of a single peak at 395.6 eV and is assigned to nitrogen bound to titanium as N^{3-}.[153] No other nitrogen species, e.g., molecular N_2, were present over the range investigated, which covered a larger energy region than that shown in Figure 5.4a. Though the La 3d and O 1s spectra were nearly identical compared to the parent 2-2-7, the Ti 2p (Figure 6.4b) was very different. Titanium is present as both Ti^{3+} and Ti^{4+} in the sample as evidenced by the asymmetry in the peaks and the position of the fitted Ti $2p_{3/2}$ peaks at 457.1 eV and 458.8 eV, respectively.[153] This is not unexpected since the ammonolysis results in an O^{2-} species being replaced by N^{3-}, and this change in charge is mostly likely balanced by a Ti reduction from 4+ to 3+. Here a Ti^{3+}/Ti^{4+} ratio of ~3.8 was calculated using the area of their respective XPS peaks. However, this ratio does not agree with what had been seen previously.[153] Masuda and co-

worker found that their nitrided 2-2-7 system is comprised of either equal amounts of Ti^{4+} and Ti^{3+} or an excess of Ti^{4+} with increasing nitrogen content as seen by XPS. They attributed this to a difference in anion electronegativity, resulting in a more ionic bond between Ti and O than Ti and N. Thus O-atoms pull more electrons from the Ti than N-atoms and this effect is greater than the difference in the anion's oxidation state, i.e., O^{2-} and N^{3-}. It should be noted that their lowest O/N ratio is ~7 which is ~2 times greater than our calculated ratio of ~3.4. This difference in O to N content could make the anion's oxidation state a more important factor than its electronegativity, resulting in more Ti^{3+} than Ti^{4+}.

It has already been shown that the sample is O rich due to the O/N ratio, however, a calculated stoichiometry of 1:0.94:2.09:1 (Table 6.1) is obtained and it is apparent that the other components are close to the projected $LaTiO_2N$ stoichiometry. A previous study has shown that annealing TiN in an O_2 atmosphere at temperatures in excess of 550 K will result in a change from TiN to TiON to TiO_2.[170] Efforts were taken to replicate these results and produce an O/N ratio similar to those seen previously, ~7,[153] by annealing the sample at 800 K in a background of 2×10^{-6} Torr O_2. The reported change from TiON to TiO_2 should shift the Ti^{3+}/Ti^{4+} closer to 1. However, as can be seen in Figure 6.5 only a minor initial increase was seen in the O/N ratio and it never approached the previously reported values of >6; this treatment also resulted in a Ti^{3+}/Ti^{4+} ratio (~3) that was constant over the time investigated. This resiliency to undergo change may be due to the relatively low pressure of O_2, when compared to atmosphere, but more importantly could be an indication of the robustness of the surface, a desirable characteristic of a commercial catalyst.

6.3.2 D_2O TPD from $La_2Ti_2O_7$, $La_5Ti_5O_{17}$, and Nitrided $La_2Ti_2O_7$

Figure 6.6 shows the TPD spectra of D_2O coverage dependence on (a) $La_2Ti_2O_7$, (b) $La_5Ti_5O_{17}$, and (c) nitrided $La_2Ti_2O_7$. The 2-2-7 and 5-5-17 single crystals have very similar TPD profiles, with a single feature appearing at 315 K and 260 K, respectively, for the lowest D_2O dose. As water coverage increases, these features increase in intensity and shift to lower temperature, 250 K and 230 K, which is indicative of the repulsive interactions between water molecules. Even though these features shift to lower temperature they still extend to ~325 K. These higher temperature features are assigned to desorption of chemisorbed water. Before these higher temperature features saturates, a new feature appears at 200 K for both surfaces. The peaks for a saturated dose for both the 2-2-7 and 5-5-17 are similar to those seen on the fully oxidized surfaces of TiO_2 (110)[70, 79] and TiO_2 terminated $SrTiO_3$ (100)[171] surfaces, where the low temperature peak can be attributed to a second layer of water that is hydrogen bonded to the chemisorbed layer or a simple physisorbed layer. The most important aspect of the TPD profiles is that there is no observed peak above 350 K, which is characteristic of dissociated water. This thermally induced dissociation is attributed to water interacting with oxygen vacancies and is seen at ~500 K on reduced TiO_2 (110)[71] and at ~700 K on CeO_2.[104]

Figure 6.6c shows the D_2O coverage dependence TPD for nitrided 2-2-7. It is similar to those seen for its parent crystal (2-2-7) and the 5-5-17, both described above. However, there are 3 different aspects to the adsorption/desorption of water from its surface. First, even at the lowest coverage in which a measurable signal was obtained, there is the presence of 2 features, rather than one. The high temperature peak starts at an even lower temperature of 240 K and shifts to 205 K at saturation. This peak is 25 – 45 K lower than that for the single crystal surfaces; however; it is still assigned to molecularly chemisorbed state. This is due to the fact

that the peak saturates and exhibits a shift to lower temperature as seen on the 2-2-7 and 5-5-17 single crystals. Furthermore, this peaks desorption temperature occurs at a similar temperature to chemisorbed peaks for TiO_2[70, 79] and $SrTiO_3$.[171] The low temperature peak, which is always present and is less intense than the high temperature peak, initially appears at a temperature of 180 K and shifts to 155 K. This peak also saturates at the same dose as the high temperature peak and is assigned to a second layer of hydrogen bonded water. The lack of an apparent physisorbed layer may be a result of the dosing temperature, 107 K, being higher than the desorption temperature of physisorbed water on this surface.

Though the desorption temperatures for each of these lanthanum titanate samples are different, they are all in within the same general temperature range and thus originate from water bound to the surface in similar manner. The higher temperature is likely due to water directly bound to either the La or Ti atoms on the surface or just below the bridging oxygen. The lower temperature peak than likely results from a second "ice" layer hydrogen bonded to this chemisorbed layer.[79]

Attempts to create O-vacancies by high temperature annealing and light sputtering, known to induce vacancies[71], proved to be unsuccessful. It is know that O vacancies have the ability to decompose water to form OH groups,[70, 79, 120] which may have been a precursor to complete water splitting. The resultant TPD profiles (not shown) did not show a presence of a peak at temperatures greater than 350 K and looked nearly identical to the native samples, with only a minor loss in signal to the chemisorbed peak on the sputtered surfaces. That loss in signal is most likely due to an altering of the surface composition and morphology due to the differences in weight of Ti and La, since lighter elements are preferentially sputtered.

The appearance of a recombination peak in the TPD spectra for the 2-2-7, 5-5-17, and nitrided 2-2-7 samples were also studied via exposure to UV irradiation (365 nm) both before and after D_2O dosing. UV exposure times up to 10 minutes resulted in no change to the subsequent TPD spectra. This method has been useful in determining the products of photoinduced reactions.[79, 172] The lack of a recombination peak does not mean these systems are ineffective as a water splitting catalyst, just that our conditions, i.e. diode power, water exposure, and catalyst surface area, are not optimal for studying water splitting over these systems.[79]

6.4 Summary

The interaction of water (D_2O) with $La_2Ti_2O_7$, $La_5Ti_5O_{17}$, and nitrided $La_2Ti_2O_7$ was investigated. All three samples were found to physisorb and chemisorb molecular water, the latter of which remained on the surface in excess of 300 K. Attempts to induce oxygen vacancies to facilitate water dissociation proved to be ineffective. As a result, it is unlikely that thermally dissociated water plays a role in the water splitting reaction seen previously on these perovskite surfaces. Photo induced dissociation of water was also investigated under UHV conditions with the use of a UV diode. Post UV TPDs revealed no change in the interaction of water with these surfaces. However, lack of a change does not mean these systems are ineffective as a water splitting catalyst, just that our conditions, i.e. diode power, water exposure, and catalyst surface area, are not optimal for water splitting to occur.

Additionally AES and XPS analysis was conducted on the surface. AES showed that the 2-2-7 and 5-5-17 crystal surface are La rich, compared to the bulk, which XPS proved to have a composition similar to the expected stoichiometry. The structure of the nitrided 2-2-7 sample proved to be oxygen rich, throughout the depths probed by XPS. Despite the excess oxygen, the Ti 2p spectrum showed a system that was highly reduced. The presence of nitrogen seems to

produce a sample made up of layers of La_2O_3, TiO_2, and TiN, rather than layers of La_2O_3 and $TiO_{2-x}N_x$. Efforts to further alter the sample's stoichiometry, via high temperature oxygen annealing, resulted in no changes to the electronic structure of the sample or its interaction with water. This is further evidence that ammonolysis produces a robust TiN layer that is resistant to oxidation. Currently, depth profiling experiments are being conducted on the nitrided 2-2-7 sample. This achieved by sputtering the surface with Ar^+ ions, with XPS taken after each treatment. Initial results are indicating that the sample is consistent through out.

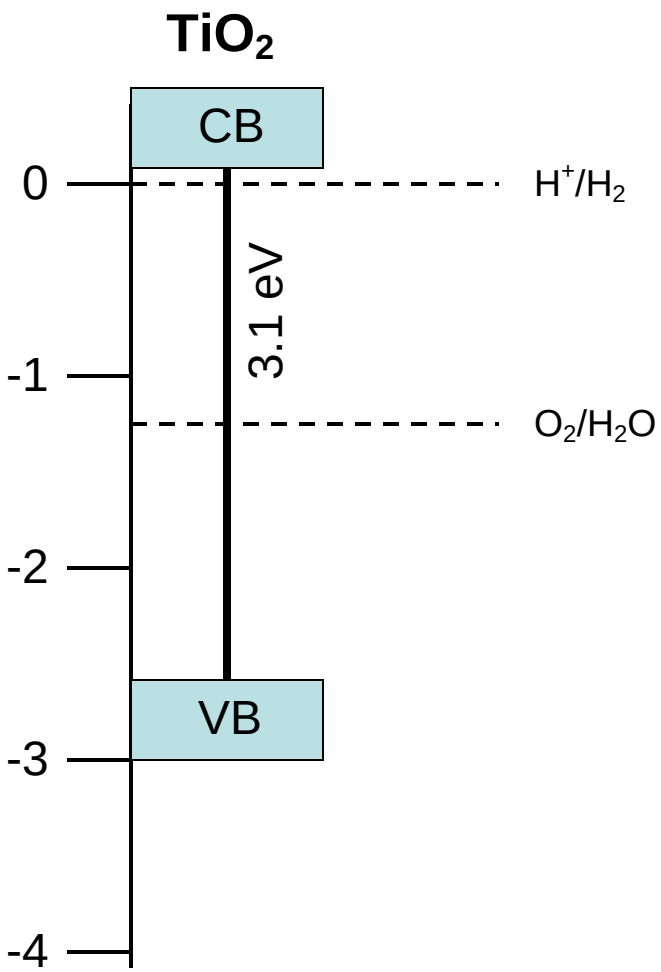

Figure 6.1: Relationship between the band structure of TiO_2 and the redox potentials for water splitting.

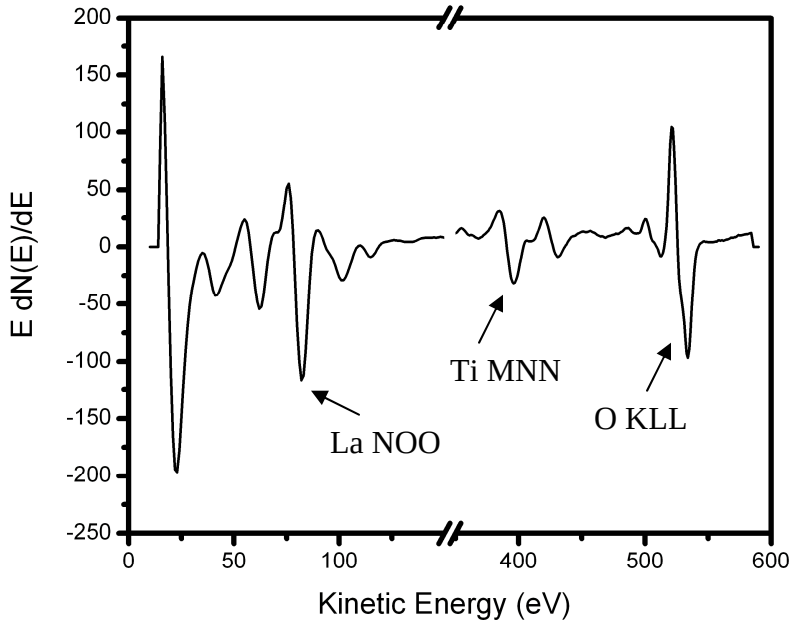

Figure 6.2: Smoothed and differentiated AES spectrum of $La_5Ti_5O_{17}$. Peaks of interest are located at 83 eV (La, NOO), 390 (Ti, MNN), and 510 (O, KLL).

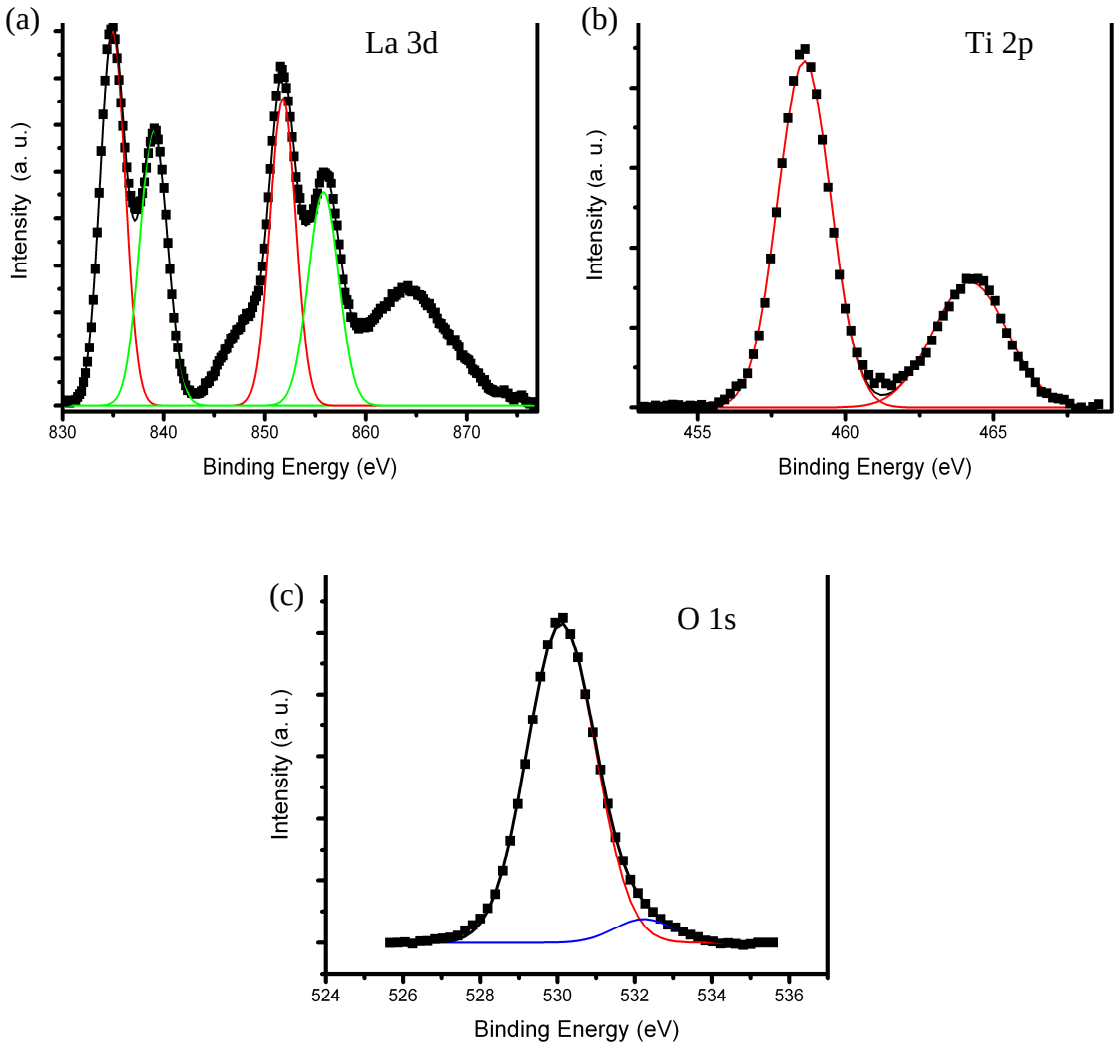

Figure 6.3: XPS spectra of (a) La 3d: red line is La^{3+} fit, the green line is satellite fit, and the peaks that are not fitted are due to La (MNN) Auger lines, (b) Ti 2p: red line is Ti^{4+} fit. (c) O 1s: red line is lattice oxygen and blue is OH fit for $La_2Ti_2O_7$. In all spectra squares are raw data and the black line represents the overall fit.

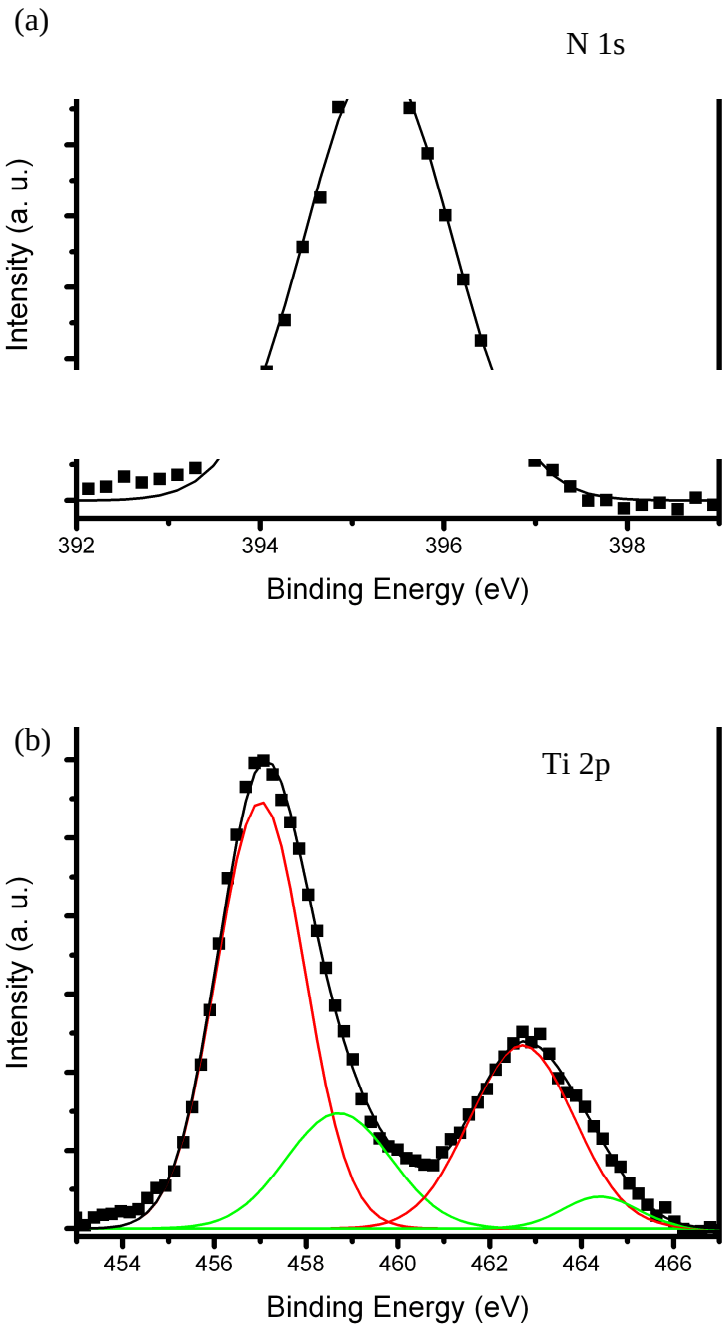

Figure 6.4: XPS spectra of (a) N 1s and (b) Ti 2p: red line is Ti^{3+} fit and green line is Ti^{4+} fit. In all spectra the squares are raw data and the black line represents the overall fit.

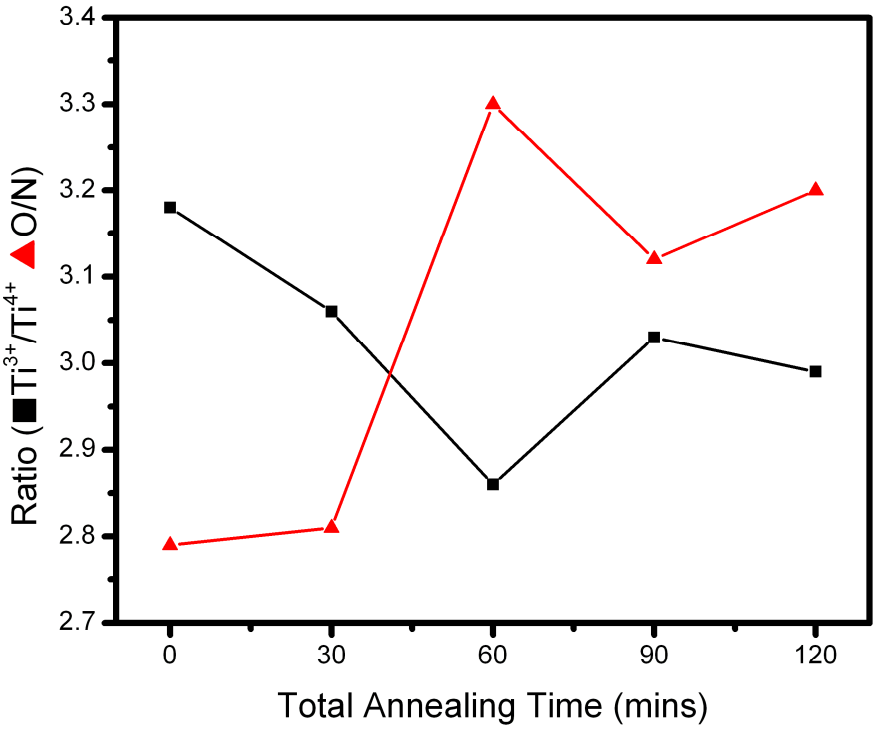

Figure 6.5: Effect of annealing in a background of O_2 (2.0 x 10^{-6} Torr) on the O/N and Ti^{3+}/Ti^{4+} ratios. Black squares are the Ti^{3+}/Ti^{4+} ratio and the red triangles are the

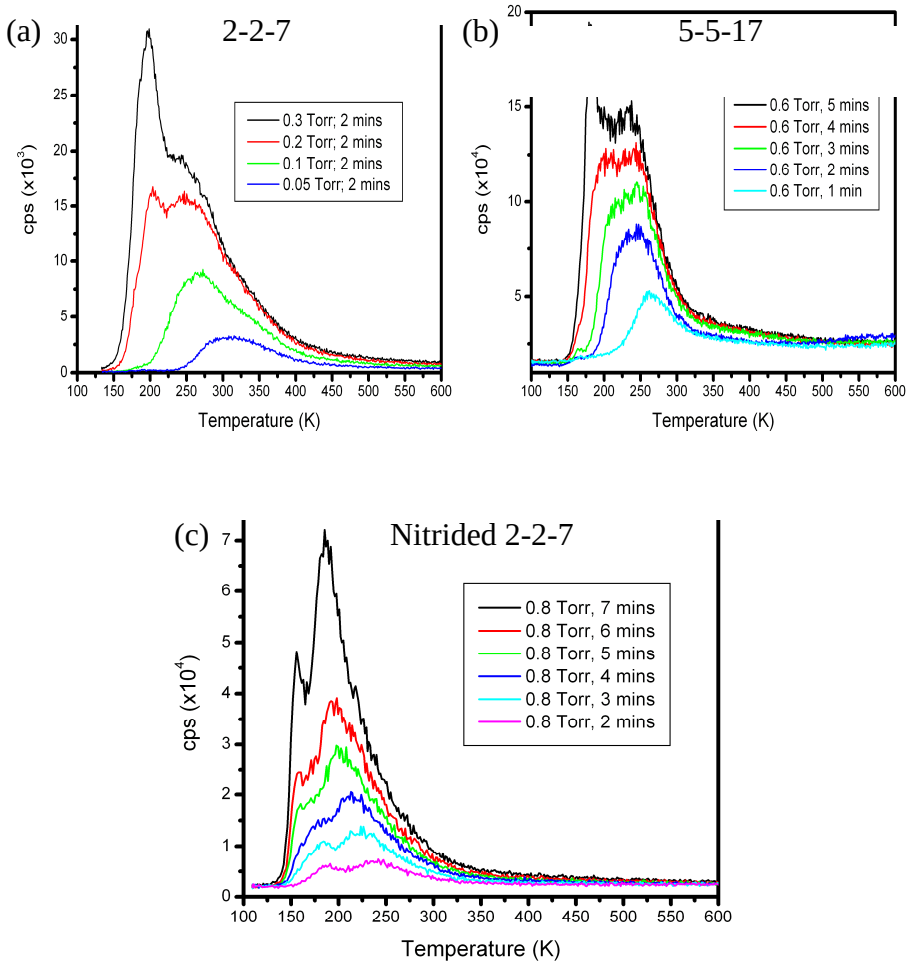

Figure 6.6: TPD spectra of D_2O coverage dependence adsorbed on (a) $La_2Ti_2O_7$, (b) $La_5Ti_5O_{17}$, and (c) nitrided $La_2Ti_2O_7$. Doses and intensities cannot be compared from sample to sample because the doser is not calibrated and spectra were taken under different QMS settings.

Sample	Expected Stoichiometry	Calculated Stoichiometry via AES	Calculated Stoichiometry via XPS
2-2-7	$LaTiO_{3.5}$	$LaTi_{0.45}O_{1.38}$	$LaTiO_{3.8}$
5-5-17	$LaTiO_{3.4}$	$LaTi_{0.45}O_{1.38}$	$LaTiO_{3.8}$
Nitrided 2-2-7	$LaTiO_2N$	N/A	$LaTi_{0.94}O_{2.09}N_1$

Table 6.1: Summary of the stoichiometry of the various lanthanum titanates. Calculated stoichiometries were determined using the corrected peak areas and by fixing the value of lanthanum to 1.

References

1. BP BP Statistical Review of World Energy: June 2012. http://www.bp.com/assets/bp_internet/globalbp/globalbp_uk_english/reports_and_publications/statistical_energy_review_2011/STAGING/local_assets/pdf/statistical_review_of_world_energy_full_report_2012.pdf.
2. Programme, U. N. D. *World Energy Assessment 2000*; September 2000, 2000.
3. Enderdata *Global Energy Statistica; Yearbook 2012*; 2012.
4. Kamat, P. V., Meeting the Clean Energy Demand: Nanostructure Architectures for Solar Energy Conversion. *The Journal of Physical Chemistry C* **2007,** *111* (7), 2834-2860.
5. Dresselhaus, M. S.; Thomas, I. L., Alternative energy technologies. *Nature* **2001,** *414* (6861), 332-337.
6. O'Connor, R. P.; Klein, E. J.; Schmidt, L. D., High yields of synthesis gas by millisecond partial oxidation of higher hydrocarbons. *Catal Lett* **2000,** *70* (3-4), 99-107.
7. Hwang, J. J., Review on development and demonstration of hydrogen fuel cell scooters. *Renew Sust Energ Rev* **2012,** *16* (6), 3803-3815.
8. Huber, G. W.; Iborra, S.; Corma, A., Synthesis of Transportation Fuels from Biomass: Chemistry, Catalysts, and Engineering. *Chemical Reviews* **2006,** *106* (9), 4044-4098.
9. Machanick, P. http://opinion-nation.blogspot.com/2009/01/forget-climate-change-fossil-fuel.html.
10. EPA, U. Climate Change Basics. http://www.epa.gov/climatechange/basics/ (accessed 09/19/12).
11. Administration, U. S. E. I. *Annual Energy Review 2011*; 2012.
12. Yang, Z. X.; Wang, Q. G.; Wei, S. Y., The synergistic effects of the Cu-CeO2(111) catalysts on the adsorption and dissociation of water molecules. *Phys Chem Chem Phys* **2011,** *13* (20), 9363-9373.
13. Chen, C. S.; Lai, T. W.; Chen, C. C., Effect of active sites for a water-gas shift reaction on Cu nanoparticles. *J Catal* **2010,** *273* (1), 18-28.
14. Rodriguez, J. A.; Liu, P.; Wang, X.; Wen, W.; Hanson, J.; Hrbek, J.; Perez, M.; Evans, J., Water-gas shift activity of Cu surfaces and Cu nanoparticles supported on metal oxides. *Catal Today* **2009,** *143* (1-2), 45-50.
15. Han, W. Q.; Wen, W.; Hanson, J. C.; Teng, X. W.; Marinkovic, N.; Rodriguez, J. A., One-Dimensional Ceria as Catalyst for the Low-Temperature Water-Gas Shift Reaction. *J Phys Chem C* **2009,** *113* (52), 21949-21955.
16. Pradhan, S.; Reddy, A. S.; Devi, R. N.; Chilukuri, S., Copper-based catalysts for water gas shift reaction: Influence of support on their catalytic activity. *Catal Today* **2009,** *141* (1-2), 72-76.
17. Laniecki, M.; Malecka-Grycz, M.; Domka, F., Water-gas shift reaction over sulfided molybdenum catalysts I. Alumina, titania and zirconia-supported catalysts. *Appl Catal a-Gen* **2000,** *196* (2), 293-303.
18. Wang, X.; Rodriguez, J. A.; Hanson, J. C.; Perez, M.; Evans, J., In situ time-resolved characterization of Au-CeO2 and AuOx-CeO2 catalysts during the water-gas shift reaction: Presence of Au and O vacancies in the active phase. *J Chem Phys* **2005,** *123* (22).

19. Sato, Y.; Terada, K.; Soma, Y.; Miyao, T.; Naito, S., Marked addition effect of Re upon the water gas shift reaction over TiO2 supported Pt, Pd and Ir catalysts. *Catal Commun* **2006,** *7* (2), 91-95.
20. Park, J. B.; Graciani, J.; Evans, J.; Stacchiola, D.; Senanayake, S. D.; Barrio, L.; Liu, P.; Sanz, J. F.; Hrbek, J.; Rodriguez, J. A., Gold, Copper, and Platinum Nanoparticles Dispersed on CeOx/TiO2(110) Surfaces: High Water-Gas Shift Activity and the Nature of the Mixed-Metal Oxide at the Nanometer Level. *J Am Chem Soc* **2010,** *132* (1), 356-363.
21. Rodriguez, J. A.; Liu, P.; Hrbek, J.; Evans, J.; Perez, M., Water gas shift reaction on Cu and Au nanoparticles supported on CeO2(111) and ZnO(000(1)over-bar): Intrinsic activity and importance of support interactions. *Angew Chem Int Edit* **2007,** *46* (8), 1329-1332.
22. Kusar, H.; Hocevar, S.; Levec, J., Kinetics of the water-gas shift reaction over nanostructured copper-ceria catalysts. *Appl Catal B-Environ* **2006,** *63* (3-4), 194-200.
23. Panagiotopoulou, P.; Kondarides, D. I., Effect of the nature of the support on the catalytic performance of noble metal catalysts for the water-gas shift reaction. *Catal Today* **2006,** *112* (1-4), 49-52.
24. Tabakova, T.; Boccuzzi, F.; Manzoli, M.; Sobczak, J. W.; Idakiev, V.; Andreeva, D., A comparative study of nanosized IB/ceria catalysts for low-temperature water-gas shift reaction. *Appl Catal a-Gen* **2006,** *298*, 127-143.
25. Boccuzzi, F.; Chiorino, A.; Manzoli, M.; Andreeva, D.; Tabakova, T., FTIR study of the low-temperature water-gas shift reaction on Au/Fe2O3 and Au/TiO2 catalysts. *J Catal* **1999,** *188* (1), 176-185.
26. Iida, H.; Igarashi, A., Difference in the reaction behavior between Pt-Re/TiO2 (Rutile) and Pt-Re/ZrO2 catalysts for low-temperature water gas shift reactions. *Appl Catal a-Gen* **2006,** *303* (1), 48-55.
27. Rodriguez, J. A.; Evans, J.; Graciani, J.; Park, J. B.; Liu, P.; Hrbek, J.; Sanz, J. F., High Water-Gas Shift Activity in TiO2(110) Supported Cu and Au Nanoparticles: Role of the Oxide and Metal Particle Size. *J Phys Chem C* **2009,** *113* (17), 7364-7370.
28. Sakurai, H.; Ueda, A.; Kobayashi, T.; Haruta, M., Low-temperature water-gas shift reaction over gold deposited on TiO2. *Chem Commun* **1997,** (3), 271-272.
29. Torquemada, M. C.; Desegovia, J. L.; Roman, E., Reactivity of Co on a Tio2(110) Defective Surface Studied by Electron-Stimulated Desorption. *Surf Sci* **1995,** *337* (1-2), 31-39.
30. Zhang, Z.; Ge, Q.; Li, S. C.; Kay, B. D.; White, J. M.; Dohnalek, Z., Imaging intrinsic diffusion of bridge-bonded oxygen vacancies on TiO2(110). *Phys Rev Lett* **2007,** *99* (12).
31. Rodriguez, J. A.; Hrbek, J., Inverse oxide/metal catalysts: A versatile approach for activity tests and mechanistic studies. *Surf Sci* **2010,** *604* (3-4), 241-244.
32. Boisen, A.; Janssens, T. V. W.; Schumacher, N.; Chorkendorff, I.; Dahl, S., Support effects and catalytic trends for water gas shift activity of transition metals. *J Mol Catal a-Chem* **2010,** *315* (2), 163-170.
33. Wang, X. Q.; Rodriguez, J. A.; Hanson, J. C.; Gamarra, D.; Martinez-Arias, A.; Fernandez-Garcia, M., In situ studies of the active sites for the water gas shift reaction over Cu-CeO2 catalysts: Complex interaction between metallic copper and oxygen vacancies of ceria. *J Phys Chem B* **2006,** *110* (1), 428-434.
34. Senanayake, S. D.; Stacchiola, D.; Evans, J.; Estrella, M.; Barrio, L.; Perez, M.; Hrbek, J.; Rodriguez, J. A., Probing the reaction intermediates for the water-gas shift over inverse CeOx/Au(111) catalysts. *J Catal* **2010,** *271* (2), 392-400.

35. Shekhar, M.; Wang, J.; Lee, W.-S.; Williams, W. D.; Kim, S. M.; Stach, E. A.; Miller, J. T.; Delgass, W. N.; Ribeiro, F. H., Size and Support Effects for the Water–Gas Shift Catalysis over Gold Nanoparticles Supported on Model Al2O3 and TiO2. *J Am Chem Soc* **2012,** *134* (10), 4700-4708.
36. Coloma, F.; Marquez, F.; Rochester, C. H.; Anderson, J. A., Determination of the nature and reactivity of copper sites in Cu-TiO2 catalysts. *Phys Chem Chem Phys* **2000,** *2* (22), 5320-5327.
37. Boccuzzi, F.; Chiorino, A.; Manzoli, M.; Lu, P.; Akita, T.; Ichikawa, S.; Haruta, M., Au/TiO2 nanosized samples: A catalytic, TEM, and FTIR study of the effect of calcination temperature on the CO oxidation. *J Catal* **2001,** *202* (2), 256-267.
38. Haruta, M., Size- and support-dependency in the catalysis of gold. *Catal Today* **1997,** *36* (1), 153-166.
39. Henderson, M. A., A surface science perspective on TiO2 photocatalysis. *Surf Sci Rep* **2011,** *66* (6-7), 185-297.
40. Jacobs, J. F.; van de Poel, I.; Osseweijer, P., Sunscreens with Titanium Dioxide (TiO(2)) Nano-Particles: A Societal Experiment. *Nanoethics* **2010,** *4* (2), 103-113.
41. Bozzi, A.; Yuranova, T.; Kiwi, J., Self-cleaning of wool-polyamide and polyester textiles by TiO2-rutile modification under daylight irradiation at ambient temperature. *J Photoch Photobio A* **2005,** *172* (1), 27-34.
42. Linsebigler, A.; Lu, G. Q.; Yates, J. T., Co Chemisorption on Tio2(110) - Oxygen Vacancy Site Influence on Co Adsorption. *J Chem Phys* **1995,** *103* (21), 9438-9443.
43. Lee, S.; Fan, C. Y.; Wu, T. P.; Anderson, S. L., Cluster size effects on CO oxidation activity, adsorbate affinity, and temporal behavior of model Au-n/TiO2 catalysts. *J Chem Phys* **2005,** *123* (12).
44. Chen, C. S.; You, J. H.; Lin, J. H.; Chen, Y. Y., Effect of highly dispersed active sites of Cu/TiO2 catalyst on CO oxidation. *Catal Commun* **2008,** *9* (14), 2381-2385.
45. Zhao, X. Y.; Hrbek, J.; Rodriguez, J. A.; Perez, M., Reaction of SO2 with Cu/TiO2 (110): Effects of size and metal-oxide interactions in the chemical activation of Cu nanoparticles. *Surf Sci* **2006,** *600* (1), 229-239.
46. Boccuzzi, F.; Chiorino, A., FTIR study of carbon monoxide oxidation and scrambling at room temperature over copper supported on ZnO and TiO2 .1. *J Phys Chem-Us* **1996,** *100* (9), 3617-3624.
47. Alexandrou, M.; Nix, R. M., The Growth, Structure and Stability of Ceria Overlayers on Pd(111). *Surf Sci* **1994,** *321* (1-2), 47-57.
48. Fujishima, A.; Honda, K., Electrochemical Photolysis of Water at a Semiconductor Electrode. *Nature* **1972,** *238* (5358), 37-+.
49. Kudo, A.; Miseki, Y., Heterogeneous photocatalyst materials for water splitting. *Chem Soc Rev* **2009,** *38* (1), 253-278.
50. Maeda, K.; Teramura, K.; Lu, D. L.; Takata, T.; Saito, N.; Inoue, Y.; Domen, K., Photocatalyst releasing hydrogen from water - Enhancing catalytic performance holds promise for hydrogen production by water splitting in sunlight. *Nature* **2006,** *440* (7082), 295-295.
51. He, Z. Q.; Xu, X.; Song, S.; Xie, L.; Tu, J. J.; Chen, J. M.; Yan, B., A Visible Light-Driven Titanium Dioxide Photocatalyst Codoped with Lanthanum and Iodine: An Application in the Degradation of Oxalic Acid. *J Phys Chem C* **2008,** *112* (42), 16431-16437.
52. Yao, W.; Iwai, H.; Ye, J., Effects of molybdenum substitution on the photocatalytic behavior of BiVO4. *Dalton T* **2008,** (11), 1426-1430.

53. Le Paven-Thivet, C.; Ishikawa, A.; Ziani, A.; Le Gendre, L.; Yoshida, M.; Kubota, J.; Tessier, F.; Doment, K., Photoelectrochemical Properties of Crystalline Perovskite Lanthanum Titanium Oxynitride Films under Visible Light. *J Phys Chem C* **2009,** *113* (15), 6156-6162.
54. Hisatomi, T.; Hasegawa, K.; Teramura, K.; Takata, T.; Hara, M.; Domen, K., Zinc and titanium spinel oxynitride (ZnxTiOyNz) as a d(0)-d(10) complex photocatalyst with visible light activity. *Chem Lett* **2007,** *36* (4), 558-559.
55. Suzuki, T.; Hisatomi, T.; Teramura, K.; Shimodaira, Y.; Kobayashi, H.; Domen, K., A titanium-based oxysulfide photocatalyst: La5Ti2MS5O7 (M = Ag, Cu) for water reduction and oxidation. *Phys Chem Chem Phys* **2012,** *14* (44), 15475-15481.
56. Wang, D. F.; Ye, J. H.; Kako, T.; Kimura, T., Photophysical and photocatalytic properties of SrTiO3 doped with Cr cations on different sites. *J Phys Chem B* **2006,** *110* (32), 15824-15830.
57. Konta, R.; Ishii, T.; Kato, H.; Kudo, A., Photocatalytic activities of noble metal ion doped SrTiO3 under visible light irradiation. *J Phys Chem B* **2004,** *108* (26), 8992-8995.
58. Hwang, D. W.; Kim, H. G.; Kim, J.; Cha, K. Y.; Kim, Y. G.; Lee, J. S., Photocatalytic water splitting over highly donor-doped (110) layered perovskites. *J Catal* **2000,** *193* (1), 40-48.
59. Kim, H. G.; Hwang, D. W.; Kim, J.; Kim, Y. G.; Lee, J. S., Highly donor-doped (110) layered perovskite materials as novel photocatalysts for overall water splitting. *Chem Commun* **1999,** (12), 1077-1078.
60. Wu, F.; Pavlovska, A.; Smith, D. J.; Culbertson, R. J.; Wilkens, B. J.; Bauer, E., Growth and structure of epitaxial CeO2 films on yttria-stabilized ZrO2. *Thin Solid Films* **2008,** *516* (15), 4908-4914.
61. Putna, E. S.; Bunluesin, T.; Fan, X. L.; Gorte, R. J.; Vohs, J. M.; Lakis, R. E.; Egami, T., Ceria films on zirconia substrates: models for understanding oxygen-storage properties. *Catal Today* **1999,** *50* (2), 343-352.
62. Costa-Nunes, O.; Gorte, R. J.; Vohs, J. M., High mobility of ceria films on zirconia at moderate temperatures. *J Mater Chem* **2005,** *15* (15), 1520-1522.
63. Kim, T. S.; Stiehl, J. D.; Reeves, C. T.; Meyer, R. J.; Mullins, C. B., Cryogenic CO oxidation on TiO2-supported gold nanoclusters precovered with atomic oxygen. *J Am Chem Soc* **2003,** *125* (8), 2018-2019.
64. Diebold, U.; Pan, J. M.; Madey, T. E., Ultrathin Metal-Films on Tio2(110) - Metal Overlayer Spreading and Surface Reactivity. *Surf Sci* **1993,** *287*, 896-900.
65. Woodruff, D. P.; Delchar, T. A., *Modern techniques of surface science*. Cambridge University Press: Cambridge Cambridgeshire ; New York, 1986; p x, 453 p.
66. Childs, K. D. C., B. A.; La Vanier, L. A.; Moulder, J. F.; Paul, D. F.; Stickle, W. F.; Watson, D. G., *Handbook of Auger Electron Spectroscopy*. Physical Electronic, Inc.: Eden Prairie, Minnesota., 1995.
67. Wagner, C. D. R., W.M.; Davis, L.E.; Moulder, J.F., *Handbook of X-ray Photoelectron Spectroscopy*. Perkin-Elmer Corporation: Eden Prairie, Minnesota, 1979.
68. Kim, K. S.; Barteau, M. A., Reactions of Aliphatic-Alcohols on the (011)-Faceted Tio2 (001) Surface. *J Mol Catal* **1990,** *63* (1), 103-117.
69. Wong, J. C. S.; Linsebigler, A.; Lu, G. Q.; Fan, J. F.; Yates, J. T., Photooxidation of Ch3cl on Tio2(110) Single-Crystal and Powdered Tio2 Surfaces. *J Phys Chem-Us* **1995,** *99* (1), 335-344.
70. Herman, G. S.; Dohnalek, Z.; Ruzycki, N.; Diebold, U., Experimental investigation of the interaction of water and methanol with anatase-TiO2(101). *J Phys Chem B* **2003,** *107* (12), 2788-2795.

71. Henderson, M. A., Structural sensitivity in the dissociation of water on TiO2 single-crystal surfaces. *Langmuir* **1996,** *12* (21), 5093-5098.
72. Hugenschmidt, M. B.; Gamble, L.; Campbell, C. T., The Interaction of H2o with a Tio2(110) Surface. *Surf Sci* **1994,** *302* (3), 329-340.
73. Lee, W.-H.; Liao, C.-H.; Tsai, M.-F.; Huang, C.-W.; Wu, J. C. S., A novel twin reactor for CO2 photoreduction to mimic artificial photosynthesis. *Applied Catalysis B: Environmental* **2013,** *132–133* (0), 445-451.
74. Williams, W. D.; Shekhar, M.; Lee, W. S.; Kispersky, V.; Delgass, W. N.; Ribeiro, F. H.; Kim, S. M.; Stach, E. A.; Miller, J. T.; Allard, L. F., Metallic Corner Atoms in Gold Clusters Supported on Rutile Are the Dominant Active Site during Water-Gas Shift Catalysis. *J Am Chem Soc* **2010,** *132* (40), 14018-14020.
75. Liu, P.; Rodriguez, J. A., Water-gas-shift reaction on metal nanoparticles and surfaces. *J Chem Phys* **2007,** *126* (16).
76. Diebold, U.; Lehman, J.; Mahmoud, T.; Kuhn, M.; Leonardelli, G.; Hebenstreit, W.; Schmid, M.; Varga, P., Intrinsic defects on a TiO2(110)(1x1) surface and their reaction with oxygen: a scanning tunneling microscopy study. *Surf Sci* **1998,** *411* (1-2), 137-153.
77. Bishop, H. E. R., J.C., Segregation of gold to teh cilicon (111) surface observed by Auger emission spectroscopy and by LEED. *Journal of Physics D: Applied Physics* **1969,** *2*, 1635-1643.
78. Mroczkowski, S.; Lichtman, D., Calculated Auger Yields and Sensitivity Factors for Kll-Noo Transitions with 1-10 Kv Primary Beams. *J Vac Sci Technol A* **1985,** *3* (4), 1860-1865.
79. Henderson, M. A., The interaction of water with solid surfaces: fundamental aspects revisited. *Surf Sci Rep* **2002,** *46* (1-8), 1-308.
80. Henderson, M. A., An HREELS and TPD study of water on TiO2(110): The extent of molecular versus dissociative adsorption. *Surf Sci* **1996,** *355* (1-3), 151-166.
81. Bange, K.; Grider, D. E.; Madey, T. E.; Sass, J. K., The Surface-Chemistry of H2o on Clean and Oxygen-Covered Cu(110). *Surf Sci* **1984,** *137* (1), 38-64.
82. Hinch, B. J.; Dubois, L. H., Stable and Metastable Phases of Water Adsorbed on Cu(111). *J Chem Phys* **1992,** *96* (4), 3262-3268.
83. Ojifinni, R. A.; Froemming, N. S.; Gong, J.; Pan, M.; Kim, T. S.; White, J. M.; Henkelman, G.; Mullins, C. B., Water-enhanced low-temperature CO oxidation and isotope effects on atomic oxygen-covered Au(111). *J Am Chem Soc* **2008,** *130* (21), 6801-6812.
84. Kolmakov, A.; Goodman, D. W., In situ scanning tunneling microscopy of oxide-supported metal clusters: Nucleation, growth, and thermal evolution of individual particles. *Chem Rec* **2002,** *2* (6), 446-457.
85. Zeng, Q. H.; Wong, K.; Jiang, X. C.; Yu, A. B., Molecular understanding of the deposition of gold nanoclusters on TiO(2)(110). *Appl Phys Lett* **2008,** *92* (10).
86. Wahlstrom, E.; Lopez, N.; Schaub, R.; Thostrup, P.; Ronnau, A.; Africh, C.; Laegsgaard, E.; Norskov, J. K.; Besenbacher, F., Bonding of gold nanoclusters to oxygen vacancies on rutile TiO2(110). *Phys Rev Lett* **2003,** *90* (2).
87. Zhou, J.; Chen, D. A., Controlling size distributions of copper islands grown on TiO2(110)-(1 x 2). *Surf Sci* **2003,** *527* (1-3), 183-197.
88. Artiglia, L.; Rizzi, G. A.; Sedona, F.; Agnoli, S.; Granozzi, G., Chemisorption of CO on Au/TiOx/Pt(111) Model Catalysts with Different Stoichiometry and Defectivity. *Journal of Nanoscience and Nanotechnology* **2008,** *8* (7), 3595-3602.

89. Ruggiero, C.; Hollins, P., Interaction of CO molecules with the Au(332) surface. *Surf Sci* **1997,** *377–379* (0), 583-586.
90. McElhiney, G.; Pritchard, J., The adsorption of Xe and CO on Au(100). *Surf Sci* **1976,** *60* (2), 397-410.
91. Mavrikakis, M.; Stoltze, P.; Nørskov, J. K., Making gold less noble. *Catal Lett* **2000,** *64* (2-4), 101-106.
92. Diemant, T.; Hartmann, H.; Bansmann, J.; Behm, R. J., CO adsorption energy on planar Au/TiO2 model catalysts under catalytically relevant conditions. *J Catal* **2007,** *252* (2), 171-177.
93. Stiehl, J. D.; Kim, T. S.; McClure, S. M.; Mullins, C. B., Reaction of CO with molecularly chemisorbed oxygen on TiO2-supported gold nanoclusters. *J Am Chem Soc* **2004,** *126* (42), 13574-13575.
94. Solsona, B. E.; Garcia, T.; Jones, C.; Taylor, S. H.; Carley, A. F.; Hutchings, G. J., Supported gold catalysts for the total oxidation of alkanes and carbon monoxide. *Appl Catal a-Gen* **2006,** *312*, 67-76.
95. Harendt, C.; Goschnick, J.; Hirschwald, W., The Interaction of Co with Copper (110) Studied by Tds and Leed. *Surf Sci* **1985,** *152* (Apr), 453-462.
96. Kirstein, W.; Kruger, B.; Thieme, F., Co Adsorption Studies on Pure and Ni-Covered Cu(111) Surfaces. *Surf Sci* **1986,** *176* (3), 505-529.
97. Parker, S. C.; Campbell, C. T., Reactivity and sintering kinetics of Au/TiO(2)(110) model catalysts: particle size effects. *Top Catal* **2007,** *44* (1-2), 3-13.
98. Yang, F.; Chen, M. S.; Goodman, D. W., Sintering of Au Particles Supported on TiO2(110) during CO Oxidation. *J Phys Chem C* **2009,** *113* (1), 254-260.
99. Lee, S.; Fan, C. Y.; Wu, T. P.; Anderson, S. L., Agglomeration, support effects, and CO adsorption on Au/TiO2(110) prepared by ion beam deposition. *Surf Sci* **2005,** *578* (1-3), 5-19.
100. Park, J. B.; Conner, S. F.; Chen, D. A., Bimetallic Pt-Au clusters on TiO2(110): Growth, surface composition, and metal-support interactions. *J Phys Chem C* **2008,** *112* (14), 5490-5500.
101. Kolmakov, A.; Goodman, D. W., In situ scanning tunneling microscopy of individual supported metal clusters at reactive gas pressures from 10(-8) to 10(4) Pa. *Rev Sci Instrum* **2003,** *74* (4), 2444-2450.
102. Zhou, J.; Kang, Y. C.; Chen, D. A., Oxygen-induced dissociation of Cu islands supported on TiO2(110). *J Phys Chem B* **2003,** *107* (28), 6664-6667.
103. Diebold, U.; Pan, J. M.; Madey, T. E., Growth Mode of Ultrathin Copper Overlayers on Tio2(110). *Phys Rev B* **1993,** *47* (7), 3868-3876.
104. Mullins, D. R.; Albrecht, P. M.; Chen, T. L.; Calaza, F. C.; Biegalski, M. D.; Christen, H. M.; Overbury, S. H., Water Dissociation on CeO2(100) and CeO2(111) Thin Films. *J Phys Chem C* **2012,** *116* (36), 19419-19428.
105. Yang, F.; Graciani, J.; Evans, J.; Liu, P.; Hrbek, J.; Sanz, J. F.; Rodriguez, J. A., CO Oxidation on Inverse CeOx/Cu(111) Catalysts: High Catalytic Activity and Ceria-Promoted Dissociation of O-2. *J Am Chem Soc* **2011,** *133* (10), 3444-3451.
106. Grabow, L. C.; Gokhale, A. A.; Evans, S. T.; Dumesic, J. A.; Mavrikakis, M., Mechanism of the water gas shift reaction on Pt: First principles, experiments, and microkinetic modeling. *J Phys Chem C* **2008,** *112* (12), 4608-4617.
107. Mullins, D. R.; Robbins, M. D.; Zhou, J., Adsorption and reaction of methanol on thin-film cerium oxide. *Surf Sci* **2006,** *600* (7), 1547-1558.
108. Mullins, D. R.; Senanayake, S. D.; Chen, T. L., Adsorption and Reaction of C-1-C-3 Alcohols over CeOx(111) Thin Films. *J Phys Chem C* **2010,** *114* (40), 17112-17119.

109. Chen, T. L.; Mullins, D. R., Ethylene Glycol Adsorption and Reaction over CeOx(111) Thin Films. *J Phys Chem C* **2011,** *115* (28), 13725-13733.
110. Senanayake, S. D.; Mullins, D. R., Redox pathways for HCOOH decomposition over CeO2 surfaces. *J Phys Chem C* **2008,** *112* (26), 9744-9752.
111. Chen, T. L.; Mullins, D. R., Adsorption and Reaction of Acetaldehyde over CeOX(111) Thin Films. *J Phys Chem C* **2011,** *115* (8), 3385-3392.
112. Ferrizz, R. M.; Egami, T.; Vohs, J. M., Temperature programmed desorption study of the reaction of C2H4 and CO on Rh supported on alpha-Al2O3(0001), YSZ(100) and CeO2 thin films. *Surf Sci* **2000,** *465* (1-2), 127-137.
113. Mullins, D. R.; Zhang, K. Z., Metal-support interactions between Pt and thin film cerium oxide. *Surf Sci* **2002,** *513* (1), 163-173.
114. Ferrizz, R. M.; Egami, T.; Wong, G. S.; Vohs, J. M., Reaction of NO on CeO2 and Rh/CeO2 thin films supported on alpha-Al2O3(0001) and YSZ(100). *Surf Sci* **2001,** *476* (1-2), 9-21.
115. Overbury, S. H.; Huntley, D. R.; Mullins, D. R.; Ailey, K. S.; Radulovic, P. V., Surface studies of model supported catalysts: NO adsorption on Rh/CeO2(001). *J Vac Sci Technol A* **1997,** *15* (3), 1647-1652.
116. Zafiris, G. S.; Gorte, R. J., A Study of Co, No, and H2 Adsorption on Model Pt/Ceo2 Catalysts. *Surf Sci* **1992,** *276* (1-3), 86-94.
117. Men, Y.; Gnaser, H.; Ziegler, C.; Zapf, R.; Hessel, V.; Kolb, G., Characterization of Cu/CeO2/gamma-Al2O3 thin film catalysts by thermal desorption spectroscopy. *Catal Lett* **2005,** *105* (1-2), 35-40.
118. Eklund, P.; Sridharan, M.; Singh, G.; Bottiger, J., Thermal Stability and Phase Transformations of gamma-/Amorphous-Al2O3 Thin Films. *Plasma Process Polym* **2009,** *6*, S907-S911.
119. Shyu, J. Z.; Otto, K.; Watkins, W. L. H.; Graham, G. W.; Belitz, R. K.; Gandhi, H. S., Characterization of Pd/Gamma-Alumina Catalysts Containing Ceria. *J Catal* **1988,** *114* (1), 23-33.
120. Herman, G. S.; Kim, Y. J.; Chambers, S. A.; Peden, C. H. F., Interaction of D2O with CeO2(001) investigated by temperature-programmed desorption and X-ray photoelectron spectroscopy. *Langmuir* **1999,** *15* (11), 3993-3997.
121. Molinari, M.; Parker, S. C.; Sayle, D. C.; Islam, M. S., Water Adsorption and Its Effect on the Stability of Low Index Stoichiometric and Reduced Surfaces of Ceria. *J Phys Chem C* **2012,** *116* (12), 7073-7082.
122. Henderson, M. A.; Perkins, C. L.; Engelhard, M. H.; Thevuthasan, S.; Peden, C. H. F., Redox properties of water on the oxidized and reduced surfaces of CeO2(111). *Surf Sci* **2003,** *526* (1-2), 1-18.
123. Kundakovic, L.; Mullins, D. R.; Overbury, S. H., Adsorption and reaction of H2O and CO on oxidized and reduced Rh/CeOx(111) surfaces. *Surf Sci* **2000,** *457* (1-2), 51-62.
124. Chen, B.; Ma, Y.; Ding, L.; Xu, L.; Wu, Z.; Yuan, Q.; Huang, W., Reactivity of Hydroxyls and Water on a CeO2(111) Thin Film Surface: The Role of Oxygen Vacancy. *The Journal of Physical Chemistry C* **2013,** *117* (11), 5800-5810.
125. Huang, M.; Fabris, S., CO adsorption and oxidation on ceria surfaces from DFT+U calculations. *J Phys Chem C* **2008,** *112* (23), 8643-8648.

126. Scanlon, D. O.; Galea, N. M.; Morgan, B. J.; Watson, G. W., Reactivity on the (110) Surface of Ceria: A GGA plus U Study of Surface Reduction and the Adsorption of CO and NO2. *J Phys Chem C* **2009,** *113* (25), 11095-11103.
127. Yang, Z. X.; He, B. L.; Lu, Z. S.; Hermansson, K., Physisorbed, Chemisorbed, and Oxidized CO on Highly Active Cu-CeO2(111). *J Phys Chem C* **2010,** *114* (10), 4486-4494.
128. Wilson, E. L.; Brown, W. A.; Thornton, G., RAIRS studies of CO adsorption on Pd/CeO(2-x)(111)/Pt(111). *Surf Sci* **2006,** *600* (12), 2555-2561.
129. Stubenrauch, J.; Vohs, J. M., Interaction of CO with Rh supported on stoichiometric and reduced CeO2(111) and CeO2(100) surfaces. *J Catal* **1996,** *159* (1), 50-57.
130. Xu, J.; Mullins, D. R.; Overbury, S. H., CO desorption and oxidation on CeO2-supported Rh: Evidence for two types of Rh sites. *J Catal* **2006,** *243* (1), 158-164.
131. Reddic, J. E.; Zhou, J.; Chen, D. A., Scanning tunneling microscopy studies of the growth of Cu clusters on a reconstructed TiO2(110)-(1 x 2) surface. *Surf Sci* **2001,** *494* (1), L767-L772.
132. Zhou, J.; Kang, Y. C.; Ma, S.; Chen, D. A., Adsorbate-induced dissociation of metal clusters: TiO2 (110)-supported Cu and Ni clusters exposed to oxygen gas. *Surf Sci* **2004,** *562* (1-3), 113-127.
133. Majimel, J.; Lamirand-Majimel, M.; Moog, I.; Feral-Martin, C.; Treguer-Delapierre, M., Size-Dependent Stability of Supported Gold Nanostructures onto Ceria: an HRTEM Study. *J Phys Chem C* **2009,** *113* (21), 9275-9283.
134. Sun, H. P.; Pan, X. P.; Graham, G. W.; Jen, H. W.; McCabe, R. W.; Thevuthasan, S.; Peden, C. H. F., Partial encapsulation of Pd particles by reduced ceria-zirconia. *Appl Phys Lett* **2005,** *87* (20).
135. Zhou, Y. H.; Zhou, J., Growth and Sintering of Au-Pt Nanoparticles on Oxidized and Reduced CeOx(111) Thin Films by Scanning Tunneling Microscopy. *J Phys Chem Lett* **2010,** *1* (3), 609-615.
136. Graham, G. W.; Jen, H. W.; Chun, W.; McCabe, R. W., High-temperature-aging-induced encapsulation of metal particles by support materials: Comparative results for Pt, Pd, and Rh on cerium-zirconium mixed oxides. *J Catal* **1999,** *182* (1), 228-233.
137. Caballero, A.; Holgado, J. P.; Gonzalez-delaCruz, V. M.; Habas, S. E.; Herranz, T.; Salmeron, M., In situ spectroscopic detection of SMSI effect in a Ni/CeO2 system: hydrogen-induced burial and dig out of metallic nickel. *Chem Commun* **2010,** *46* (7), 1097-1099.
138. Akita, T.; Tanaka, K.; Kohyama, M.; Haruta, M., Analytical TEM study on structural changes of Au particles on cerium oxide using a heating holder. *Catal Today* **2007,** *122* (3-4), 233-238.
139. Akita, T.; Okumura, M.; Tanaka, K.; Kohyama, M.; Haruta, M., TEM observation of gold nanoparticles deposited on cerium oxide. *J Mater Sci* **2005,** *40* (12), 3101-3106.
140. Bernal, S.; Botana, F. J.; Calvino, J. J.; Cifredo, G. A.; Perezomil, J. A., Hrem Study of the Behavior of a Rh/Ceo2 Catalyst under High-Temperature Reducing and Oxidizing Conditions. *Catal Today* **1995,** *23* (3), 219-250.
141. Pfau, A.; Schierbaum, K. D., The Electronic-Structure of Stoichiometric and Reduced Ceo2 Surfaces - an Xps, Ups and Hreels Study. *Surf Sci* **1994,** *321* (1-2), 71-80.
142. Fox, E. B.; Velu, S.; Engelhard, M. H.; Chin, Y. H.; Miller, J. T.; Kropf, J.; Song, C. S., Characterization of CeO2-supported Cu-Pd bimetallic catalyst for the oxygen-assisted water-gas shift reaction. *J Catal* **2008,** *260* (2), 358-370.

143. Zou, Z. G.; Ye, J. H.; Sayama, K.; Arakawa, H., Direct splitting of water under visible light irradiation with an oxide semiconductor photocatalyst. *Nature* **2001,** *414* (6864), 625-627.
144. Kuo, Y. T.; Klabunde, K. J., Hydrogen generation from water/methanol under visible light using aerogel prepared strontium titanate (SrTiO3) nanomaterials doped with ruthenium and rhodium metals. *Nanotechnology* **2012,** *23* (29).
145. Chen, H. C.; Huang, C. W.; Wu, J. C. S.; Lin, S. T., Theoretical Investigation of the Metal-Doped SrTiO3 Photocatalysts for Water Splitting. *J Phys Chem C* **2012,** *116* (14), 7897-7903.
146. Sasaki, Y.; Nemoto, H.; Saito, K.; Kudo, A., Solar Water Splitting Using Powdered Photocatalysts Driven by Z-Schematic Interparticle Electron Transfer without an Electron Mediator. *J Phys Chem C* **2009,** *113* (40), 17536-17542.
147. Bae, S. W.; Borse, P. H.; Lee, J. S., Dopant dependent band gap tailoring of hydrothermally prepared cubic SrTi(x)M(1-x)O(3) (M=Ru,Rh,Ir,Pt,Pd) nanoparticles as visible light photocatalysts. *Appl Phys Lett* **2008,** *92* (10).
148. Shen, P.; Lofaro Jr, J. C.; Woerner, W. R.; White, M. G.; Su, D.; Orlov, A., Photocatalytic activity of hydrogen evolution over Rh doped SrTiO3 prepared by polymerizable complex method. *Chem Eng J* **2013,** *223* (0), 200-208.
149. Kosola, A.; Putkonen, M.; Johansson, L. S.; Niinisto, L., Effect of annealing in processing of strontium titanate thin films by ALD. *Appl Surf Sci* **2003,** *211* (1-4), 102-112.
150. Wang, T. X.; Chen, W. W., Solid phase preparation of submicron-sized SrTiO3 crystallites from SrO2 nanoparticles and TiO2 powders. *Mater Lett* **2008,** *62* (17-18), 2865-2867.
151. WengSieh, Z.; Gronsky, R.; Bell, A. T., Microstructural evolution of gamma-alumina-supported Rh upon aging in air. *J Catal* **1997,** *170* (1), 62-74.
152. Bonnell, D. A.; Garra, J., Scanning probe microscopy of oxide surfaces: atomic structure and properties. *Rep Prog Phys* **2008,** *71* (4).
153. Masuda, Y.; Mashima, R.; Yamada, M.; Ikeuchi, K.; Murai, K.; Waterhouse, G. I. N.; Metson, J. B.; Moriga, T., Relationship between anion and cation nonstoichiometries and valence state of titanium in perovskite-type oxynitrides LaTiO2N. *J Ceram Soc Jpn* **2009,** *117* (1361), 76-81.
154. Nishimura, N.; Raphael, B.; Maeda, K.; Le Gendre, L.; Abe, R.; Kubota, J.; Domen, K., Effect of TiCl(4) treatment on the photoelectrochemical properties of LaTiO(2)N electrodes for water splitting under visible light. *Thin Solid Films* **2010,** *518* (20), 5855-5859.
155. Ebbinghaus, S. G.; Aguiar, R.; Weidenkaff, A.; Gsell, S.; Reller, A., Topotactical growth of thick perovskite oxynitride layers by nitridation of single crystalline oxides. *Solid State Sci* **2008,** *10* (6), 709-716.
156. Domen, K.; Kudo, A.; Shinozaki, A.; Tanaka, A.; Maruya, K.; Onishi, T., Photodecomposition of Water and Hydrogen Evolution from Aqueous Methanol Solution over Novel Niobate Photocatalysts. *J Chem Soc Chem Comm* **1986,** (4), 356-357.
157. Sayama, K.; Arakawa, H.; Domen, K., Photocatalytic water splitting on nickel intercalated A(4)Ta(x)Nb(6-x)O(17) (A=K, Rb). *Catal Today* **1996,** *28* (1-2), 175-182.
158. Sayama, K.; Tanaka, A.; Domen, K.; Maruya, K.; Onishi, T., Photocatalytic Decomposition of Water over a Ni-Loaded Rb4nb6o17 Catalyst. *J Catal* **1990,** *124* (2), 541-547.
159. Williams, T.; Schmalle, H.; Reller, A.; Lichtenberg, F.; Widmer, D.; Bednorz, G., On the Crystal-Structures of La2ti2o7 and La5ti5o17 - High-Resolution Electron-Microscopy. *J Solid State Chem* **1991,** *93* (2), 534-548.

160. Zhang, F. X.; Lian, J.; Becker, U.; Ewing, R. C.; Wang, L. M.; Hu, J. Z.; Saxena, S. K., Structural change of layered perovskite La2Ti2O7 at high pressures. *J Solid State Chem* **2007,** *180* (2), 571-576.
161. Sakatani, Y.; Nunoshige, J.; Ando, H.; Okusako, K.; Koike, H.; Takata, T.; Kondo, J. N.; Hara, M.; Domen, K., Photocatalytic decomposition of acetaldehyde under visible light irradiation over La3+ and N co-doped TiO2. *Chem Lett* **2003,** *32* (12), 1156-1157.
162. Ando, T.; Wakamatsu, T.; Masuda, K.; Yoshida, N.; Suzuki, K.; Masutani, S.; Katayama, I.; Uchida, H.; Hirose, H.; Kamimoto, A., Photocatalytic behavior of heavy La-doped TiO2 films deposited by pulsed laser deposition using non-sintered target. *Appl Surf Sci* **2009,** *255* (24), 9688-9690.
163. Onozuka, K.; Kawakami, Y.; Imai, H.; Yokoi, T.; Tatsumi, T.; Kondo, J. N., Perovskite-type La2Ti2O7 nriesoporous photocatalyst. *J Solid State Chem* **2012,** *192*, 87-92.
164. Hwang, D. W.; Lee, J. S.; Li, W.; Oh, S. H., Electronic band structure and photocatalytic activity of Ln(2)Ti(2)O(7) (Ln = La, Pr, Nd). *J Phys Chem B* **2003,** *107* (21), 4963-4970.
165. Kasahara, A.; Nukumizu, K.; Takata, T.; Kondo, J. N.; Hara, M.; Kobayashi, H.; Domen, K., LaTiO2N as a visible-light (<= 600 nm)-driven photocatalyst (2). *J Phys Chem B* **2003,** *107* (3), 791-797.
166. NIST Standard Reference Database 82: NIST Electron Effective-Attenuation-Length Database. 1.1 ed.; Commerce, U. S. S. o., Ed. 2003.
167. Suzuki, S.; Ishii, T.; Sagawa, T., X-Ray Photoemission Spectra of 4d and 3d Electrons in Lanthanum-Halides and Cerium-Halides. *J Phys Soc Jpn* **1974,** *37* (5), 1334-1340.
168. Sunding, M. F.; Hadidi, K.; Diplas, S.; Lovvik, O. M.; Norby, T. E.; Gunnaes, A. E., XPS characterisation of in situ treated lanthanum oxide and hydroxide using tailored charge referencing and peak fitting procedures. *J Electron Spectrosc* **2011,** *184* (7), 399-409.
169. Diebold, U., The surface science of titanium dioxide. *Surf Sci Rep* **2003,** *48* (5-8), 53-229.
170. Lu, F.-H.; Chen, H.-Y., XPS analyses of TiN films on Cu substrates after annealing in the controlled atmosphere. *Thin Solid Films* **1999,** *355–356* (0), 374-379.
171. Wang, L. Q.; Ferris, K. F.; Herman, G. S., Interactions of H2O with SrTiO3(100) surfaces. *J Vac Sci Technol A* **2002,** *20* (1), 239-244.
172. Henderson, M. A., Ethyl radical ejection during photodecomposition of butanone on TiO2(1 1 0). *Surf Sci* **2008,** *602* (20), 3188-3193.